# Spin Qubit Studies Using A 2x2 Quantum Dot Array In Si/SiGe

Unseld, F.K.

**DOI**
10.4233/uuid:ef54221a-ff19-485e-9e16-14af85de035e

**Publication date**
2025

**Document Version**
Final published version

**Citation (APA)**
Unseld, F. K. (2025). *Spin Qubit Studies Using A 2x2 Quantum Dot Array In Si/SiGe*. [Dissertation (TU Delft), Delft University of Technology]. https://doi.org/10.4233/uuid:ef54221a-ff19-485e-9e16-14af85de035e

# Spin Qubit Studies Using A 2x2 Quantum Dot Array In Si/SiGe

Florian Karl Unseld

# Spin Qubit Studies Using A 2x2 Quantum Dot Array In Si/SiGe

## Dissertation

for the purpose of obtaining the degree of doctor
at Delft University of Technology
by the authority of the Rector Magnificus,
prof. dr. ir. T.H.J.J. van der Hagen,
chair of the Board for Doctorates
to be defended publicly on
Wednesday 01 October 2025 at 17:30

by


**Florian Karl UNSELD**

Master of Science in Electrical Engineering and Information Technology,
Technische Universität München, Germany
born in Ulm, Germany

This dissertation has been approved by the promotors.

Composition of the doctoral committee:

| | |
|---|---|
| Rector Magnificus, | chairperson |
| **Promotors:** | |
| Prof. dr. ir. L.M.K.Vandersypen | Delft University of Technology |
| Dr.ir. M. Veldhorst, | Delft University of Technology |
| **Independent members:** | |
| Prof. dr. K. De Greve | Katholieke Universiteit Leuven, Belgium |
| Dr. A. Laucht | The University of New South Wales, Australia |
| Prof. dr. L. DiCarlo | Delft University of Technology |
| Dr. G. Scappucci | Delft University of Technology |
| **Reserve member:** | |
| Prof. dr. B. M. Terhal | Delft University of Technology |

QuTech


intel


*Keywords:* Quantum Computing, Quantum Dots, Spin Qubits, 2D-Array, Baseband Control

*Printed by:* Gildeprint

*Cover:* Simulated hopping gate (front) overlaid with measured data (back).



ISBN 978-94-6518-117-2

An electronic copy of this dissertation is available at
https://repository.tudelft.nl/.

*One day there will be no borders, no boundaries, no flags and no countries and the only passport will be the heart.*

Carlos Santana

# CONTENTS

# SUMMARY

Classical computers have long been the cornerstone of information processing, yet their capabilities are constrained by the limits of the classical laws of physics. Quantum mechanics offers a new spin on information processing, potentially providing immense speed-ups for some specialized problems. There are many approaches to building such a quantum computer, that leverages quantum mechanical principles. The most popular approach uses superconducting circuits to implement a qubit. This thesis, however, builds on the advances of the semiconductor industry. The miniaturisation of electronic devices in the last decades has enabled the fabrication of gate defined quantum dots. Such a quantum dot allows the isolation of a single charged particle that can be used to implement a qubit. More specifically this thesis employs electrons in Si/SiGe heterostructures. While most implementations so far rely on linear chains of quantum dots, scaling in a second dimension is crucial for building larger systems.

This thesis explores a 2x2 array as a proof of concept for a 2D array. This small-scale device demonstrates that charge-related properties, such as gate pitches and tunnel coupling control, remain similar when transitioning from one to two dimensions. We show that existing qubit control strategies using electric-dipole spin resonance (EDSR) and micromagnets can also be adopted for 2D arrays as long as the second dimension remains small. In larger 2D arrays, the magnetic field gradients achievable by micromagnets no longer meet the requirements for EDSR control. Additionally, the application of microwave bursts causes an unintended spin resonance shift that complicates qubit manipulation.

To address these challenges, this thesis also explores baseband control of single-spin qubits. In this scheme, single-qubit rotations are implemented using hopping gates, which use tilted quantisation axes in neighbouring quantum dots. In Si/SiGe this tilt is achieved using the strong spatial variation of the stray field of a nearly demagnetized micromagnet. Building on this, a nanomagnet-based architecture is proposed, integrating localized nanomagnets to provide magnetic field gradients for spin manipulation. This approach circumvents EDSR limitations, offering a more scalable pathway for 2D quantum dot arrays and advancing spin qubit technologies toward large-scale quantum computing.

# SAMENVATTING

Klassieke computers zijn al lang de hoeksteen van informatieverwerking, maar hun mogelijkheden worden beperkt door de grenzen van de klassieke natuurwetten. De kwantummechanica biedt een nieuwe kijk op informatieverwerking en kan mogelijk enorme snelheidswinsten opleveren voor bepaalde gespecialiseerde problemen. Er zijn veel benaderingen om een kwantumcomputer te bouwen die gebruikmaakt van kwantummechanische principes. De meest populaire aanpak gebruikt supergeleidende circuits om een qubit te implementeren. Deze thesis bouwt echter voort op de vooruitgang van de halfgeleiderindustrie. De miniaturisatie van elektronische apparaten in de afgelopen decennia heeft de fabricage van gate-gedefinieerde kwantumdots mogelijk gemaakt. Zo'n kwantumdot maakt het mogelijk om een enkel geladen deeltje te isoleren dat als qubit kan fungeren. Meer specifiek maakt deze thesis gebruik van elektronen in Si/SiGe-heterostructuren. Hoewel de meeste implementaties tot nu toe lineaire ketens van kwantumdots aanwenden, is schaalvergroting in een tweede dimensie cruciaal voor het bouwen van grotere systemen.

Deze thesis onderzoekt een 2x2-array als proof of concept voor een 2D-array. Dit kleinschalige apparaat laat zien dat eigenschappen gerelateerd aan lading, zoals gate-afstanden en tunnelkoppeling, vergelijkbaar blijven bij de overgang van één naar twee dimensies. We tonen aan dat bestaande qubit-controlestrategieën met behulp van elektrische dipool-spinresonantie (EDSR) en micromagneten ook kunnen worden toegepast op 2D-arrays, zolang de tweede dimensie klein blijft. In grotere 2D-arrays zullen micromagneten niet in staat zijn om de magnetische veldgradiënten te genereren die nodig zijn voor EDSR controle. Bovendien veroorzaakt het aanleggen van microgolfpulsen een onbedoelde spinresonantieverschuiving, wat de manipulatie van qubits compliceert.

Om deze uitdagingen aan te pakken, onderzoekt deze thesis ook baseband-controle van enkele spin qubits. In dit schema worden enkele-qubit-rotaties geïmplementeerd met behulp van hopping gates, die gebruikmaken van gekantelde kwantisatie-assen in naburige kwantumdots. In Si/SiGe wordt deze kanteling bereikt door de sterke ruimtelijke variatie van het strooiveld van een bijna gedemagnetiseerde micromagneet. Hierop voortbordurend wordt een nanomagneet-gebaseerde architectuur voorgesteld, waarbij gelokaliseerde nanomagneten worden geïntegreerd om magnetische veldgradiënten te leveren voor spinmanipulatie. Deze aanpak omzeilt de beperkingen van EDSR en biedt een

meer schaalbare weg voor 2D-kwantumdot-arrays, waardoor spinqubit-technologieën een stap dichter komen bij grootschalige kwantumcomputing.

# ZUSAMMENFASSUNG

Klassische Computer sind seit langem das Fundament der Informationsverarbeitung, doch ihre Fähigkeiten sind durch die Grenzen der klassischen Physik beschränkt. Die Quantenmechanik bietet eine neue Perspektive auf die Informationsverarbeitung und könnte für einige spezialisierte Probleme enorme Geschwindigkeitsvorteile ermöglichen. Es gibt viele Ansätze, um einen solchen Quantencomputer zu bauen, der quantenmechanische Prinzipien nutzt. Der populärste Ansatz verwendet supraleitende Schaltkreise zur Implementierung eines Qubits. Diese Dissertation hingegen baut auf die Fortschritte der klassischen Halbleiterindustrie. Die Miniaturisierung in den letzten Jahrzehnten hat die Herstellung von gate-definierten Quantenpunkten ermöglicht. Ein solcher Quantenpunkt erlaubt die Isolation eines einzelnen geladenen Teilchens, das zur Implementierung eines Qubits verwendet werden kann. Konkret nutzt diese Arbeit Elektronen, die in Si/SiGe-Heterostrukturen. Während die meisten bisherigen Implementierungen auf linearen Ketten von Quantenpunkten basieren, ist die Skalierung in eine zweite Dimension entscheidend für den Aufbau größerer Systeme.

Diese Arbeit untersucht ein 2x2-Array als Proof of Concept für ein zweidimensionales Array. Dieses Miniatur-System zeigt, dass ladungsbezogene Eigenschaften wie Gate-Abstände und die Kontrolle der Tunnelkopplung beim Übergang von einer zu zwei Dimensionen ähnlich bleiben.Wir demonstrieren, dass bestehende Qubit-Steuerungsmethoden – etwa elektrische Dipolspinresonanz (EDSR) mit Mikromagneten – auch auf 2D-Arrays anwendbar sind, solange die zweite Dimension klein bleibt. In größeren 2D-Arrays erfüllen die mit Mikromagneten erreichbaren Magnetfeldgradienten nicht mehr die Anforderungen für die EDSR-Kontrolle. Zudem führen Mikrowellenpulse zu unbeabsichtigten Resonanzverschiebungen, welche die Manipulation von Qubiten erschweren.

Um diese Herausforderungen zu adressieren, untersucht diese Arbeit auch die Basisband-Steuerung von Einzelspin-Qubits. In diesem Schema werden Einzelqubit-Rotationen durch sogenannte Hopping-Gates implementiert, die geneigte Quantisierungsachsen in benachbarten Quantenpunkten nutzen. In Si/SiGe wird diese Neigung durch die starke räumliche Variation des Streufelds eines nahezu entmagnetisierten Mikromagneten erreicht. Darauf aufbauend wird eine nanomagnetische Architektur vorgeschlagen, die lokalisierte Nanomagnete integriert, um Magnetfeldgradienten für die Spin-Manipulation bereitzustellen. Dieser Ansatz umgeht die Einschränkungen von EDSR und bietet einen skalierbareren Weg für

2D-Quantenpunkt-Arrays, wodurch die Spin-Qubit-Technologien in Richtung großskaliger Quantencomputer vorangetrieben werden.

# 1

# INTRODUCTION

*Some books are to be tasted,*
*others to be swallowed,*
*and some few to be chewed and digested...*

Francis Bacon

# 1

Quantum computing builds on two major strands of development in the 20$^{th}$ century: the development of quantum mechanics and the invention of classical computers. The first, quantum mechanics, has revolutionized our understanding of the microscopic world, with “spooky” phenomena, such as superposition and entanglement. Quantum computers aim to exploit these properties to process information in fundamentally new ways, which enable exponentially faster computations for highly specific problems. The promise of quantum advantage, particularly in fields such as cryptography, optimization, and drug discovery, has driven substantial research and technological development in the pursuit of a large-scale quantum computer [1–3].

The second major foundation of quantum computing lies in classical computers and advancements in information processing. Particularly for solid-state-based quantum computers the progress in semiconductor materials and later nano fabrication plays a pivotal role. Both are part of a development process spanning multiple decades. The shrinkage of components and improvements to the materials established the integrated circuit (IC) as the backbone of the classical information age. However, the miniaturisation of the last decade then uncovered quantum mechanical effects in conventional electronic devices, enabling quantum computer architectures based on structures analogous to classical transistors. These structures are known as gate based quantum dots.

## 1.1. HISTORY OF QUANTUM MECHANICS

Many people mark the birth of quantum mechanics with Planck’s theory on black body radiation from 1900/1901. He hypothesized that electromagnetic radiation is emitted in discrete "quanta" rather than a continuous spectrum [4]. His publication also introduced a constant $h$, with a value of $6.55 \times 10^{-27}\,\mathrm{erg} \times \mathrm{second}$, to describe the quantization of energy $E$ in relation to the frequency $f$ of electromagnetic radiation. Today, this constant is known as the Planck constant, with the exact value of $6.626\,070\,15 \times 10^{-34}\,\mathrm{J\,Hz^{-1}}$.

The significance of this discovery became clearer when Albert Einstein used this constant to explain the photoelectric effect in 1905 [5]. This experimental effect demonstrated that all light consists of discrete packets of energy, or photons, whose energy is proportional to their frequency, following the now well-known relation $E = hf$. The groundbreaking nature of this discovery earned Einstein the Nobel Prize. Planck’s theoretical concept of blackbody radiation, once abstract, became much more tangible through its application to the photoelectric effect.

Also Niels Bohr used the idea of discretized energies. He proposed that electrons orbit the nucleus of an atom only at specific, discrete

energy levels. According to this model, electrons can only absorb or emit photons whose energy corresponds to the difference between these discrete orbital levels [6]. At the time, Bohr's model was the most complete and comprehensive theory explaining the puzzling emission spectrum of the hydrogen atom.

By the mid-1920s, Werner Heisenberg and Erwin Schrödinger independently developed mathematical frameworks to describe quantum theory [8, 9]. Heisenberg introduced matrix mechanics, focusing on observable quantities like energy, and formulated the uncertainty principle [10]. He stated that certain properties, such as position and momentum, cannot be measured with arbitrary precision at the same time. This introduced the concept that quantum systems have an inherent uncertainty.

**Figure 1.1: Conference image of the fifth Solvay conference** [7]**.**

Meanwhile, Schrödinger developed the wave mechanics and the Schrödinger equation, which describes how quantum systems evolve over time. His interpretation of the wave function provides the probability distribution of different measurement outcomes, further reinforcing the probabilistic nature of quantum theory.

While these theories became more refined and increasingly capable of describing strange phenomena, they were not widely accepted. Einstein himself rejected them and wrote to fellow physicist Max Born, "*I, at any rate, am convinced that He does not throw dice*" [11], referring to the probabilistic nature of quantum mechanics.

The fifth instalment of the Solvay Conference in 1927 marks a historic event in the development of quantum mechanics. Many of the most prolific physicists of the era attended the conference and gathered for the famous photograph in Fig. 1.1. Concepts such as particle-wave duality and the role of measurements in determining the state of a quantum system were debated. Famously, Einstein and Bohr had heated arguments about the validity of the Copenhagen interpretation. The discoveries and advancements made during this time are often collectively referred to as the first quantum revolution, as it fundamentally transformed our understanding of physics.

The start of the second quantum revolution is marked by the ideas of Richard Feynman. In a lecture series in 1982 (see Fig. 1.2), he stated, "*Nature isn't classical, dammit, and if you want to make a simulation of*

1

*nature, you'd better make it quantum mechanical, and by golly it's a wonderful problem, because it doesn't look so easy.*" [12]. Effectively, he proposed to actively make use of effects that had so far only been observed and acknowledged. Paul Benioff and David Deutsch picked up this idea and developed the notion of a quantum computer by adopting and extending the Turing machine to the quantum realm [13, 14]. Although any technical realisations of a quantum computer were still years away, powerful use cases were designed.

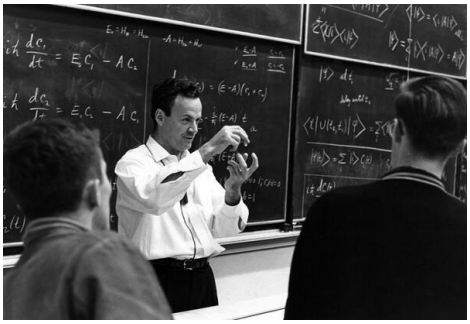

**Figure 1.2: R. P. Feynman giving a lecture on quantum mechanics** [15]**.**

The most notorious algorithm was developed by Peter Shor in 1993/1994 [2]. This algorithm demonstrates how a quantum computer can efficiently factorise numbers into their prime factors — a task that takes exponential effort using the best known classical algorithms, making it in practice infeasible to solve for large instances. This infeasibility is so widely accepted that most digital security systems were, and still are, based around this problem. It is easy to understand why this algorithm, and with it quantum computers, gained massive interest, as it could potentially allow access to most encrypted information on the internet. It should, however, be noted that almost a decade earlier, Charles Bennett and Gilles Brassard developed a secure quantum communication protocol, which cannot be broken even using quantum computer [16].

Sixteen years after Feynman proposed the idea of using quantum mechanics, Isaac Chuang, Neil Gershenfeld, and Mark Kubinec built the first quantum computer. It was made from chloroform and contained two quantum bits (qubits) that could store information for a few ns [17]. By 2000, Shor's algorithm saw its first experimental realisation factoring 15 into 5 and 3[18]. While these quantum computers were hardly useful, they provided significant proof of concept.

Since then, new and better ways to encode, manipulate, store, and transmit quantum information have been developed. Only 19 years later a quantum computer outperformed the best available classical computer [19]. The outcome, however, was highly disputed, particularly due to its limited usefulness and the argument that improvements in classical computing could challenge the performance advantage [20].

Today, multiple different ways to build a quantum computer still compete with each other, with no clear winner in sight. The fragility

of information encoded in a quantum mechanical object remains a significant obstacle. Error correction provides a mitigation of this problem; however, until recently, the added overhead only reduced the overall performance. Using superconducting qubits, Google's quantum team managed to demonstrate that quantum error correction is capable of improving the lifetime of qubits [21].

## 1.2. HISTORY OF COMPUTERS

The origins of modern computing can be traced back to 1830, when Charles Babbage designed the Difference Engine and later the Analytical Engine, the latter widely regarded as the first general-purpose computer [22].

Babbage envisioned a machine capable of solving any arithmetic problem using three key components. First, the Mill, which served as the calculating unit, was analogous to today's central processing unit (CPU). Second, its "hard drive" could store a thousand 50-digit numbers—equivalent to around 170 kbit. Third, input/output were managed via punch cards, which could encode both numbers and instructions, introducing concepts like looping and conditional branching that remain fundamental to modern programming.

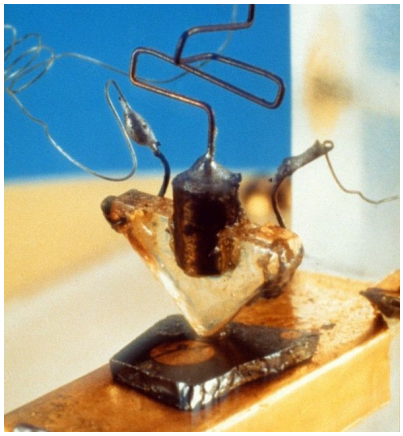

**Figure 1.3: First transistor from Bell Labs.** The spring in the centre presses a plastic wedge onto a Ge crystal. The wires going left and right are the collector and emitter of the transistor. They connect to the Ge crystal via thin gold foil on the sides of the plastic wedge. Below the Germanium crystal is the golden base contact of the transistor. Image courtesy of AT&T Archives and History Center.

Collaborating with Babbage, Ada Lovelace wrote in 1843 the first-ever computer program which could calculate Bernoulli numbers. However, her vision extended beyond numerical computation; she foresaw that such machines could generate art and compose music [23].

For decades after Babbage and Lovelace's work, progress stagnated. Only in the 1930s Alan Turing revolutionised theoretical computer science with his conception of the Turing Machine [24]. This abstract model established a framework for understanding the limits of

computation and remains a cornerstone of the discipline. Around the same time, Konrad Zuse, focused on practical implementations. He built a series of electromechanical computers called Z-machines. The Z3, completed in 1941, became the world's first programmable digital computer. Zuse's use of binary logic allowed him to shrink components and increase complexity [25].

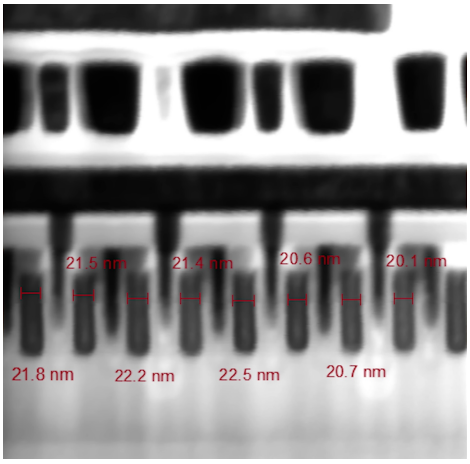


**Figure 1.4: Transmission electron microscopy of transistors of a commercial CPU.** The CPU was made in 2019 using the TSMC 7 nm process. Highlighted in red are gate lengths. Image courtesy of R. "Der 8auer" Hartung [26].

Building on these theoretical and practical advancements, Claude Shannon fundamentally transformed how information is understood and processed. He introduced the concept of entropy as a measure of uncertainty in information systems [27]. His work also demonstrated that any data could be represented and transmitted efficiently using binary encoding. These ideas not only established the bit as the fundamental unit of information but also created a theoretical foundation for error correction, data compression, and telecommunications, shaping the design of modern digital systems.

While these early innovations laid the groundwork for computational theory and basic programmable machines, the invention of transistors in 1947 by Bardeen, Shockley, and Brattain marked a turning point in hardware development. Using a pure germanium crystal designed for diodes and applying a voltage to it, the trio successfully modulated the current between two gold contacts. The prototype is depicted in Fig. 1.3. Building on the transistor's success, the 1950s saw Jack Kilby, Robert Noyce, and Geoffrey Dummer propose and demonstrate the integration of multiple transistors into a single semiconductor chip [28–30]. This innovation not only reduced size and cost but also significantly enhanced performance, paving the way for the rapid miniaturisation and increased computational power of modern computing devices.

Gordon Moore observed these trends of miniaturisation and increasing performance and complexity and famously predicted in 1965 that the number of transistors on a microchip would double approximately every year [31]. He later revised this prediction to a doubling every two

years. This observation, known as Moore's Law, became a self-fulfilling prophecy, as it set the goals for the semiconductor industry for decades. Although Moore's Law has slowed in recent years, the miniaturisation of components continues, with modern semiconductor fabrication lines now producing chips containing trillions of identical transistors. Fig. 1.4 shows several transistors side by side in a modern CPU. However, as transistor gates shrink below a certain size, quantum mechanical effects are beginning to impact their performance. These effects, which present challenges for classical computing, also present new opportunities for quantum computing.

## 1.3. CHAPTER OVERVIEW

With these brief historical overviews as a foundation, Chapter 2 aims to marry the fields of quantum mechanics and computers. It provides the necessary background information on quantum information, semiconductor quantum dots, and spin qubits. More practical information on how to build a suitable set-up to run spin qubit experiments is provided in Chapter 3. The two subsequent Chapters, Chapter 4 and Chapter 5, will make use of this information and describe my experiments on scaling silicon (Si)/silicon-germanium (Ge) quantum dots in two dimensions.

While impressive advancements have pushed quantum computers based on Si/SiGe quantum dots with partial control up to twelve qubits [32] including high-fidelity universal gate sets [33–35], high-fidelity initialization and readout of multiple qubits [36, 37], and coherent spin shuttling [34, 38], in one dimension. The limited connectivity and stringent fault tolerance thresholds of linear arrays imply that entering the second dimension is all but essential [39].

My experiments provide insight on different aspects of scaling in a second dimension. Chapter 4 will focus on the charge state and the control of the tunnel couplings. It shows that existing control strategies are adoptable with minor accommodations in two dimensions. On the other hand, Chapter 5 concerns itself with spin qubits, their performance, and control strategies. We show that existing control strategies can be adopted but issues such as heating as discovered in linear devices [40] will remain a notable issue. The Chapter also shows a new way to control spin qubits in Si/SiGe and how this new approach might be scaled up to larger devices. Lastly, Chapter 6 will provide an overview and outlook.

# REFERENCES


[1] S. Pirandola, U. L. Andersen, L. Banchi, M. Berta, D. Bunandar, R. Colbeck, D. Englund, T. Gehring, C. Lupo, C. Ottaviani, J. L. Pereira, M. Razavi, J. Shamsul Shaari, M. Tomamichel, V. C. Usenko, G. Vallone, P. Villoresi, and P. Wallden. "Advances in quantum cryptography". In: *Advances in Optics and Photonics* 12.4 (Dec. 2020), p. 1012. doi: 10.1364/aop.361502.

[2] P. W. Shor. "Algorithms for quantum computation: discrete logarithms and factoring". In: *Proceedings 35th Annual Symposium on Foundations of Computer Science*. SFCS-94. IEEE Comput. Soc. Press, 1994, pp. 124–134. doi: 10.1109/sfcs.1994.365700.

[3] N. S. Blunt, J. Camps, O. Crawford, R. Izsák, S. Leontica, A. Mirani, A. E. Moylett, S. A. Scivier, C. Sünderhauf, P. Schopf, J. M. Taylor, and N. Holzmann. "Perspective on the Current State-of-the-Art of Quantum Computing for Drug Discovery Applications". In: *Journal of Chemical Theory and Computation* 18.12 (Nov. 2022), pp. 7001–7023. doi: 10.1021/acs.jctc.2c00574.

[4] M. Planck. "Über das Gesetz der Energieverteilung im Normalspectrum". In: *Annalen der Physik* 309.3 (Jan. 1901), pp. 553–563. doi: 10.1002/andp.19013090310.

[5] A. Einstein. "Über einen die Erzeugung und Verwandlung des Lichtes betreffenden heuristischen Gesichtspunkt". In: *Annalen der Physik* 322.6 (Jan. 1905), pp. 132–148. doi: 10.1002/andp.19053220607.

[6] N. Bohr. "I. On the constitution of atoms and molecules". In: *The London, Edinburgh, and Dublin Philosophical Magazine and Journal of Science* 26.151 (July 1913), pp. 1–25. doi: 10.1080/14786441308634955.

[7] Couprie, Benjamin. *Institut International de Physique Solvay*. de. 1927. doi: 10.3932/ETHZ-A-000046848.

[8] W. Heisenberg. "Über quantentheoretische Umdeutung kinematischer und mechanischer Beziehungen." In: *Zeitschrift für Physik* 33.1 (Dec. 1925), pp. 879–893. doi: 10.1007/bf01328377.

[9] E. Schrödinger. "Quantisierung als Eigenwertproblem". In: *Annalen der Physik* 384.4 (Jan. 1926), pp. 361–376. doi: 10.1002/andp.19263840404.

[10] W. Heisenberg. “Über den anschaulichen Inhalt der quantentheoretischen Kinematik und Mechanik”. In: *Zeitschrift für Physik* 43.3–4 (Mar. 1927), pp. 172–198. doi: 10.1007/bf01397280.

[11] A. Einstein and M. Born. *Born-Einstein letters, 1916-1955*. en. Macmillan Science. Gordonsville, VA: Palgrave Macmillan, Dec. 2004.

[12] R. P. Feynman. “Simulating physics with computers”. In: *International Journal of Theoretical Physics* 21.6–7 (June 1982), pp. 467–488. doi: 10.1007/bf02650179.

[13] P. A. Benioff. “Quantum mechanical Hamiltonian models of discrete processes that erase their own histories: Application to Turing machines”. In: *International Journal of Theoretical Physics* 21.3–4 (Apr. 1982), pp. 177–201. doi: 10.1007/bf01857725.

[14] D. Deutsch. “Quantum theory, the Church–Turing principle and the universal quantum computer”. en. In: *Proc. R. Soc. Lond.* 400.1818 (July 1985), pp. 97–117.

[15] T. Harvey and C. I. of Technology. *Richard Feynman Lecturing on Quantum Mechanics*. Image. Accessed 21 Nov. 2024. May 1963.

[16] C. H. Bennett and G. Brassard. “Quantum cryptography: Public key distribution and coin tossing”. In: *Proceedings of IEEE International Conference on Computers, Systems and Signal Processing*. Bangalore, India, Dec. 1984, pp. 175–179.

[17] I. L. Chuang, L. M. K. Vandersypen, X. Zhou, D. W. Leung, and S. Lloyd. “Experimental realization of a quantum algorithm”. In: *Nature* 393.6681 (May 1998), pp. 143–146. doi: 10.1038/30181.

[18] L. M. K. Vandersypen, M. Steffen, G. Breyta, C. S. Yannoni, R. Cleve, and I. L. Chuang. “Experimental Realization of an Order-Finding Algorithm with an NMR Quantum Computer”. In: *Physical Review Letters* 85.25 (Dec. 2000), pp. 5452–5455. doi: 10.1103/physrevlett.85.5452.

[19] F. Arute, K. Arya, R. Babbush, D. Bacon, J. C. Bardin, R. Barends, R. Biswas, S. Boixo, F. G. S. L. Brandao, D. A. Buell, B. Burkett, Y. Chen, Z. Chen, B. Chiaro, R. Collins, W. Courtney, A. Dunsworth, E. Farhi, B. Foxen, A. Fowler, C. Gidney, M. Giustina, R. Graff, K. Guerin, S. Habegger, M. P. Harrigan, M. J. Hartmann, A. Ho, M. Hoffmann, T. Huang, T. S. Humble, S. V. Isakov, E. Jeffrey, Z. Jiang, D. Kafri, K. Kechedzhi, J. Kelly, P. V. Klimov, S. Knysh, A. Korotkov, F. Kostritsa, D. Landhuis, M. Lindmark, E. Lucero, D. Lyakh, S. Mandrà, J. R. McClean, M. McEwen, A. Megrant, X. Mi, K. Michielsen, M. Mohseni, J. Mutus, O. Naaman, M. Neeley, C. Neill, M. Y. Niu, E. Ostby, A. Petukhov, J. C. Platt, C. Quintana, E. G. Rieffel, P. Roushan, N. C. Rubin, D. Sank, K. J. Satzinger,

V. Smelyanskiy, K. J. Sung, M. D. Trevithick, A. Vainsencher, B. Villalonga, T. White, Z. J. Yao, P. Yeh, A. Zalcman, H. Neven, and J. M. Martinis. “Quantum supremacy using a programmable superconducting processor”. In: *Nature* 574.7779 (Oct. 2019), pp. 505–510. doi: 10.1038/s41586-019-1666-5.

[20] E. Pednault, J. Gunnels, D. Maslov, and J. Gambetta. *On "Quantum Supremacy"*. IBM Research Blog. Accessed 11 November 2024. Oct. 2019.

[21] G. Q. AI and Collaborators. “Quantum error correction below the surface code threshold”. In: *Nature* (Dec. 2024). doi: 10.1038/s41586-024-08449-y.

[22] C. Babbage. *On the Mathematical Powers of the Calculating Engine*. Unpublished manuscript. 1837.

[23] A. A. Lovelace. “Sketch of the analytical engine invented by Charles Babbage, by LF Menabrea, officer of the military engineers, with notes upon the memoir by the translator”. In: *Taylor’s Scientific Memoirs* 3 (1842), pp. 666–731.

[24] A. M. Turing. “On Computable Numbers, with an Application to the Entscheidungsproblem”. In: *Proceedings of the London Mathematical Society* 2 (1936), pp. 230–265. doi: 10.1112/plms/s2-42.1.230.

[25] M. R. Swaine and P. A. Freiberger. *Zuse computer*. Encyclopedia Britannica. Accessed 11 November 2024. Nov. 2015.

[26] R. “Der 8auer” Hartung. *14nm and 7nm are NOT what you think it is - Visiting Tescan Part 3/3*. Accessed 20 December 2024. 2020. url: https://www.youtube.com/watch?v=1kQUXpZpLXI.

[27] C. E. Shannon. “A Mathematical Theory of Communication”. In: *Bell System Technical Journal* 27.3 (July 1948), pp. 379–423. doi: 10.1002/j.1538-7305.1948.tb01338.x.

[28] G. W. A. Dummer. “Electronic Components in Great Britain”. In: *Proceedings Components Symposium*. Presented at the Washington DC Symposium. 1952, pp. 15–20.

[29] J. S. Kilby. *Miniaturized Electronic Circuits*. U.S. Patent 3,138,743. Filed February 6, 1959, issued June 23, 1964. 1959.

[30] R. H. Noyce. *Semiconductor Device-and-Lead Structure*. U.S. Patent 2,981,877. Filed July 30, 1959, issued April 25, 1961. 1961.

[31] G. E. Moore. “Cramming more components onto integrated circuits”. In: *Electronics Magazine* 38.8 (Apr. 1965). Originally presented as an internal paper at Fairchild Semiconductor in 1964, pp. 114–117.

[32] H. C. George, M. T. Mądzik, E. M. Henry, A. J. Wagner, M. M. Islam, F. Borjans, E. J. Connors, J. Corrigan, M. Curry, M. K. Harper, D. Keith, L. Lampert, F. Luthi, F. A. Mohiyaddin, S. Murcia, R. Nair, R. Nahm, A. Nethwewala, S. Neyens, B. Patra, R. D. Raharjo, C. Rogan, R. Savytskyy, T. F. Watson, J. Ziegler, O. K. Zietz, S. Pellerano, R. Pillarisetty, N. C. Bishop, S. A. Bojarski, J. Roberts, and J. S. Clarke. "12-Spin-Qubit Arrays Fabricated on a 300 mm Semiconductor Manufacturing Line". In: *Nano Letters* 25.2 (Dec. 2024), pp. 793–799. doi: 10.1021/acs.nanolett.4c05205.

[33] X. Xue, M. Russ, N. Samkharadze, B. Undseth, A. Sammak, G. Scappucci, and L. M. K. Vandersypen. "Quantum logic with spin qubits crossing the surface code threshold". In: *Nature* 601.7893 (Jan. 2022), pp. 343–347. doi: 10.1038/s41586-021-04273-w.

[34] A. Noiri, K. Takeda, T. Nakajima, T. Kobayashi, A. Sammak, G. Scappucci, and S. Tarucha. "Fast universal quantum gate above the fault-tolerance threshold in silicon". In: *Nature* 601.7893 (Jan. 2022), pp. 338–342. doi: 10.1038/s41586-021-04182-y.

[35] A. Mills, C. Guinn, M. Feldman, A. Sigillito, M. Gullans, M. Rakher, J. Kerckhoff, C. Jackson, and J. Petta. "High-Fidelity State Preparation, Quantum Control, and Readout of an Isotopically Enriched Silicon Spin Qubit". In: *Physical Review Applied* 18.6 (Dec. 2022). doi: 10.1103/physrevapplied.18.064028.

[36] S. G. J. Philips, M. T. Mądzik, S. V. Amitonov, S. L. de Snoo, M. Russ, N. Kalhor, C. Volk, W. I. L. Lawrie, D. Brousse, L. Tryputen, B. P. Wuetz, A. Sammak, M. Veldhorst, G. Scappucci, and L. M. K. Vandersypen. "Universal control of a six-qubit quantum processor in silicon". In: *Nature* 609.7929 (Sept. 2022), pp. 919–924. doi: 10.1038/s41586-022-05117-x.

[37] K. Takeda, A. Noiri, T. Nakajima, L. C. Camenzind, T. Kobayashi, A. Sammak, G. Scappucci, and S. Tarucha. "Rapid single-shot parity spin readout in a silicon double quantum dot with fidelity exceeding 99%". In: *npj Quantum Information* 10.1 (Feb. 2024). doi: 10.1038/s41534-024-00813-0.

[38] M. De Smet, Y. Matsumoto, A.-M. J. Zwerver, L. Tryputen, S. L. de Snoo, S. V. Amitonov, A. Sammak, N. Samkharadze, Ö. Gül, R. N. M. Wasserman, M. Rimbach-Russ, G. Scappucci, and L. M. K. Vandersypen. *High-fidelity single-spin shuttling in silicon*. 2024. doi: 10.48550/ARXIV.2406.07267.

[39] C. Jones, M. A. Fogarty, A. Morello, M. F. Gyure, A. S. Dzurak, and T. D. Ladd. "Logical Qubit in a Linear Array of Semiconductor Quantum Dots". In: *Phys. Rev. X* 8 (2 June 2018), p. 021058. doi: 10.1103/PhysRevX.8.021058.

[40] B. Undseth, O. Pietx-Casas, E. Raymenants, M. Mehmandoost, M. T. Madzik, S. G. J. Philips, S. L. de Snoo, D. J. Michalak, S. V. Amitonov, L. Tryputen, B. P. Wuetz, V. Fezzi, D. D. Esposti, A. Sammak, G. Scappucci, and L. M. Vandersypen. “Hotter is Easier: Unexpected Temperature Dependence of Spin Qubit Frequencies”. In: *Physical Review X* 13.4 (Oct. 2023). doi: 10.1103/physrevx.13.041015.

# 2

# THEORETICAL CONCEPTS

*One man's 'magic' is another man's engineering.*

Robert Heinlein

## 2.1. QUANTUM INFORMATION

Classical computers are the foundation of modern computing. They process information digitally, representing all data as sequences of zeros and ones. A single digit, the smallest unit of information, is called a bit. Eight bits make a byte (B), 1024 B make a KiB, and so on[1]. Similarly, a quantum computer uses a quantum bit (qubit) as its fundamental unit of information.

### DESCRIBING A SINGLE QUBIT

Like a classical bit, a qubit can represent a zero or a one. More formally, a qubit spans a two-dimensional Hilbert space $\mathbb{H}^2$, with a set of basis states e.g. $|0\rangle$ and $|1\rangle$. Any pure qubit state $|\Psi\rangle$ can be expressed as a linear combination of these basis states:

$$|\Psi\rangle = \alpha|0\rangle + \beta|1\rangle, \tag{2.1}$$

where $\alpha, \beta \in \mathbb{C}$ satisfy the normalization condition

$$|\alpha|^2 + |\beta|^2 = 1. \tag{2.2}$$

The basis states as well as generic pure qubit states can also be represented as vectors:

$$\begin{aligned} |0\rangle &= \begin{pmatrix} 1 \\ 0 \end{pmatrix} \\ |1\rangle &= \begin{pmatrix} 0 \\ 1 \end{pmatrix} \\ |\Psi\rangle &= \alpha \begin{pmatrix} 1 \\ 0 \end{pmatrix} + \beta \begin{pmatrix} 0 \\ 1 \end{pmatrix} = \begin{pmatrix} \alpha \\ \beta \end{pmatrix}. \end{aligned} \tag{2.3}$$

Through mathematical reformulations, the state of a qubit can be mapped onto the surface of a sphere, known as the Bloch sphere, illustrated in Fig. 2.1 **a**.

When restricted to the basis states, i.e., setting $\alpha, \beta \in \{0, 1\}$, a qubit can fully represent a classical bit. However, without this restriction, the qubit reaches states beyond what a classical bit can achieve. In such cases, the qubit is in a superposition of the basis states, existing in both states simultaneously. Fig. 2.1**a** depicts the most common superposition states, namely $|+\rangle, |+i\rangle, |-\rangle, |-i\rangle$, all of which share $|\alpha| = |\beta| = 1/\sqrt{2}$. The primary distinction among these states is the relative phase between the basis states. For instance, in the state $|+i\rangle$, the phase relationship is given by

$$|+i\rangle = \frac{1}{\sqrt{2}}(|0\rangle + \boldsymbol{i}|1\rangle) \tag{2.4}$$

[1] 1000 B=1 kB

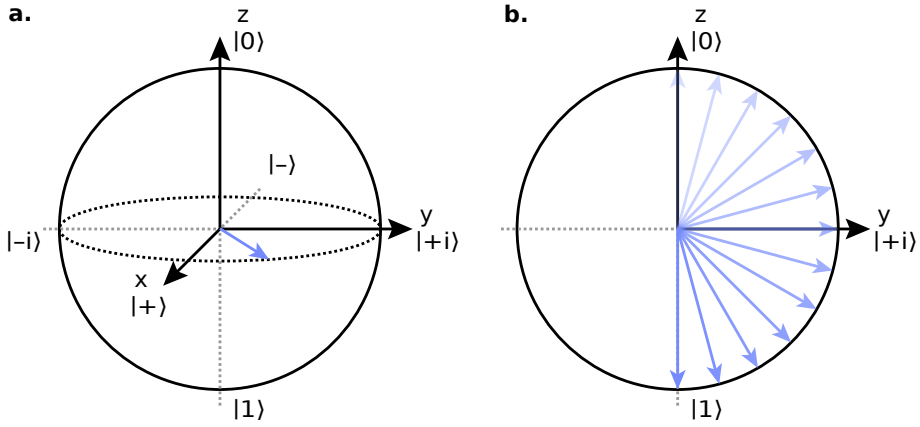


**Figure 2.1: Representation and manipulation of a Qubit visualised in the Bloch sphere. a.** Bloch sphere showing the six states along the carthesian axes along with an arbitrary qubit state in light blue. **b.** Rotation of a qubit from the $|0\rangle$ state to the $|1\rangle$ state when applying a $R_x(\pi)$ gate visualised in the yz-plane.

### MANIPULATING A QUBIT

Like a classical computer, a quantum computer must be capable of manipulating and transforming information. In classical computing, a single bit can only be flipped, and thus the NOT gate is the only non-trivial gate that acts on a single bit. Qubits, however, have more than two states available, requiring a broader set of gates to access them. Mathematically, a quantum gate is a unitary operator that, in a given basis, can be represented as a matrix. The classical NOT gate corresponds to the Pauli X ($\boldsymbol{\sigma}_x$) operator in quantum computing. Using Equation 2.3, we can express the action of this operator as:

$$|\psi'\rangle = \boldsymbol{\sigma}_x |\psi\rangle = \begin{pmatrix} 0 & 1 \\ 1 & 0 \end{pmatrix} \begin{pmatrix} \alpha \\ \beta \end{pmatrix}$$
$$= \begin{pmatrix} \beta \\ \alpha \end{pmatrix}$$

This demonstrates how the $\boldsymbol{\sigma}_x$ operator inverts the qubit state by swapping the coefficients $\alpha$ and $\beta$.

In the Bloch sphere representation, any single-qubit gate corresponds to a rotation around a specified axis by a given angle. The previously discussed NOT gate, for instance, is a rotation around the x-axis by an angle of $\pi$, as illustrated in Fig. 2.1**b**. More generally, arbitrary rotations are defined as:

$$R_{\vec{n}}(\phi) = e^{-i\frac{\phi}{2}(\vec{n}\cdot\vec{\boldsymbol{\sigma}})} \tag{2.5}$$

where $\vec{n}$ specifies the rotation axis, $\phi$ the rotation angle, and $\vec{\boldsymbol{\sigma}} = (\boldsymbol{\sigma}_x, \boldsymbol{\sigma}_y, \boldsymbol{\sigma}_z)^T$ denotes the vector of Pauli operators.



### MULTIPLE QUBITS

While a single qubit offers more possible states than a classical bit, its utility on its own remains limited. To describe multiple qubits, the Hilbert spaces of the individual qubits are combined using the tensor product.

$$\begin{aligned} |\Psi_1\Psi_2\rangle &= |\Psi_1\rangle \otimes |\Psi_2\rangle \\ &= (\alpha_1 |0_1\rangle + \beta_1 |1_1\rangle) \otimes (\alpha_2 |0_2\rangle + \beta_2 |1_2\rangle) \\ &= \alpha_1\alpha_2 |0_1 0_2\rangle + \alpha_1\beta_2 |0_1 1_2\rangle + \beta_1\alpha_2 |1_1 0_2\rangle + \beta_1\beta_2 |1_1 1_2\rangle \end{aligned} \tag{2.6}$$

Equation 2.6 can be simplified into Equation 2.7, which resembles the structure of Equations 2.1 and 2.2 from the single-qubit case:

$$\begin{aligned} |\Psi_1\Psi_2\rangle &= \alpha' |00\rangle + \beta' |01\rangle + \gamma' |10\rangle + \delta' |11\rangle, \\ |\alpha'|^2 + |\beta'|^2 + |\gamma'|^2 + |\delta'|^2 &= 1. \end{aligned} \tag{2.7}$$

This formalism extends naturally to two-qubit gates. Like single-qubit gates, which operate on a two-dimensional Hilbert space, two-qubit gates act on a four-dimensional Hilbert space. Common two-qubit gates are controlled or conditional rotations, where one qubit's state determines the rotation applied to another. A key example is the controlled-NOT (CNOT) gate, the quantum equivalent of the classical XOR gate. The CNOT gate applies a NOT operation to the target qubit if the control qubit is in the $|1\rangle$ state. Table 2.1 summarizes how the CNOT gate transforms the four computational basis states.

**Table 2.1:** CNOT gate acting on the four basis states under $|\Psi_{in}\rangle$ producing $|\Psi_{out}\rangle$. The left qubit is the control qubit, the right one the target qubit. The right half shows the truth table of the classical XOR gate as comparison.

| $\|\Psi_{in}\rangle$ | $\|\Psi_{out}\rangle$ | x,y | x,x⊕y |
|---|---|---|---|
| $\|00\rangle$ | $\|00\rangle$ | 0,0 | 0,0 |
| $\|01\rangle$ | $\|01\rangle$ | 0,1 | 0,1 |
| $\|10\rangle$ | $\|11\rangle$ | 1,0 | 1,1 |
| $\|11\rangle$ | $\|10\rangle$ | 1,1 | 1,0 |

In combination with arbitrary rotations around the cardinal axis of each single qubit the CNOT gate forms a universal set of quantum gates. Similar to the classical NAND or NOR gates any other gate or circuit can be represented by this gate set [1].

When considering multiple qubits another non-classical phenomenon arises: entanglement. When two or more qubits become entangled,

their states are no longer independent, meaning the properties of each qubit cannot be described individually. Instead, the system as a whole must be considered. A key consequence of this is that any operation or measurement performed on one qubit will instantaneously influence the state of the others, regardless of the physical distance separating them.

A well-known example of an entangled state is the Bell state $|\Phi^+\rangle$, where two qubits exist in a superposition of the $|00\rangle$ and $|11\rangle$ states:

$$|\Psi_1\Psi_2\rangle = |\Phi^+\rangle = \frac{1}{\sqrt{2}}|00\rangle + \frac{1}{\sqrt{2}}|11\rangle\,. \tag{2.8}$$

In this state, if one qubit is measured to be in the $|0\rangle$ state, the other qubit will also be $|0\rangle$. Similarly, if one qubit is found to be $|1\rangle$, the other must also be $|1\rangle$. Contrary to classical correlations the state of the two qubit remains in the superposition until the first measurement and both outcomes are possible. This perfect correlation between the qubits exists regardless of the distance between them [2, 3]. Today, entanglement is recognized as a crucial resource in quantum computing [4], enabling advanced algorithms and facilitating quantum communication between distributed quantum systems [5].

#### MEASURING QUBITS

To utilize these properties, the information encoded in qubits must be accessed or measured. Yet, this measurement process comes with fundamental limitations. The measurement is performed in a specific basis, e.g. the computational basis $|0\rangle, |1\rangle$, and the act of measurement irreversibly collapses the qubit's state into one of the states of this basis, erasing the original superposition and returning only one basis state. This collapse is inherently probabilistic, with the probability of collapsing into a basis state $|\nu\rangle$ determined by

$$P_\Psi(|\nu\rangle) = |\langle\nu|\Psi\rangle|^2\,. \tag{2.9}$$

Measuring in the computational basis, setting $|\nu\rangle = |1\rangle$,

$$P_\Psi(|1\rangle) = |\langle 1|\Psi\rangle|^2 = |\alpha\,\langle 1|0\rangle|^2 + |\beta\,\langle 1|1\rangle|^2 = |\beta|^2 \tag{2.10}$$

it becomes clear that the complex prefactors $\alpha$ and $\beta$ from Equations 2.1 and 2.2 are a direct measure for the probability to end up in the respective basis state. As a single measurement yields only one basis state multiple repetitions of the algorithm and measurement are needed to estimate $|\alpha|$ and $|\beta|$. To gain complete information of the qubit state it is necessary to perform quantum state tomography. This technique reconstructs the full quantum state by combining the outcomes of multiple measurements in different bases. In practice, however, noise

and other imperfections make it impossible to reconstruct a single pure state $|\Psi\rangle$, instead a density matrix is estimated.

For a pure state $|\Psi\rangle$, the density matrix $\rho$ is defined as

$$\rho = |\Psi\rangle\langle\Psi| = \begin{pmatrix}\alpha\\ \beta\end{pmatrix}\begin{pmatrix}\alpha^* & \beta^*\end{pmatrix} = \begin{pmatrix}|\alpha|^2 & \alpha\beta^*\\ \alpha^*\beta & |\beta|^2\end{pmatrix}. \tag{2.11}$$

But the density matrix can also be used to describe mixed states. Unlike pure states, which are described by a single state vector $|\Psi\rangle$, mixed states are statistical ensembles of different pure states $|\Psi_i\rangle$, each with an associated probability $p_i$. Then

$$\rho = \sum_i p_i |\Psi_i\rangle\langle\Psi_i|, \tag{2.12}$$

with $\sum_i p_i = 1$ ensuring normalization. Measuring a mixed state is described with a set of projective measurement operators $P_i$. The probability to measure the state corresponding to $P_i$ is given by

$$p(i) = Tr(P_i\rho) \tag{2.13}$$

where $Tr$ denotes the trace. This formalism is also used to calculate the updated state $\rho'$ after a projective measurement following

$$\rho' = \frac{P_i\rho P_i}{Tr(P_i\rho)}. \tag{2.14}$$

IN PRACTICE

With the mathematical framework of qubits and their operations established, one can translate these theoretical principles into practical requirements for physical implementations. David DiVincenzo identified five (computing) plus two (communication) key criteria that physical systems must meet to function as reliable quantum computers [6].

1. **Well-Defined Scalable Qubit:** Even in large-scale systems, qubits must remain distinguishable and preserve their two basis states.
2. **Deterministic Initialization:** A well-defined initial state is essential for drawing meaningful conclusions from the output. Therefore, it must be possible to deterministically initialize all qubits in a known, well-defined state.
3. **Coherence:** Qubits must retain the encoded information for a duration significantly longer than the gate time to ensure that algorithms can be executed with minimal information loss.
4. **Universal Set of Quantum Gates:** The system must support a universal set of quantum gates that enables any quantum computation.

5. **Readout:** After an algorithm is executed, the system must be capable of projectively measuring the state of all relevant qubits and retrieving their measurement outcome.

6. **Conversion between Stationary and Flying Qubits:** To enable communication between quantum computers, it must be possible to convert the quantum information stored in a stationary qubit of a quantum computer into a flying qubit that can be transported over large distances and back.

7. **Faithful Transmission of Flying Qubits:** Quantum information must be transferred between distant locations with high accuracy, preserving coherence.



## 2.2. IMPLEMENTING QUBITS IN SEMICONDUCTOR QUANTUM DOTS

Physically implementing a qubit can take many forms, each leveraging unique quantum properties to encode and manipulate information. Solid-state implementations, in particular, have emerged as a promising avenue. A common implementation is superconducting circuits that rely on Josephson junctions (JJs) to form anharmonic resonators capable of encoding a qubit. This work, however, focuses on the spin degree of freedom of an electron confined in a gate-defined quantum dot within a semiconductor material.

### 2.2.1. HETEROSTRUCTURES

The foundation to realising a qubit in a quantum dot is the semiconductor material stack. Typically a heterostructure of different materials is created that supports the formation of a 2D electron gas (2DEG) or 2D hole gas (2DHG) at an interface. Depending on the materials or additional doping the 2DEG can form naturally. Field effect gates akin to the gate of a field effect transistor (FET) can locally deplete the 2DEG to form a isolated region, the quantum dot. This operation mode is dubbed depletion mode. Alternatively, if the 2DEG does not form naturally, field effect gates can be used to accumulate a local 2DEG and form a quantum dot, in accumulation mode. Large “global” gates can be used to offset the energy landscape and switch between different modes. Fig. 2.2 shows two example heterostructures, with Fig. 2.2 **a** depicting a heterostructure in depletion mode, Fig. 2.2 **b** in accumulation mode.

For a long time a (doped) heterostructure of gallium arsenide (GaAs) and aluminium gallium arsenide (AlGaAs) (see Fig. 2.2**a**) was used. High mobility and low disorder enabled first experiments exhibiting quantum mechanical effects such as quantized conductance. Furthermore, the

low effective mass and intrinsic spin-orbit coupling (SOC) simplified the formation of quantum dots and spin qubits. However the noise originating from the high density of nuclear spins in GaAs materials ultimately limited qubit performance [7].

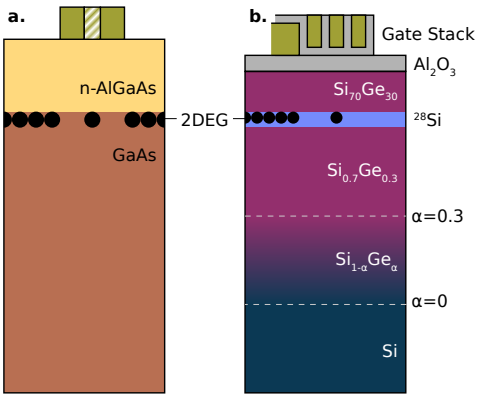


**Figure 2.2: Example heterostructures used to form quantum dots. a.** The negative dopants in the AlGaAs layer lets the GaAs/AlGaAs heterostructure operate in depletion mode. The gates locally deplete the 2DEG to form quantum dots. The plunger gate used to adjust the electrochemical potential of the quantum dot is shown as shaded area. **b.** In the Si/SiGe heterostructure, gates accumulate a 2DEG and quantum dots. Barrier gates are implemented to provide a better isolation between quantum dots and to the 2DEG. Image adopted from [7]

The transition to Group IV materials has been driven by their potential to mitigate this limitation. Both Silicon and Germanium based systems can be isotopically enriched such that the noise from nuclear spins is mitigated (see Section 2.2.3 *Coherence*). Common heterostructures are Si metal oxide semiconductor (MOS), a tensile strained Si quantum well between relaxed layers of $Si_{1-x}Ge_x$ where x is typically around 0.3 (see Fig. 2.2**b**) and a compressively strained Ge quantum well between relaxed layers of $Si_{1-x}Ge_x$ with x typically around 0.7 to 0.8. While the following paragraphs will focus on the properties of $Si/Si_{1-x}Ge_x$ heterostructures with low Germanium concentration a comprehensive overview of the different materials and their properties can be found in [7].

Starting with the band structure of bulk silicon, shown in Fig. 2.3 **a**, we observe a sixfold degeneracy of the conduction band minimum. The Brillouin zone lets us associate the degeneracy with six wave vectors, namely $\pm k_x$, $\pm k_y$ and $\pm k_z$. In $Si/Si_{1-x}Ge_x$, however, the minima associated with the $\pm k_x$ and $\pm k_y$ wave vectors are shifted upwards in energy due to the tensile strain (see Fig. 2.3 **b**). This tensile strain is created by the additional Ge atoms in the strain relaxed SiGe barriers, which increases the lattice constant of the crystal following the modified Vegard's law [8, 9]:

$$a_{Si_{1-X}Ge_X} = 0.5431 + 0.01992X + 0.002733X^2 (\text{nm}) \tag{2.15}$$

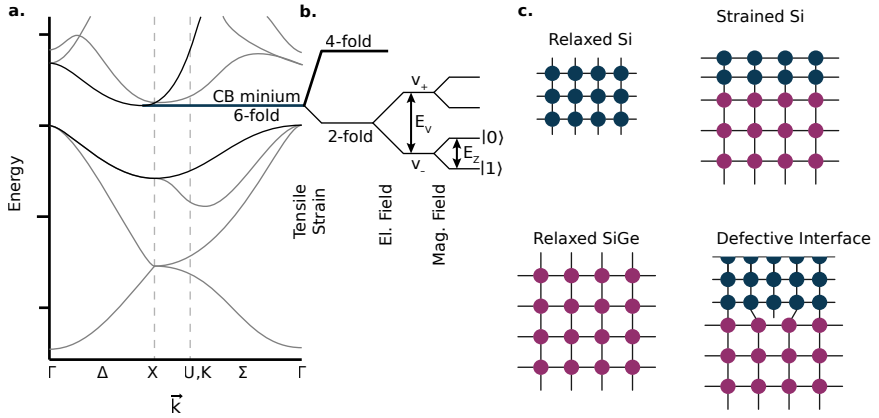


**Figure 2.3: Band diagram of silicon and effects of strain.** **a.** Section of the band diagram of bulk Si adopted from [10, 11] indicating the conduction band (CB) minimum. **b.** Schematic splitting of the 6-fold degeneracy of the conduction band minimum due to strain into a 4-fold and 2-fold degeneracy. Electric fields facilitate the split of the 2-fold degeneracy into a $v_-$ and a $v_+$ valley. The energy difference $E_v$ between the two lowest-energy valleys is called valley splitting. Lastly a magnetic field lifts the degeneracy of the two spin states by the Zeeman energy $E_Z$. **c.** Schematic of the Si and SiGe crystal in a relaxed state, and when brought into contact straining the Si layer to match the lattice constant of the SiGe. The third panel shows the formation of defects when the critical thickness is exceeded.

For $Si_{0.7}Ge_{0.3}$ the lattice constant is 1.15 % larger than the pure Si quantum well. For quantum wells below a critical thickness it is energetically favourable to adopt the larger lattice constant rather than forming dislocations as depicted in Fig. 2.3**c**. The critical thickness of a Si quantum well sandwiched between $Si_{70\%}Ge_{30\%}$ layers is estimated to be around 8 nm to 9 nm [12].

The remaining two valleys $\pm k_z$ are split by the electric fields of the field effect gates. It causes an overlap of the electron wave function with the SiGe barrier thus shifting the energy levels upwards. The exact overlap depends on the phase of the wave function thus shifting the two valleys by a different amount, splitting them apart in energy. This valley splitting typically ranges from 0 µeV to ∼ 500 µeV [13]. Due to alloy disorder, the random distribution of Ge atoms in the SiGe layer, the valley splitting is a stochastic property and highly position dependent [14].

An equally important material property is the SOC, which plays a critical role in the manipulation and coherence of qubits. In bulk silicon, the SOC is naturally weak due to the high symmetry of its diamond cubic lattice. This symmetry suppresses Dresselhaus SOC, while the absence of interfaces in the bulk material eliminates Rashba SOC [15, 16]. However, these bulk considerations are significantly altered in Si/SiGe heterostructures.

In heterostructures, the structural inversion asymmetry introduced by an external electric field or the confinement potential can induce Rashba SOC. Similarly, alloy disorder at the Si/SiGe interfaces disrupts the bulk inversion symmetry, giving rise to Dresselhaus SOC [17]. However, these effects are generally weak compared to those in other materials, such as III-V semiconductors or holes in Ge-based quantum dots. Furthermore, the SOC-induced corrections to the Landé $g$-factor are small for electrons in Si/SiGe quantum dots such that $g \approx 2$ remains a fair approximation.

### 2.2.2. QUANTUM DOTS

The term quantum dot encompasses a multitude of similar concepts, perhaps most notably optically active particles used in modern displays. Here, the term notes a zero-dimensional (0D) structure within a semiconductor heterostructure designed to trap a charged particle, such as an electron or a hole. The band structure of the heterostructure creating the 2DEG confines the particle in the vertical (z) direction. Lateral confinement (x/y direction) is created using electric fields from charged field effect gates as sketched in Fig. 2.2. By reducing the size of the box to around 100 nm, the continuous bands of the semiconductor crystal split into discrete levels, resulting in atom-like behaviour. The energy barriers isolating the box, combined with an addition energy well

exceeding the thermal energy ($k_B T \ll E_{\text{add}} \approx 1\,\text{meV}$), allow the system to hold a well-defined number of charge carriers, which can then be used to encode a qubit.

This ability to form a qubit within a semiconductor crystal using standard FET gates makes gate-defined quantum dots uniquely compatible with existing semiconductor technologies. The fabrication of gate-defined quantum dots is therefore able to leverage the well-established and highly uniform processes of the semiconductor industry [18–22]. This synergy also opens up opportunities for potential co-integration of quantum devices with classical electronics as shown in Fig. 2.4 [23–26].

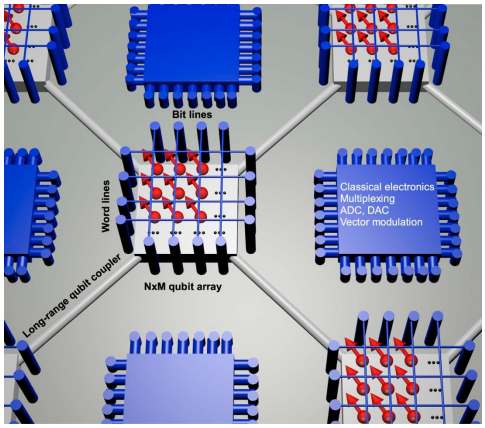


**Figure 2.4: Popular vision for a scalable architecture.** Leveraging compatibility of quantum dots and conventional electronics may allow the direct integration of both a quantum dot array hosting qubits and (parts of) the required control electronics on the same chip. In this proposal the qubit arrays are interlaced with the control electronics and then connected to each other via couplers. Image adopted from [23].

To describe the properties of a quantum dot we can look towards the Fermi-Hubbard model where each site represents a quantum dot. The Hamiltonian is written as

$$H = U \sum_i \boldsymbol{n}_{i\uparrow} \boldsymbol{n}_{i\downarrow} - t \sum_{\langle i,j \rangle, \sigma} \left( \boldsymbol{c}_{i\sigma}^\dagger \boldsymbol{c}_{j\sigma} + \text{h.c.} \right). \tag{2.16}$$

The first term describes the on-site interactions taking into account effects such as Coulomb repulsion. The parameter $U$ describes the on-site interaction strength while $\boldsymbol{n}_{i\updownarrow}$ is the number operator counting the electrons on site $i$ with spin $\uparrow$ or $\downarrow$.

The second term, the hopping term, describes the movement of electrons between lattice sites. Here $t$ denotes the tunnel coupling and $\boldsymbol{c}_{j\sigma}$ and $\boldsymbol{c}_{i\sigma}^\dagger$ are the annihilation and creation operators for an electron with spin $\sigma$ on lattice sites $i$ and $j$ respectively. Moving electrons e.g. by hopping along a quantum dot chain, can facilitate on-chip connectivity between quantum dot arrays, as illustrated in Fig. 2.4, where a long-range coupler is used to connect qubit patches. Alternative approaches to establish such connectivity such as superconducting resonators or other shuttling techniques are beyond the scope of this dissertation [27–32]. Additionally, the tunnel coupling influences the overlap of neighbouring electron wave functions, mediating exchange interaction - a fundamental mechanism used to implement quantum gates e.g. as

explained in Section 2.2.3 *Universal Gate Set*.

For gate-defined quantum dots these parameters can be adjusted using dedicated gates, making quantum dots a popular choice for simulating the various regimes of the Fermi Hubbard Model [33, 34]. Even though gates are typically designed to influence a single parameter, adjacent parameters retain a notable capacitive coupling. Thus changing a gate voltage will affect multiple parameters. This form of crosstalk can be avoided by using virtual gate voltages where $\vec{V}^{\text{virt}} = \mathbb{M}\vec{V}^{\text{real}}$ [33, 35]. The virtual gate matrix $\mathbb{M}$ contains the information on the capacitive coupling of a gate to all parameters with an example shown in Section 4.1 and Section 4.4.3. Changing a virtual voltage causes multiple physical voltages to change, which compensates the undesired couplings and allows each virtual gate to independently control one parameter.

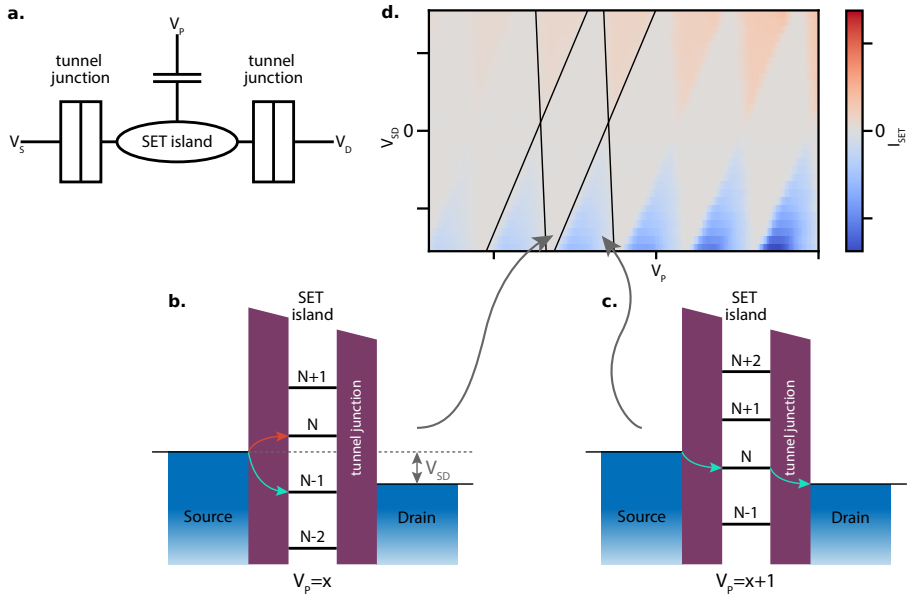


**Figure 2.5: Schematic and operation of a single electron transistor. a.** Schematic circuit of a SET. Tunnel junctions connect source and drain to the SET island, while the voltage $V_P$ couples capacitatively to it. **b.** The arrangement of the discrete electrochemical potential levels of the SET island ($N-2$ to $N+1$) prevents electrons from entering or leaving it (red arrows) **c.** Adjusting $V_P$ shifts the electrochemical potential levels such that electrons can enter and leave the SET island. **d.** Sweeping $V_P$ and $V_{SD}$ shows the characteristic diamond shape, Coulomb diamonds, where transport is blocked.

To accurately determine and control the exact number of charges

on a quantum dot, a charge sensor such as the single electron transistor (SET) is required. A SET is a quantum dot with an arbitrary number of electrons while also coupled to two reservoirs as shown in Fig. 2.5**a**. The Coulomb interaction between the electrons on the SET island prevents the addition of more electrons to the island unless the addition energy $E_{\mathrm{add}}$ is overcome. The positioning of the energy levels shown in Fig. 2.5**b**. also prevents electrons from leaving the SET island, thus prohibiting any electron movement from source to drain. The SET is blockaded.

By changing the voltage of the plunger gate $V_{\mathrm{P}}$ it is possible to change the electrochemical potential of the SET. By aligning the energy levels of source, drain and the SET as shown in Fig. 2.5**c** electrons can tunnel from source to the SET to drain causing an electrical current. The larger the source-drain-bias $V_{\mathrm{SD}}$ the larger the voltage range of $V_{\mathrm{P}}$ at which this process is possible. Fig. 2.5**d** shows this dependency of the current through a SET depending on the source-drain-bias $V_{\mathrm{SD}}$ and the plunger gate voltage $V_{\mathrm{P}}$. The sharpness of the Coulomb peaks, the periodic spikes in electrical current as $V_{\mathrm{P}}$ is changed, allows the detection of changes to the electrical environment of the SET. Even the movement or addition of single electrons on adjacent quantum dots causes a large enough shift to the electro chemical potential of the SET that the corresponding change in current can be detected.

In modern SETs, the traditional measurement of current through the device is increasingly being replaced by an radio frequency (RF)-impedance measurement. An additional tank circuit using parasitic capacitances and a superconductor with high kinetic inductance creates a resonance in the $\sim 100\,\mathrm{MHz}$ regime. The quality factor $Q$ of the resonance directly depends on the impedance of the SET, which changes as the Coulomb blockade is lifted. Analysing the reflected signal will therefore exhibit similar Coulomb peaks as a current measurement. By operating in the RF regime with higher bandwidth, measurements can be performed orders of magnitude faster than with traditional DC methods [36]. The higher frequency also improves the signal-to-noise ratio as the amplification chain often suffers from $1/f$ noise. Additionally, with minor modifications to the tank circuit, RF-SETs can operate with only one reservoir, simplifying the device architecture while retaining sensitivity [37, 38].

Despite its advantages, the RF approach is not without challenges. Additional components such as the tank circuit require space. Moreover, amplifiers in the RF readout chain dissipate power, adding heat to cryogenic environments and complicating thermal management.

### 2.2.3. SPIN QUBITS IN SI/SIGE QUANTUM DOTS

Once a single electron is confined in a quantum dot it can be used to implement a qubit. This topic is split into sections loosely following the previously discussed DiVincenzo criteria.



#### WELL-DEFINED QUBIT

Various properties of an electron can be used to encode a qubit. Confining one electron in two quantum dots one can use the quantum dots as basis states with the position of the electron within as quantum degree of freedom. But the electron provides a more intuitive way to encode a qubit, namely its intrinsic angular momentum or spin. A spin-$\frac{1}{2}$ particle such as the electron possesses precisely two distinct spin states, spin up ($|\uparrow\rangle$) and spin down ($|\downarrow\rangle$). These spin states, however, are degenerate in energy. It can be lifted by applying a magnetic field, which gives rise to the Zeeman splitting (see Fig. 2.3**b**). This system is then described by the Hamiltonian

$$\mathbf{H}_{\text{Static}} = \frac{1}{2} g \mu_B \vec{B} \cdot \vec{\boldsymbol{\sigma}} \tag{2.17}$$

assuming $\hbar = 1$ and with $g$ as Landé g-factor, $\mu_B$ the Bohr magneton, $\vec{B}$ the magnetic field vector and $\vec{\boldsymbol{\sigma}}$ the vector of Pauli operators as defined previously. The magnetic field does not only energetically split the two spin states it also causes the magnetic moment to rotate around the field axis, a fact we will make extensive use of in Chapter 5. The frequency $f_L$ of this Larmor precession is proportional to the magnitude of the magnetic field $hf_L = g\mu_B \left|\vec{B}\right|$, with typical values ranging between 5 GHzand25 GHz.

To simplify the model, the Larmor precession can be removed by switching to a rotating reference frame. Assuming the magnetic field is in the z-direction the Hamiltonian changes in this rotating frame to

$$\mathbf{H}_{\text{Rot,Static}} = \frac{\Delta}{2} \boldsymbol{\sigma}_z \tag{2.18}$$

with the detuning $\Delta = g\mu_B B_Z - hf_{\text{Frame}}$. By exactly matching the frequency of the reference frame with the qubit frequency, i.e. setting $\Delta = 0$, the qubit stops rotating in the Bloch sphere.

This mathematical description of the electron as pure two-level system has a notable shortcoming. It ignores quantum degrees of freedom such as valley or orbital states. While the orbital splitting is generally large compared to the Zeeman energy, the lowest valley states can be comparable in energy or even lower. As several studies showed, this will cause issues for initialisation, readout, gates, and coherence [39–42].

#### INITIALISATION AND READOUT

Initializing the spin qubit is intertwined with its readout. Reading a qubit collapses its wave function into a basis state, determining the measurement outcome. Hence by reading a qubit it can be brought into a well-defined initial state. Measuring the spin state of an electron directly is infeasible as its magnetic moment is extremely small. Instead the information encoded in the spin can be converted into a charge state. The latter can be more easily detected using a charge detector as introduced in Section 2.2.2. Fig. 2.6 shows the two most common methods for spin to charge conversion: Elzerman readout and Pauli spin blockade (PSB) readout [43–45]. The former method relies on aligning the two spin levels to a reservoir such that only an electron occupying the energetically higher spin state is permitted to leave the quantum dot (see Fig. 2.6**a**). The rate at which an electron with spin down can leave and an electron with spin up can re-enter the quantum dot is set by the tunnel coupling to the reservoir. By monitoring the charge sensor, these two tunnelling events can be detected as shown by the traces in Fig. 2.6**b**. The presence (absence) of the blip then can be related to the electron being in spin down (up). This procedure is well known but has two major flaws. First, each qubit needs access to a reservoir, which becomes impractical in even medium sized arrays. Secondly, the occupation of the reservoir follows a Fermi-Dirac distribution, making the width of the reservoir line temperature dependent. This broadening stochastically allows spin up electrons to leave the quantum dot causing a false detection. Increasing the temperature will increase the probability of this event thus reducing the state preparation and measurement (SPAM) fidelity [46].

Both of the two short comings can be mitigated by using PSB readout. It relies on the Pauli exclusion principle that prevents two fermions from occupying the same quantum state. This exclusion can be leveraged by trying to move an electron from one quantum dot into a quantum dot with another electron i.e. going from the $(N_1, N_2) = (1, 1)$ to the $(0, 2)$ charge state where $N_i$ denotes the occupation of the $i$th quantum dot. If the two spin states align, the electron cannot tunnel to the second quantum dot, instead it is blockaded. The system will remain in the $(1, 1)$ charge state. Loosely speaking, if the spin states are antiparallel, however, the moving electron is not blockaded and will tunnel into the second quantum dot and form the $(0, 2)$ charge state. Both options are depicted in Fig. 2.6**c**. As before the spin information is mapped onto different charge states that can be detected with a charge sensor.

The list of (non) blockaded states depends on minute details of the system, such as ramp speeds, Zeeman energies and SOC [45]. Typically all three triplet states, $T_+$, $T_0$ and $T_-$ are blockaded while only the singlet state S is not. The PSB readout scheme is then called singlet-triplet readout. However, a large Zeeman energy difference between the two

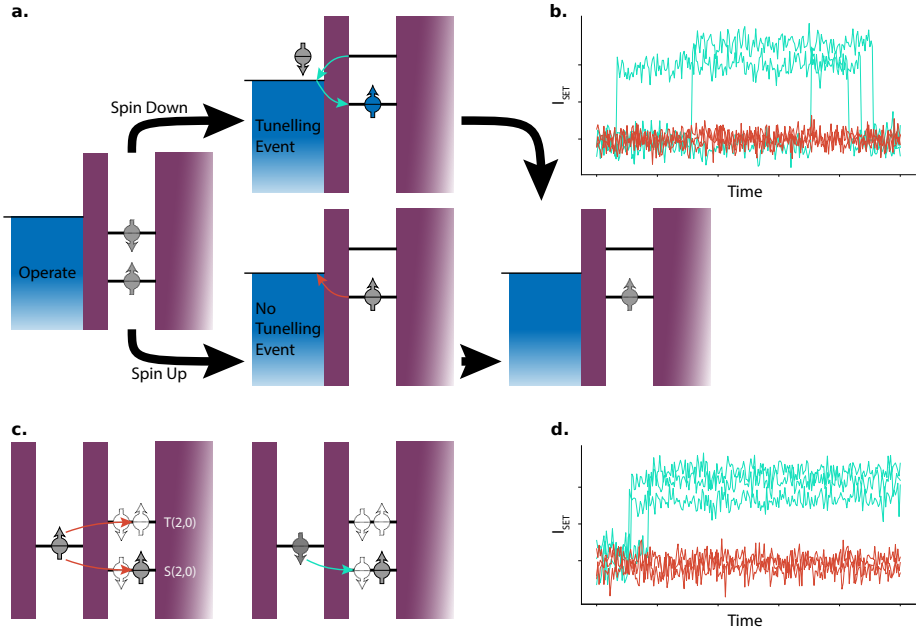


**Figure 2.6: Schematics of charge readout methods.** **a.** Readout scheme for Elzerman readout. A spin down electron can leave the quantum dot in the second phase and is instead replaced with a spin up electron from the reservoir. The two tunnelling events cause a blip to appear in the illustrated readout traces as indicated in **b.** (turquoise). This is contrasted by the spin up electron which cannot tunnel and no blip appears in the readout traces (red) **c.** PSB readout relies on the Pauli exclusion principle which prevents the electron in the left panel to tunnel to the other quantum dot. The system remains in the $(N_1, N_2) = (1, 1)$ charge state. A spin down electron as depicted in the right panel can form a singlet state and thus can enter the other quantum dot and form a $(0, 2)$ charge state. **d.** Illustrated readout traces with red (turquoise) lines corresponding to the left (right) panel.

quantum dots causes the $T_0$ triplet to relax faster than state-of-the-art charge detection schemes can resolve. Thus, only even parity states ($T_+$ and $T_-$) are blockaded while for states with odd parity the blockade is lifted. The singlet-triplet readout is thus transformed into a parity readout [45, 47].

Initialization using PSB can be performed through several methods, all of which begin in the $(0, 2)$ and evolve into the $(1, 1)$ charge configuration. In the $(0, 2)$ state, the two spins form a singlet state, $S_{(0,2)}$. If the system is ramped diabatically with respect to spin through all anticrossings, the singlet state is preserved, and the system transitions into the $S_{(1,1)}$ state initialising an entangled state. Achieving full adiabaticity instead can prove challenging due to the small size of the S-$T_-$ anticrossing. However, in certain materials where this anticrossing is more pronounced, the $T_-$ state can be successfully initialized by ramping fully adiabatically. Alternatively, if the system passes through the S-$T_-$ anticrossing diabatically and then continues adiabatically, it will initialize one of the odd-parity triplet states, depending on the relative Zeeman energies of the two quantum dots involved [47].

While this readout method is less sensitive to temperature and requires only a second qubit instead of a reservoir it also has flaws. Without additional tricks the retrieved information is reduced from one bit per qubit to one bit per two qubits. Also initialisation methods are more involved than for Elzerman readout. While Elzerman readout always initialises the lower spin state, PSB conditions a successful initialisation on starting in the $(0, 2)$ charge regime which is not achieved in every measurement. Beyond that, the Landau-Zener transitions in the involved anticrossings can limit the SPAM fidelity.

Both Elzerman and PSB readout require charge sensors to detect the charge movement. Its inclusion in large scale architectures, particularly with dense qubit arrays can be challenging. This has motivated the development of alternative readout methods, such as dispersive readout. Dispersive readout relies on coupling a double quantum dot to a high-quality-factor resonator, which becomes sensitive to the quantum capacitance of the system. The spins state of the quantum dot system modifies the electrical susceptibility, leading to a measurable shift in the resonator's frequency or phase. Using an adequate reflectometry set up these changes can be detected thus giving information on the spin states of the involved quantum dots [48–50].

#### UNIVERSAL GATE SET

To manipulate the spin state an RF magnetic field can be applied, orthogonal to the static field. As the spin precesses around the static magnetic field along the z-axis, the orthogonal magnetic field has to rotate in the xy-plane. The amplitude of this rotating field, the driving field, is denoted by $B_1$. In the non-rotating frame, the lab frame, the

Hamiltonian of Equations 2.17 changes to

$$\mathbf{H}_{\text{Driven}} = \frac{1}{2} g\mu_B \begin{pmatrix} B_1 \cos(2\pi f_{\text{Drive}} t) \\ B_1 \sin(2\pi f_{\text{Drive}} t) \\ B_0 \end{pmatrix} \cdot \vec{\boldsymbol{\sigma}}, \tag{2.19}$$

assuming that $\vec{B} = (0, 0, B_0)^{\mathrm{T}}$ and with $f_{\text{Drive}}$ denoting the frequency of the driving field. Perfectly matching all three frequencies, the Larmor frequency of the qubit $f_L$, the frequency of the drive $f_{\text{Drive}}$ and the frequency of the rotating frame $f_{\text{Frame}}$ changes the Hamiltonian of Equations 2.18 to

$$\mathbf{H}_{\text{Rot,Driven}} = B_1 \boldsymbol{\sigma}_{\text{x}}, \tag{2.20}$$

which causes the spin to rotate around the x-axis. These resulting oscillations in the spin up probability are called Rabi oscillations. By changing the phase of the drive one can rotate around any axis in the xy-plane. However, applying such an rotating magnetic field is impractical. It is significantly easier to apply a linearly polarized field, i.e. an oscillating field along a fixed axis:

$$\mathbf{H} = \frac{1}{2} g\mu_B \begin{pmatrix} 2B_1 \cos(2\pi f_{\text{Drive}} t) \\ 0 \\ B_0 \end{pmatrix} \cdot \vec{\boldsymbol{\sigma}}. \tag{2.21}$$

Transforming this into the rotating frame will give rise to additional non secular terms which can, under the rotating wave approximation, safely be ignored. The Hamiltonian of Equations 2.20 remains valid.

This linearly polarized magnetic field can be implemented by driving an RF current through a shorted antenna. The current induces an alternating magnetic field which induces Rabi oscillations. This approach is commonly known as electron spin resonance (ESR) [51].

An popular alternative relies on SOC and is called electric-dipole spin resonance (EDSR). In EDSR, an oscillating electric field is applied to modulate the position of the quantum dot. This charge motion interacts with the electron spin through SOC, which acts as a bridge between the orbital and spin degree of freedom.

However, for electrons in Si/SiGe the intrinsic SOC is too small for efficient driving. Instead the transversal gradient of a static magnetic field can be used as artificial SOC. More intuitively this method can be seen as shaking the electron in a magnetic field gradient causing the electron to experience an effective oscillating magnetic field. The magnetic field amplitude of the drive $B_1$ is proportional to the magnetic field gradient $dB_\perp/dx$ and the amplitude of the electric drive $E_x$ [41, 52].

Commonly this is implemented with a magnetic on-chip structure, the micromagnet. After magnetizing it at sufficiently high fields its shape modulates the external field on the required length scales thus

providing the transversal magnetic field gradient. Aside from this, the micromagnet can also provide a longitudinal field gradient which makes the Zeeman energy position dependent. Electrons in different quantum dots will then have different Larmor frequencies, enabling addressability of individual qubits in frequency space [47, 52].

A third alternative to manipulate a spin state without an active microwave drive was demonstrated in Ge/SiGe by Wang et al. [53]. They induced rotations around a new rotation axis by diabatically transferring a hole spin from one quantum dot to another. The direction of this new rotation axis is set by the difference in quantisation axes between the two quantum dots caused by variations in the local $g$-tensor. Chapter 5 shows how this method can be implemented in Si/SiGe with variations in the magnetic field orientation instead.

Two-qubit gates are commonly implemented using the Heisenberg exchange interaction. The Hamiltonian for two electron spins with a magnetic field along the z-axis is

$$\mathbf{H}_{\text{Heis}} = \frac{1}{2} g\mu_B \left( B_z^1 \boldsymbol{\sigma}_z^1 + B_z^2 \boldsymbol{\sigma}_z^2 \right) + \frac{J}{4} \left( \vec{\boldsymbol{\sigma}}^1 \cdot \vec{\boldsymbol{\sigma}}^2 - 1 \right). \tag{2.22}$$

The first term in the Hamiltonian represents the evolution of each individual spin as described by Equations 2.17, where the superscripts denote the two qubits. The second term models the interaction between the two spins, with $J$ representing the Heisenberg exchange interaction. The energies of the four basis states as well as the eigenstates and their energies are shown in Fig. 2.7. Depending on the strength of the exchange interaction, different two-qubit gates can be implemented.

For a strong exchange interaction, where $J >> h|f_L^1 - f_L^2|$, the eigenstates of the system are no longer those of the individual spins. Instead, with the exchange interaction dominating the system's behaviour, the eigenstates are singlet- and triplet-like states. In this regime, the two qubits continuously exchange energy, resulting in SWAP oscillations that can be used as an entangling mechanism. On the other hand, when $J << h|f_L^1 - f_L^2|$, the off-diagonal terms of the Heisenberg exchange Hamiltonian become non-secular and can be neglected. In this case, the Hamiltonian becomes Ising-like, dominated by the ZZ-interaction, which can be used to implement a controlled phase gate (CZ).

Alternatively, by applying an appropriate microwave drive in the weak exchange regime, a controlled rotation or CROT gate can be implemented. The slight shift of the odd parity energy levels allows to selectively drive one transition conditional on the other qubit as indicated by the highlighted frequencies in Fig. 2.7.

To characterize experimental realizations of single- and two-qubit gates, one can calculate their fidelity, which measures how closely the experimentally implemented operation matches the desired target

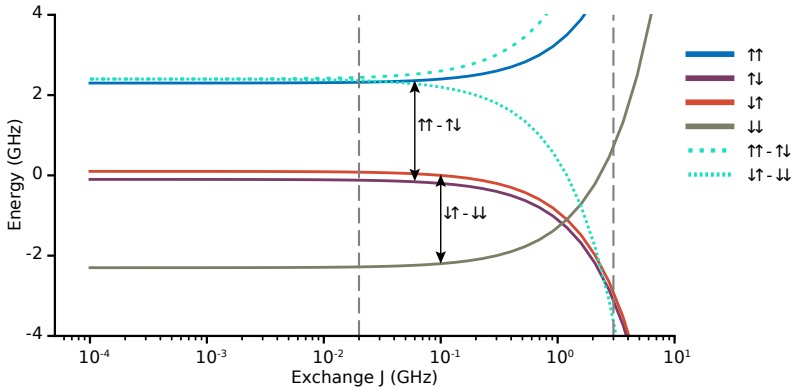


**Figure 2.7: Simulated two qubit Hamiltonian with Heisenberg exchange.** Plotted are the energies of the four computational basis states depending on the exchange interaction $J$, assuming $f_1 = 1.1\,\mathrm{GHz}$ and $f_2 = 1.2\,\mathrm{GHz}$. The gray dashed lines indicate regions where a CZ (left) or SWAP (right) gate may be executed. A CROT gate can be implemented due to the frequency differences between $\uparrow\uparrow - \uparrow\downarrow$ and $\downarrow\uparrow - \downarrow\downarrow$ as indicated by the turquoise dotted lines and the respective arrows.

operation. The average gate fidelity $\bar{F}(\mathscr{E}, U)$ is defined as the overlap of the initial state and the state after applying the experimental realisation of a quantum gate $\mathscr{E}$ and the inverse of the corresponding target operation $U^\dagger$ averaged over all possible input states:

$$\bar{F}(\mathscr{E}, U) = \int d\Psi \, \langle\Psi| U^\dagger \mathscr{E}(\Psi) U |\Psi\rangle \,. \tag{2.23}$$

This can be simplified into,

$$\bar{F}(\mathscr{E}, U) = \frac{1}{d^2} \left|\mathrm{tr}(\mathscr{E} U)\right|^2 , \tag{2.24}$$

where $d$ denotes the dimensionality of the Hilbert space [54]. Measuring $\mathscr{E}$, however, is not trivial and with randomized benchmarking (RB) a more practical tool was developed. RB measures the gate fidelity averaged over a set of gates, typically the Clifford gates. To measure the average Clifford gate fidelity $\overline{F_{\mathrm{Clif}}}$ a random sequence of Clifford gates is applied to a initial state, followed by a single operation that inverts the unitary produced by the sequence of Clifford gates, ideally returning the system to its initial state. Analysing the probability of successful state recovery as a function of the sequence length $l$ provides a decay curve

which is linked to the average Clifford gate fidelity

$$P_{\text{return}}(l) = a\overline{F_{\text{Clif}}}^{l} + o. \tag{2.25}$$

Here, $a$ and $o$ are fit parameters that account for experimental imperfections such as SPAM errors. Experimental demonstrations of RB are presented in Fig. 5.2 and Fig. 5.4 with details on the methodology in Section 5.6.3.

A significant advantage of RB is its resilience to state preparation and measurement (SPAM) errors. The decay rate primarily reflects errors that occur during the application of the random gate sequences, effectively isolating the measurement from SPAM contributions.

While RB provides a global measure of average gate fidelity across a set of quantum gates, it does not offer detailed insight into the performance of individual gates or specific error sources such as systematic errors due to miscalibration or decoherence [55, 56].

#### COHERENCE

The performance and stability of quantum gates are fundamentally tied to the coherence properties of the underlying quantum system. Coherence quantifies the ability of a qubit to preserve its quantum state over time, and its degradation is a primary source of errors in quantum computations. Two key processes contribute to the loss of coherence: relaxation and dephasing.

Relaxation describes the process of losing energy to the environment and relaxing from an excited state to the thermal equilibrium state. The measurement procedure to measure the $e^{-1}$ decay time $T_1$ is depicted in Fig. 2.8**a**. The process of spin relaxation is mediated by phonons, which absorb energy through lattice vibrations. These vibrations generate electric field fluctuations that couple to the spin via SOC or, in systems with abundant nuclear spins, through hyperfine interactions. Under typical conditions, weak SOC and low nuclear spin density result in a relaxation time $T_1$ that is several orders of magnitude longer than average gate times. However, at hotspots where the Zeeman energy matches the valley splitting the resonance condition significantly enhances spin-phonon coupling. This leads to a drastic reduction in $T_1$, as illustrated in Fig. 2.8**d** [40, 57, 58].

Dephasing on the other hand scrambles the phase information of the qubit without energy loss to the environment. The dephasing time $T_2$ is bound by the relaxation time $T_1$, with $T_2 \leq 2T_1$. It reflects the intrinsic coherence of the qubit.

In contrast, $T_2^*$ describes the coherence time in the presence of both intrinsic decoherence and external noise. It is measured using a Ramsey experiment, where the qubit is brought into a superposition state and after a free evolution time rotated back and measured as shown in

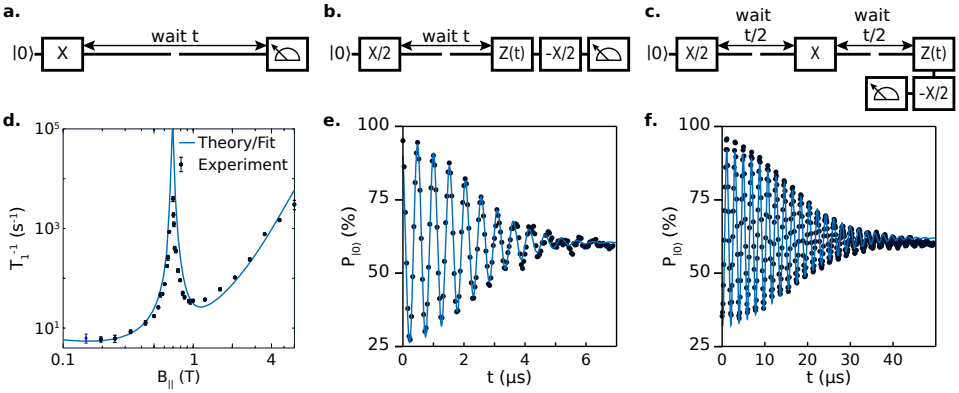


**Figure 2.8: Protocol schematics and examples for relaxation and coherence measurements.** Measurement sequence for a **a.** $T_1$, **b.** $T_2^*$, **c.** $T_2^H$ measurement. **d.** $T_1$ decay rate depending on the external magnetic field, showing a peak due to spin-valley mixing. Image adopted from [59, 60] **e.** $T_2^*$ measurement showing the return probability depending on idle time. **f.** $T_2^H$ measurement showing the return probability depending on idle time.

Fig. 2.8**b**. Without noise the qubit would always return to the initial basis state. A random phase accumulation due to noise will change the return state. By averaging over multiple repetitions the return probability decays to 50 %. In practice an artificial detuning is introduced to induce the oscillations in Fig. 2.8**e**, which allows for a more precise fit of the decay. These artificial oscillations can also be used to accurately determine the qubit frequency.

In case of slow dephasing noise an echo sequence is able to counteract the random phase shift. For that the qubit is periodically flipped as shown in Fig. 2.8**c,f**. Noise that is relatively static for such time periods will accumulate in one period and cancel or echo itself out in the second period, thus increasing the dephasing time. This procedure can be repeated and extended in various different ways [61, 62].

Main contributors to the dephasing of an electron spin are nuclear spins and charge noise. The former interact with the electron spin due to hyperfine interaction. The sum of which create a random effective magnetic field, the Overhauser field, which changes the precession frequency of the qubit. In Equations 2.18 the parameter $\Delta$ becomes non-zero and the qubit starts precessing at a random speed. In GaAs this was a major problem as all nuclei carry a spin. However, in Group IV materials the majority of nuclei are spinless. Specifically for Silicon and Germanium only $^{29}$Si and $^{73}$Ge have a non-zero nuclear spin. Both have an abundance of 4.7 % and 7.8 % respectively. It is possible to further

reduce these numbers using isotopically enriched materials. For the experiments in the Chapter 4 and Chapter 5 the residual concentration of $^{29}$Si in the quantum well was reduced to 800 ppm. Though, the optimal residual concentrations of $^{29}$Si and $^{73}$Ge at which resulting nuclear noise can be considered negligible remains an active area of research [63].

Charge noise on the other hand encompasses electrical noise in the system, which can change the potential landscape and thus perturb the energy levels of a quantum dot. While the magnetic moment of the spin is in principle insensitive to charge fluctuations, SOC provides an interaction mechanism. An intuitive example is the longitudinal magnetic field gradient provided by a micromagnet. As discussed in Section 2.2.3 *Universal Gate Set* the gradient makes the Zeeman energy position dependent and thus allows for spectral addressability of different quantum dots. However, this spatial dependency of the Zeeman energy is not restricted to inter dot distances. Tiny variations to the quantum dot position induced by charge noise also modulate the qubit frequency which in turn causes the detuning $\Delta$ to become noise and time dependent. As before this leads to unwanted and uncontrollable phase changes of the spin qubit [64].

Charge noise originates from various sources, including defects and traps in the surrounding materials or charge dynamics at nearby interfaces. These defects are commonly modelled as two-level fluctuators, each characterized by a Lorentzian spectral shape centred around its switching rate. When numerous fluctuators with a wide range of switching rates are present, their individual contributions combine to produce the characteristic $1/f$-like behaviour observed in charge noise measurements [65, 66].

# REFERENCES


[1] A. Barenco, C. H. Bennett, R. Cleve, D. P. DiVincenzo, N. Margolus, P. Shor, T. Sleator, J. A. Smolin, and H. Weinfurter. “Elementary gates for quantum computation”. In: *Physical Review A* 52.5 (Nov. 1995), pp. 3457–3467. doi: 10.1103/physreva.52.3457.

[2] B. Hensen, H. Bernien, A. E. Dréau, A. Reiserer, N. Kalb, M. S. Blok, J. Ruitenberg, R. F. L. Vermeulen, R. N. Schouten, C. Abellán, W. Amaya, V. Pruneri, M. W. Mitchell, M. Markham, D. J. Twitchen, D. Elkouss, S. Wehner, T. H. Taminiau, and R. Hanson. “Loophole-free Bell inequality violation using electron spins separated by 1.3 kilometres”. In: *Nature* 526.7575 (Oct. 2015), pp. 682–686. doi: 10.1038/nature15759.

[3] S. J. Freedman and J. F. Clauser. “Experimental Test of Local Hidden-Variable Theories”. In: *Physical Review Letters* 28.14 (Apr. 1972), pp. 938–941. doi: 10.1103/physrevlett.28.938.

[4] P. W. Shor. “Algorithms for quantum computation: discrete logarithms and factoring”. In: *Proceedings 35th Annual Symposium on Foundations of Computer Science*. SFCS-94. IEEE Comput. Soc. Press, 1994, pp. 124–134. doi: 10.1109/sfcs.1994.365700.

[5] C. H. Bennett and G. Brassard. “Quantum cryptography: Public key distribution and coin tossing”. In: *Proceedings of IEEE International Conference on Computers, Systems and Signal Processing*. Bangalore, India, Dec. 1984, pp. 175–179.

[6] D. P. DiVincenzo. “The Physical Implementation of Quantum Computation”. In: *Fortschritte der Physik* 48.9–11 (Sept. 2000), pp. 771–783. doi: 10.1002/1521-3978(200009)48:9/11<771::aid-prop771>3.0.co;2-e.

[7] G. Scappucci, P. J. Taylor, J. R. Williams, T. Ginley, and S. Law. “Crystalline materials for quantum computing: Semiconductor heterostructures and topological insulators exemplars”. In: *MRS Bulletin* 46.7 (July 2021), pp. 596–606. doi: 10.1557/s43577-021-00147-8.

[8] J. P. Dismukes, L. Ekstrom, and R. J. Paff. “Lattice Parameter and Density in Germanium-Silicon Alloys1”. In: *The Journal of Physical Chemistry* 68.10 (Oct. 1964), pp. 3021–3027. doi: 10.1021/j100792a049.

[9] D. J. Paul. “Si/SiGe heterostructures: from material and physics to devices and circuits”. In: *Semiconductor Science and Technology* 19.10 (Sept. 2004), R75–R108. doi: 10.1088/0268-1242/19/10/r02.

[10] J. R. Chelikowsky and M. L. Cohen. “Electronic structure of silicon”. In: *Physical Review B* 10.12 (Dec. 1974), pp. 5095–5107. doi: 10.1103/physrevb.10.5095.

[11] W. Commons. *File:Band structure Si schematic.svg — Wikimedia Commons, the free media repository*. [Online; accessed 17-January-2025]. 2023.

[12] Y. Liu, K.-P. Gradwohl, C.-H. Lu, T. Remmele, Y. Yamamoto, M. H. Zoellner, T. Schroeder, T. Boeck, H. Amari, C. Richter, and M. Albrecht. “Role of critical thickness in SiGe/Si/SiGe heterostructure design for qubits”. In: *Journal of Applied Physics* 132.8 (Aug. 2022). doi: 10.1063/5.0101753.

[13] B. Paquelet Wuetz, M. P. Losert, S. Koelling, L. E. A. Stehouwer, A.-M. J. Zwerver, S. G. J. Philips, M. T. Mądzik, X. Xue, G. Zheng, M. Lodari, S. V. Amitonov, N. Samkharadze, A. Sammak, L. M. K. Vandersypen, R. Rahman, S. N. Coppersmith, O. Moutanabbir, M. Friesen, and G. Scappucci. “Atomic fluctuations lifting the energy degeneracy in Si/SiGe quantum dots”. In: *Nature Communications* 13.1 (Dec. 2022). doi: 10.1038/s41467-022-35458-0.

[14] M. Volmer, T. Struck, A. Sala, B. Chen, M. Oberländer, T. Offermann, R. Xue, L. Visser, J.-S. Tu, S. Trellenkamp, Ł. Cywiński, H. Bluhm, and L. R. Schreiber. “Mapping of valley splitting by conveyor-mode spin-coherent electron shuttling”. In: *npj Quantum Information* 10.1 (June 2024). doi: 10.1038/s41534-024-00852-7.

[15] G. Dresselhaus. “Spin-Orbit Coupling Effects in Zinc Blende Structures”. In: *Physical Review* 100.2 (Oct. 1955), pp. 580–586. doi: 10.1103/physrev.100.580.

[16] G. Bihlmayer, O. Rader, and R. Winkler. “Focus on the Rashba effect”. In: *New Journal of Physics* 17.5 (May 2015), p. 050202. doi: 10.1088/1367-2630/17/5/050202.

[17] M. Prada, G. Klimeck, and R. Joynt. “Spin–orbit splittings in Si/SiGe quantum wells: from ideal Si membranes to realistic heterostructures”. In: *New Journal of Physics* 13.1 (Jan. 2011), p. 013009. doi: 10.1088/1367-2630/13/1/013009.

[18] R. Maurand, X. Jehl, D. Kotekar-Patil, A. Corna, H. Bohuslavskyi, R. Laviéville, L. Hutin, S. Barraud, M. Vinet, M. Sanquer, and S. De Franceschi. “A CMOS silicon spin qubit”. In: *Nature Communications* 7.1 (Nov. 2016). doi: 10.1038/ncomms13575.

[19] A. M. J. Zwerver, T. Krähenmann, T. F. Watson, L. Lampert, H. C. George, R. Pillarisetty, S. A. Bojarski, P. Amin, S. V. Amitonov, J. M. Boter, R. Caudillo, D. Correas-Serrano, J. P. Dehollain, G. Droulers, E. M. Henry, R. Kotlyar, M. Lodari, F. Lüthi, D. J. Michalak, B. K. Mueller, S. Neyens, J. Roberts, N. Samkharadze, G. Zheng, O. K. Zietz, G. Scappucci, M. Veldhorst, L. M. K. Vandersypen, and J. S. Clarke. "Qubits made by advanced semiconductor manufacturing". In: *Nature Electronics* 5.3 (Mar. 2022), pp. 184–190. doi: 10.1038/s41928-022-00727-9.

[20] S. Neyens, O. K. Zietz, T. F. Watson, F. Luthi, A. Nethwewala, H. C. George, E. Henry, M. Islam, A. J. Wagner, F. Borjans, E. J. Connors, J. Corrigan, M. J. Curry, D. Keith, R. Kotlyar, L. F. Lampert, M. T. Mądzik, K. Millard, F. A. Mohiyaddin, S. Pellerano, R. Pillarisetty, M. Ramsey, R. Savytskyy, S. Schaal, G. Zheng, J. Ziegler, N. C. Bishop, S. Bojarski, J. Roberts, and J. S. Clarke. "Probing single electrons across 300-mm spin qubit wafers". In: *Nature* 629.8010 (May 2024), pp. 80–85. doi: 10.1038/s41586-024-07275-6.

[21] P. Steinacker, N. D. Stuyck, W. H. Lim, T. Tanttu, M. Feng, A. Nickl, S. Serrano, M. Candido, J. D. Cifuentes, F. E. Hudson, K. W. Chan, S. Kubicek, J. Jussot, Y. Canvel, S. Beyne, Y. Shimura, R. Loo, C. Godfrin, B. Raes, S. Baudot, D. Wan, A. Laucht, C. H. Yang, A. Saraiva, C. C. Escott, K. D. Greve, and A. S. Dzurak. *A 300 mm foundry silicon spin qubit unit cell exceeding 99% fidelity in all operations*. 2024.

[22] T. Huckemann, P. Muster, W. Langheinrich, V. Brackmann, M. Friedrich, N. D. Komerički, L. K. Diebel, V. Stieß, D. Bougeard, C. Dahl, L. R. Schreiber, and H. Bluhm. *Industrially fabricated single-electron quantum dots in Si/Si-Ge heterostructures*. 2024.

[23] L. M. K. Vandersypen, H. Bluhm, J. S. Clarke, A. S. Dzurak, R. Ishihara, A. Morello, D. J. Reilly, L. R. Schreiber, and M. Veldhorst. "Interfacing spin qubits in quantum dots and donors—hot, dense, and coherent". In: *npj Quantum Information* 3.1 (Sept. 2017). doi: 10.1038/s41534-017-0038-y.

[24] Y. Xu, F. K. Unseld, A. Corna, A. M. J. Zwerver, A. Sammak, D. Brousse, N. Samkharadze, S. V. Amitonov, M. Veldhorst, G. Scappucci, R. Ishihara, and L. M. K. Vandersypen. "On-chip integration of Si/SiGe-based quantum dots and switched-capacitor circuits". In: *Applied Physics Letters* 117.14 (Oct. 2020). doi: 10.1063/5.0012883.

[25] J. van Dijk, E. Kawakami, R. Schouten, M. Veldhorst, L. Vandersypen, M. Babaie, E. Charbon, and F. Sebastiano. "Impact of Classical Control Electronics on Qubit Fidelity". In: *Physical Review Applied* 12.4 (Oct. 2019). doi: 10.1103/physrevapplied.12.044054.

[26] M. A. Wolfe, T. McJunkin, D. R. Ward, D. Campbell, M. Friesen, and M. A. Eriksson. *On-chip cryogenic multiplexing of Si/SiGe quantum devices*. 2024. doi: 10.48550/ARXIV.2410.13721.

[27] J. Dijkema, X. Xue, P. Harvey-Collard, M. Rimbach-Russ, S. L. de Snoo, G. Zheng, A. Sammak, G. Scappucci, and L. M. K. Vandersypen. "Cavity-mediated iSWAP oscillations between distant spins". In: *Nature Physics* (Dec. 2024). doi: 10.1038/s41567-024-02694-8.

[28] I. Seidler, T. Struck, R. Xue, N. Focke, S. Trellenkamp, H. Bluhm, and L. R. Schreiber. "Conveyor-mode single-electron shuttling in Si/SiGe for a scalable quantum computing architecture". In: *npj Quantum Information* 8.1 (Aug. 2022). doi: 10.1038/s41534-022-00615-2.

[29] A. R. Mills, D. M. Zajac, M. J. Gullans, F. J. Schupp, T. M. Hazard, and J. R. Petta. "Shuttling a single charge across a one-dimensional array of silicon quantum dots". In: *Nature Communications* 10.1 (Mar. 2019). doi: 10.1038/s41467-019-08970-z.

[30] A. Zwerver, S. Amitonov, S. de Snoo, M. Mądzik, M. Rimbach-Russ, A. Sammak, G. Scappucci, and L. Vandersypen. "Shuttling an Electron Spin through a Silicon Quantum Dot Array". In: *PRX Quantum* 4.3 (July 2023). doi: 10.1103/prxquantum.4.030303.

[31] M. De Smet, Y. Matsumoto, A.-M. J. Zwerver, L. Tryputen, S. L. de Snoo, S. V. Amitonov, A. Sammak, N. Samkharadze, Ö. Gül, R. N. M. Wasserman, M. Rimbach-Russ, G. Scappucci, and L. M. K. Vandersypen. *High-fidelity single-spin shuttling in silicon*. 2024. doi: 10.48550/ARXIV.2406.07267.

[32] T. Struck, M. Volmer, L. Visser, T. Offermann, R. Xue, J.-S. Tu, S. Trellenk, Ł. Cywiński, H. Bluhm, and L. R. Schreiber. "Spin-EPR-pair separation by conveyor-mode single electron shuttling in Si/SiGe". In: *Nature Communications* 15.1 (Feb. 2024). doi: 10.1038/s41467-024-45583-7.

[33] T. Hensgens, T. Fujita, L. Janssen, X. Li, C. J. Van Diepen, C. Reichl, W. Wegscheider, S. Das Sarma, and L. M. K. Vandersypen. "Quantum simulation of a Fermi–Hubbard model using a semiconductor quantum dot array". In: *Nature* 548.7665 (Aug. 2017), pp. 70–73. doi: 10.1038/nature23022.

[34] X. Wang, E. Khatami, F. Fei, J. Wyrick, P. Namboodiri, R. Kashid, A. F. Rigosi, G. Bryant, and R. Silver. "Experimental realization of an extended Fermi-Hubbard model using a 2D lattice of dopant-based quantum dots". In: *Nature Communications* 13.1 (Nov. 2022). doi: 10.1038/s41467-022-34220-w.

[35] C. Volk, A. M. J. Zwerver, U. Mukhopadhyay, P. T. Eendebak, C. J. van Diepen, J. P. Dehollain, T. Hensgens, T. Fujita, C. Reichl, W. Wegscheider, and L. M. K. Vandersypen. “Loading a quantum-dot based “Qubyte” register”. In: *npj Quantum Information* 5.1 (Apr. 2019). doi: 10.1038/s41534-019-0146-y.

[36] D. Keith, M. G. House, M. B. Donnelly, T. F. Watson, B. Weber, and M. Y. Simmons. “Single-Shot Spin Readout in Semiconductors Near the Shot-Noise Sensitivity Limit”. In: *Physical Review X* 9.4 (Oct. 2019). doi: 10.1103/physrevx.9.041003.

[37] G. A. Oakes, V. N. Ciriano-Tejel, D. F. Wise, M. A. Fogarty, T. Lundberg, C. Lainé, S. Schaal, F. Martins, D. J. Ibberson, L. Hutin, B. Bertrand, N. Stelmashenko, J. W. A. Robinson, L. Ibberson, A. Hashim, I. Siddiqi, A. Lee, M. Vinet, C. G. Smith, J. J. L. Morton, and M. F. Gonzalez-Zalba. “Fast High-Fidelity Single-Shot Readout of Spins in Silicon Using a Single-Electron Box”. In: *Physical Review X* 13.1 (Feb. 2023). doi: 10.1103/physrevx.13.011023.

[38] L. Cochrane, A. A. Seshia, and M. F. Gonzalez-Zalba. “Intrinsic noise of the single-electron box”. In: *Physical Review Applied* 21.6 (June 2024). doi: 10.1103/physrevapplied.21.064066.

[39] D. Buterakos and S. Das Sarma. “Spin-Valley Qubit Dynamics in Exchange-Coupled Silicon Quantum Dots”. In: *PRX Quantum* 2.4 (Dec. 2021). doi: 10.1103/prxquantum.2.040358.

[40] C. H. Yang, A. Rossi, R. Ruskov, N. S. Lai, F. A. Mohiyaddin, S. Lee, C. Tahan, G. Klimeck, A. Morello, and A. S. Dzurak. “Spin-valley lifetimes in a silicon quantum dot with tunable valley splitting”. In: *Nature Communications* 4.1 (June 2013). doi: 10.1038/ncomms3069.

[41] E. Kawakami, P. Scarlino, D. R. Ward, F. R. Braakman, D. E. Savage, M. G. Lagally, M. Friesen, S. N. Coppersmith, M. A. Eriksson, and L. M. K. Vandersypen. “Electrical control of a long-lived spin qubit in a Si/SiGe quantum dot”. In: *Nature Nanotechnology* 9.9 (Aug. 2014), pp. 666–670. doi: 10.1038/nnano.2014.153.

[42] M. L. V. Tagliaferri, P. L. Bavdaz, W. Huang, A. S. Dzurak, D. Culcer, and M. Veldhorst. “Impact of valley phase and splitting on readout of silicon spin qubits”. In: *Physical Review B* 97.24 (June 2018). doi: 10.1103/physrevb.97.245412.

[43] J. M. Elzerman, R. Hanson, L. H. Willems van Beveren, B. Witkamp, L. M. K. Vandersypen, and L. P. Kouwenhoven. “Single-shot readout of an individual electron spin in a quantum dot”. In: *Nature* 430.6998 (July 2004), pp. 431–435. doi: 10.1038/nature02693.

[44] N. S. Lai, W. H. Lim, C. H. Yang, F. A. Zwanenburg, W. A. Coish, F. Qassemi, A. Morello, and A. S. Dzurak. “Pauli Spin Blockade in a Highly Tunable Silicon Double Quantum Dot”. In: *Scientific Reports* 1.1 (Oct. 2011). doi: 10.1038/srep00110.

[45] A. E. Seedhouse, T. Tanttu, R. C. Leon, R. Zhao, K. Y. Tan, B. Hensen, F. E. Hudson, K. M. Itoh, J. Yoneda, C. H. Yang, A. Morello, A. Laucht, S. N. Coppersmith, A. Saraiva, and A. S. Dzurak. “Pauli Blockade in Silicon Quantum Dots with Spin-Orbit Control”. In: *PRX Quantum* 2.1 (Jan. 2021). doi: 10.1103/prxquantum.2.010303.

[46] A. Mills, C. Guinn, M. Feldman, A. Sigillito, M. Gullans, M. Rakher, J. Kerckhoff, C. Jackson, and J. Petta. “High-Fidelity State Preparation, Quantum Control, and Readout of an Isotopically Enriched Silicon Spin Qubit”. In: *Physical Review Applied* 18.6 (Dec. 2022). doi: 10.1103/physrevapplied.18.064028.

[47] S. G. J. Philips, M. T. Mądzik, S. V. Amitonov, S. L. de Snoo, M. Russ, N. Kalhor, C. Volk, W. I. L. Lawrie, D. Brousse, L. Tryputen, B. P. Wuetz, A. Sammak, M. Veldhorst, G. Scappucci, and L. M. K. Vandersypen. “Universal control of a six-qubit quantum processor in silicon”. In: *Nature* 609.7929 (Sept. 2022), pp. 919–924. doi: 10.1038/s41586-022-05117-x.

[48] L. Childress, A. S. Sørensen, and M. D. Lukin. “Mesoscopic cavity quantum electrodynamics with quantum dots”. In: *Physical Review A* 69.4 (Apr. 2004). doi: 10.1103/physreva.69.042302.

[49] J. I. Colless, A. C. Mahoney, J. M. Hornibrook, A. C. Doherty, H. Lu, A. C. Gossard, and D. J. Reilly. “Dispersive Readout of a Few-Electron Double Quantum Dot with Fast rf Gate Sensors”. In: *Physical Review Letters* 110.4 (Jan. 2013). doi: 10.1103/physrevlett.110.046805.

[50] A. West, B. Hensen, A. Jouan, T. Tanttu, C.-H. Yang, A. Rossi, M. F. Gonzalez-Zalba, F. Hudson, A. Morello, D. J. Reilly, and A. S. Dzurak. “Gate-based single-shot readout of spins in silicon”. In: *Nature Nanotechnology* 14.5 (Mar. 2019), pp. 437–441. doi: 10.1038/s41565-019-0400-7.

[51] F. H. L. Koppens, C. Buizert, K. J. Tielrooij, I. T. Vink, K. C. Nowack, T. Meunier, L. P. Kouwenhoven, and L. M. K. Vandersypen. “Driven coherent oscillations of a single electron spin in a quantum dot”. In: *Nature* 442.7104 (Aug. 2006), pp. 766–771. doi: 10.1038/nature05065.

[52] J. Yoneda, T. Otsuka, T. Takakura, M. Pioro-Ladrière, R. Brunner, H. Lu, T. Nakajima, T. Obata, A. Noiri, C. J. Palmstrøm, A. C. Gossard, and S. Tarucha. “Robust micromagnet design for fast electrical manipulations of single spins in quantum dots”. In: *Applied Physics*

*Express* 8.8 (July 2015), p. 084401. doi: 10.7567/apex.8.084401.

[53] C.-A. Wang, V. John, H. Tidjani, C. X. Yu, A. S. Ivlev, C. Déprez, F. van Riggelen-Doelman, B. D. Woods, N. W. Hendrickx, W. I. L. Lawrie, L. E. A. Stehouwer, S. D. Oosterhout, A. Sammak, M. Friesen, G. Scappucci, S. L. de Snoo, M. Rimbach-Russ, F. Borsoi, and M. Veldhorst. "Operating semiconductor quantum processors with hopping spins". In: *Science* 385.6707 (July 2024), pp. 447–452. doi: 10.1126/science.ado5915.

[54] M. A. Nielsen. "A simple formula for the average gate fidelity of a quantum dynamical operation". In: *Physics Letters A* 303.4 (Oct. 2002), pp. 249–252. doi: 10.1016/s0375-9601(02)01272-0.

[55] J. Emerson, R. Alicki, and K. Życzkowski. "Scalable noise estimation with random unitary operators". In: *Journal of Optics B: Quantum and Semiclassical Optics* 7.10 (Sept. 2005), S347–S352. doi: 10.1088/1464-4266/7/10/021.

[56] E. Knill, D. Leibfried, R. Reichle, J. Britton, R. B. Blakestad, J. D. Jost, C. Langer, R. Ozeri, S. Seidelin, and D. J. Wineland. "Randomized benchmarking of quantum gates". In: *Physical Review A* 77.1 (Jan. 2008). doi: 10.1103/physreva.77.012307.

[57] A. Hollmann, T. Struck, V. Langrock, A. Schmidbauer, F. Schauer, T. Leonhardt, K. Sawano, H. Riemann, N. V. Abrosimov, D. Bougeard, and L. R. Schreiber. "Large, Tunable Valley Splitting and Single-Spin Relaxation Mechanisms in a Si/SiGe Quantum Dot". In: *Physical Review Applied* 13.3 (Mar. 2020). doi: 10.1103/physrevapplied.13.034068.

[58] P. Huang and X. Hu. "Spin relaxation in a Si quantum dot due to spin-valley mixing". In: *Physical Review B* 90.23 (Dec. 2014). doi: 10.1103/physrevb.90.235315.

[59] A. Hosseinkhani and G. Burkard. "Theory of silicon spin qubit relaxation in a synthetic spin-orbit field". In: *Physical Review B* 106.7 (Aug. 2022). doi: 10.1103/physrevb.106.075415.

[60] F. Borjans, D. Zajac, T. Hazard, and J. Petta. "Single-Spin Relaxation in a Synthetic Spin-Orbit Field". In: *Physical Review Applied* 11.4 (Apr. 2019). doi: 10.1103/physrevapplied.11.044063.

[61] H. Y. Carr and E. M. Purcell. "Effects of Diffusion on Free Precession in Nuclear Magnetic Resonance Experiments". In: *Physical Review* 94.3 (May 1954), pp. 630–638. doi: 10.1103/physrev.94.630.

[62] S. Meiboom and D. Gill. "Modified Spin-Echo Method for Measuring Nuclear Relaxation Times". In: *Review of Scientific Instruments* 29.8 (Aug. 1958), pp. 688–691. doi: 10.1063/1.1716296.

[63] L. Cvitkovich, P. Stano, C. Wilhelmer, D. Waldhör, D. Loss, Y.-M. Niquet, and T. Grasser. *Coherence limit due to hyperfine interaction with nuclei in the barrier material of Si spin qubits*. 2024. doi: 10.48550/ARXIV.2405.10667.

[64] A. Kha, R. Joynt, and D. Culcer. "Do micromagnets expose spin qubits to charge and Johnson noise?" In: *Applied Physics Letters* 107.17 (Oct. 2015). doi: 10.1063/1.4934693.

[65] K. W. Chan, W. Huang, C. H. Yang, J. C. C. Hwang, B. Hensen, T. Tanttu, F. E. Hudson, K. M. Itoh, A. Laucht, A. Morello, and A. S. Dzurak. "Assessment of a Silicon Quantum Dot Spin Qubit Environment via Noise Spectroscopy". In: *Physical Review Applied* 10.4 (Oct. 2018). doi: 10.1103/physrevapplied.10.044017.

[66] E. J. Connors, J. Nelson, L. F. Edge, and J. M. Nichol. "Charge-noise spectroscopy of Si/SiGe quantum dots via dynamically-decoupled exchange oscillations". In: *Nature Communications* 13.1 (Feb. 2022). doi: 10.1038/s41467-022-28519-x.

# 3

# EXPERIMENTAL METHODS

*Machines take me by surprise with great frequency.*

Alan Turing

Moving from theoretical concepts to practical implementation introduces a range of new challenges. This chapter addresses three key aspects encountered during this research work. Operating spin qubits in cryogenic conditions requires meticulous design of the wiring to minimize noise and heat dissipation while ensuring robust signal integrity. Extending this consideration, the design of the printed circuit board (PCB) plays a critical role as the interface linking the control electronics, the cryogenic environment, and the spin qubit chip. Lastly, while there is a growing trend toward industrially fabricated quantum dot devices, the work presented here was conducted on samples produced in an academic clean room, making the fabrication processes the third focus of this chapter.



## 3.1. SETTING UP A CRYOSTAT

Dilution cryostats have become a standard tool in this line of research and are commercially available from various companies. Hence this chapter will not focus on their inner workings, (see [1, 2]), but instead provide guidance on how to design its wiring. For this purpose the wiring is divided into two categories: wires for direct current (DC) to medium frequency (MF) signals that are used to bias gates and create a potential landscape which isolates single spins (DC-wiring) and coaxial cables for high frequency (HF) to super high frequency (SHF) signals that modulate the potential landscape temporarily e.g. to operate a spin qubit (RF-wiring)[3].

### DIRECT CURRENT WIRING

Specifying the DC-wiring is relatively straight forward as commercial looms can be used with few considerations. A trade-off between wire count and static heat load has to be found as each wire provides a thermal connection between different temperature stages. By using wires made from materials such as phosphor bronze (PhBr), the static heat load can be reduced significantly. At 4 K PhBr has a thermal conductance of $1.6\,\mathrm{W\,m^{-1}\,K^{-1}}$, contrasting copper which has $300\,\mathrm{W\,m^{-1}\,K^{-1}}$. The reduced thermal conductivity comes at a price though, the resistance of PhBr wires is over two orders of magnitudes higher than copper wires [4].

When (slowly) sweeping voltages on field effect gates this is negligible, however, driving a current through PhBr wires quickly dissipates a significant amount of power. For 50 cm of wire at 4 K and a current of 1 mA the wire alone dissipates $P = I^2 \times R_{\mathrm{PhBr}}(T) \times l \approx 1.6\,\mu\mathrm{W}$. While this amount of dissipated power affects the 4K-stage very little, a similar amount will also be dissipated on other temperature stages e.g. the MXC-stage. There it is a significant fraction of the available cooling

power, typically 10 µW to 100 µW at base temperature.

A second consideration is the filtering of the DC-wiring. Ultimately this impacts the noise on gates and the speed in which measurements using the DC-wiring can be done. Set ups in this lab typically use two types of low pass filters: a second-order resistor–capacitor (RC) low-pass (LP) with discrete elements and a copper powder filter. The discrete RC filters can be well adjusted to the needs of a set up and experiment. A distinction between filtering for gates and ohmic contacts (e.g. for SETs, see Section 2.2.2) should be considered as the additional resistances of the RC filters will limit the measurable current[1]. Typical cut-off frequency are 10 Hz to 50 Hz for gates and 0.5 MHz to 5 MHz for ohmic contacts.



Metal powder filters on the other hand are less flexible in their filtering characteristics. The large surface area of metal powder dampens RF signals due to the skin effect [5]. With the skin effect being proportional to the frequency metal powder filters are used as LP filters. The cut-off frequency is approximated by the frequency at which the penetration depth equals the powder size. Non-uniformity of particle size and spurious resonances due to manufacturing processes can make a clear definition challenging [6, 7]. Common powder materials are copper, brass and steel with nominal grain sizes ranging between 1 µm and 100 µm [6–9].

#### RADIO-FREQUENCY WIRING

Designing the RF-wiring has more free parameters. As before a variety of materials can be used which impact transmission properties or static heat loads. However, more impactful are the discrete attenuators that can be installed on every temperature stage. These attenuators are required to thermalize noise and inhibit the formation of standing waves due to impedance mismatches. Both effects benefit from a larger attenuation, however, there are two arguments against using a large attenuation, e.g. 20 dB, on every stage. First attenuators not only reduce noise and standing waves but also the signals. Increasing the signal strength to compensate is not always possible or desired. Secondly the attenuation is dissipative, a larger attenuator as well as a larger signal dissipate more power, creating additional heat loads.

To plan the number and distribution of the attenuators in a line it is best to first estimate the maximally possible attenuation. This can be based on the signal power/amplitude that is required on the chip and the maximum output power of the used signal generators. With the maximally possible attenuation fixed, the attenuation is then distributed to optimize power dissipation/heat load and photon temperature.

For voltages

$$V_{\text{out}} = 10^{\frac{\alpha+\beta}{20}} V_{\text{in}}, \tag{3.1}$$

[1] Some ohmic contacts use only a first-order low-pass filter.

where $\alpha$ denotes the total attenuation of the discrete attenuators in dB and $\beta$ cable losses in dB[2]. Cable attenuation depends heavily on the used materials and thicknesses as well as the frequency range and temperature. For silver plated copper nickel cables (SCuNi-CuNi) with 0.86mm diameter range the attenuation ranges between 1.5 dB m$^{-1}$ at 4 K and 1 GHz to 9.5 dB m$^{-1}$ at 300 K and 10 GHz [10].

Solving Equation 3.1 for $\alpha$, assuming a $V_{\text{out,peak}} = 150\,\text{mV}$ voltage swing on the sample is required using a $V_{\text{in,peak}} = 2\,\text{V}$ source with a total cable attenuation of $\beta = 6\,\text{dB}$ the discrete attenuators should not exceed

$$\alpha = \left| 20 \log_{10} \left( \frac{0.15\ \text{V}}{2\ \text{V}} \right) \right| - 6\ \text{dB} \approx 16.50\,\text{dB}. \tag{3.2}$$

In an example to emphasize the effect of attenuator placement, a single attenuator is positioned at the very beginning of the system, prior to any cable losses. It will dissipate

$$P_{\text{diss}} = P_{\text{in}} - P_{\text{out}}, \tag{3.3}$$

with

$$P_{\text{in}} = P_{\text{Signal}} = \frac{V_{\text{in,RMS}}^2}{Z_0}. \tag{3.4}$$

Assuming $Z_0 = 50\,\Omega$ and a sinusoidal waveform gives $V_{\text{in,RMS}} = \frac{1}{\sqrt{2}} V_{\text{in,peak}}$ and thus $P_{in} = 40\,\text{mW}$ or $P_{in,dBm} = 16.02\,\text{dBm}$. Using then

$$P_{out,dBm} = P_{in,dBm} - \alpha \tag{3.5}$$

$$= 16.02\,\text{dBm} - 16.5\,\text{dB} = -0.48\,\text{dBm} \tag{3.6}$$

which gives $P_{\text{out}} \approx 0.90\,\text{mW}$ in Equation 3.3 we find $P_{diss} = 40\,\text{mW} - 0.90\,\text{mW} = 39.10\,\text{mW}$.

On the other hand using a single attenuator on the last stage, after the cable attenuation, changes Equation 3.4 to

$$P'_{\text{in,dBm}} = P_{\text{Signal,dBm}} - \beta \tag{3.7}$$

$$= 16.02\,\text{dBm} - 6\,\text{dB} = 10.02\,\text{dBm} \tag{3.8}$$

as the cables attenuate the signal before it reaches the discrete attenuator. Following Equation 3.5 and Equation 3.3 we find $P'_{out} \approx 0.22\,\text{mW}$ and $P'_{diss} = 9.78\,\text{mW}$. These two example calculations show how the distribution of attenuators impacts the heat load on different stages.

Looking only at power dissipation it makes most sense to put most or all attenuation on the 50K-stage or 4K-stage as they have more than

[2] The correction factor for driving a line with an open end is not included in this calculation.

sufficient cooling power. Contrary to this it is desired to maximise the attenuation on the lower stages to thermalize noise which not only originates from the signal source but is also introduced along the entire transmission line. However using a 1 dB attenuator on the MXC-plate and running the above outlined calculation again

$$P_{\text{in,dBm}} = 16.02\,\text{dBm} - 6\,\text{dB} - 15.50\,\text{dB} = -5.48\,\text{dBm} \tag{3.9}$$

$$P_{\text{out,dBm}} = 16.02\,\text{dBm} - 6\,\text{dB} - 15.50\,\text{dB} - 1\,\text{dB} = -6.48\,\text{dBm}, \tag{3.10}$$

yields $P_{diss} \approx 60\,\mu\text{W}$ which exceeds the cooling power of most fridges at base temperature. Hence, with parameters similar to this example attenuation on the MXC-stage should be avoided.

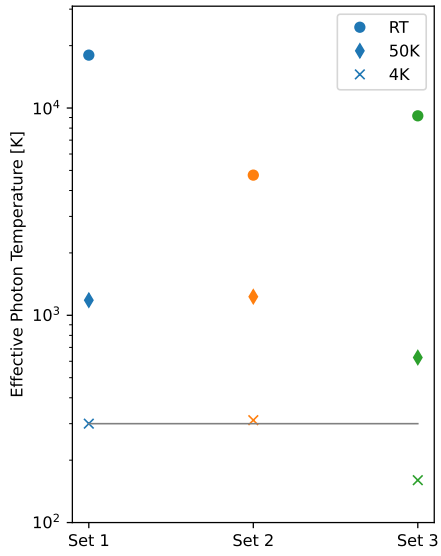


**Figure 3.1: Effect of attenuation on photon noise temperature.** Photon temperatures at 1 MHz for three sets of attenuation at the stages [Room temperature, 50K Plate, 4K Plate]: Set 1 = [0 dB,12 dB,6 dB], Set 2 = [6 dB,6 dB,6 dB], Set 3 = [3 dB,12 dB,6 dB] using a starting temperature of 18 000 K

Even with this constraint, noise temperature and its spectral distribution can be optimized. Most relevant for this consideration is Johnson-Nyquist noise, the noise generated by the natural motion of charge carriers in an electrical conductor. Its power spectral density for a coaxial line with characteristic impedance $Z$ can be described by

$$S(T,f) = 2Zhf \frac{1}{e^{\frac{hf}{k_b T}} - 1}, \tag{3.11}$$

where the second factor is the photon occupation number given by a Bose-Einstein distribution [11, 12]

$$n_{BE}(T,f) = \frac{1}{e^{\frac{hf}{k_b T}} - 1}. \tag{3.12}$$

Here $T$ denotes the temperature, $f$ the frequency while $h$ and $k_B$ denote the Planck and Boltzmann constants respectively.

The coaxial cables propagate the Johnson-Nyquist noise generated at room temperature into the fridge where attenuators dissipate a fraction of this noise while adding new noise at their respective temperature. A 20 dB

attenuator reduces the incoming noise power by a factor of $A = 10^{-\frac{20\,\mathrm{dB}}{10}}$ to 1 % and adds 99 % blackbody radiation with the temperature of the attenuator. The new photon occupation distribution becomes

$$n_{\mathrm{new}}(f) = A n_{\mathrm{old}}(f) + (1-A) n_{BE}(T_{\mathrm{Att}}, f). \tag{3.13}$$

Equations 3.12 and 3.13 allow to calculate and propagate the photon occupation distribution from room temperature through all attenuators down to the sample. Using this we can not only estimate the number of photons at a certain frequency but also calculate the effective photon temperature as function of frequency $T(f) = \frac{hf}{k_B \ln\left(\frac{n+1}{n}\right)}$.

While this is a good approximation it is important to note two things. First these calculations ignore the distributed attenuation of the coaxial cables $A_{\mathrm{coax}}$ that is a function of temperature and frequency. Secondly the noise generated by active electronics is not equivalent to the noise of a cable at room temperature. Data sheets of e.g. arbitrary waveform generators (AWGs) specify voltage noise densities $V_n$ in $\mathrm{V}/\sqrt{\mathrm{Hz}}$ or $\mathrm{dBm}/\sqrt{\mathrm{Hz}}$. This can be converted per unit of bandwidth to an effective temperature using

$$T_{\mathrm{eff}} = \frac{V_n^2}{4 k_B Z}. \tag{3.14}$$

The QBlox Qubit Control Module AWG specifies $V_n < 7\,\mathrm{nV}/\sqrt{\mathrm{Hz}}$ at 1 MHz thus $T_{\mathrm{eff}} \lessapprox 18\,000\,\mathrm{K}$ [13]. Therefore including an attenuator at room temperature will also improve the noise properties. Fig. 3.1 shows the noise temperatures of three sets of attenuation, one without attenuation at room temperature, the second and third with. Both Set 1 and Set 2 have a photon temperature of above 300 K at the 4K-stage while the difference between them is below 5 %. The additional 3 dB of Set 3, compared to Set 1 and Set 2, improve the photon temperature significantly. While Set 1 does outperform Set 2 the flexibility to change attenuators without having to open the fridge is an underrated benefit.

Ultimately when choosing the attenuation scheme for the RF lines in a fridge a delicate balance has to be found. Each line can be maximally optimised with the attenuators as cold as possible and values picked for each individual cable depending on intended signals. But this approach offers little flexibility and with projects regularly changing is short sighted. A possible compromise in the context of spin-qubits is to specify three sets of RF lines with increasing attenuation. One set each for barrier and quantum dot plunger gates and one for miscellaneous gates such as SET plungers or driving gates. All thee sets should have between 3 dB and 6 dB less attenuation than a calculation following Equation 3.2 allows. This underestimation enables different projects to customise and optimise with additional attenuation at room temperature. Due to this

underestimation none of three sets should have any attenuation on the MXC-plate. The Still plate offers a better alternative, as the dissipated power can be compensated by dissipating less power in the still heater.

## 3.2. DESIGN OF A PRINTED CIRCUIT BOARD

In the signal chain from the room temperature (RT) electronics to the spin qubit sample, the PCB plays a crucial role. Primarily, it hosts the sample and serves as the interface between the fridge wiring and the sample. The latter is typically connected to the PCB via aluminium (Al) bond wires. Additionally, the PCB integrates bias tees that combine RF and DC signals, along with various RC-filters. Lastly, it provides space for tank circuits used for RF-SET-based charge sensing.

As samples change so will their requirements for connections and thus for the PCBs that are hosting them. Every so often the requirements change enough that using existing PCB designs becomes infeasible and new ones are required. The design of a new PCB can be broken down into three parts. Formulating the requirements, designing the schematic and transferring the schematic into a board.

For the PCB “21-021 Sample Board” the requirements were based on the idea of scaling quantum dot arrays in the second dimension with the following consequences: first with more quantum dots more RF lines were required. Secondly their distribution around the chip needed to be more even, contrasting prior PCBs where one chip side had access to a majority of RF lines. Lastly the new PCB should be compatible with current infrastructure where possible.

Complying with the last point meant that the new PCB would rely on two 50 line flat flexible cables (FFC) for DC signals. Each FFC connector is shorted to a second connector allowing to fully ground/short the chip before disconnecting the PCB from the fridge. Additional solder pads for 0 Ω resistors were added to accommodate inconsistencies in grounding schemes of different fridges.

For RF connectivity prior PCBs relied on SMP connectors. However, the idea to plainly add more was discarded for two reasons, their low density (>24 $mm^2$/channel) and high mating effort. Instead the Ardent TR40 connector was chosen as new RF-connector. Unlike SMP connectors the Ardent connector pushes spring loaded pins onto pads on the PCB. Each connector has 16 or 24 RF lines with a footprint of 252 $mm^2$ (15.8 $mm^2$/channel) and 353.5 $mm^2$ (14.7 $mm^2$/channel) respectively. The TR40 connector thus increases channel density while reducing complexity and components on the PCB. Two TR40 connectors, each providing 24 channels, were selected to sufficiently improve the availability of RF lines over earlier PCBs in the group. Separated from this a dedicated SMP connector was kept for the RF-readout chain.

Two additional design improvements were incorporated. First, a

central cut-out was introduced in the PCB to allow the sample to be mounted directly onto a copper backplate instead of the PCB epoxy. This modification is expected to improve the thermalisation of the sample. This placement also reduces distance between the sample surface and the PCB, which shortens bond wire lengths, thereby enhancing RF signal integrity by reducing parasitic inductances [14]. Second, a copper shield was added to safeguard the sample and bond wires from mechanical interference, such as accidental contact. At this stage cavity modes of the shield were not addressed, but this can easily be avoided by making the shield from plastic.

Building on these design considerations, the next step is the creation of a schematic, which serves as a comprehensive blueprint for the PCB. The schematic defines all electrical connections between components, represented either as wires or through standardized labels and symbols. Furthermore, each component is annotated with metadata that specifies its physical attributes, including dimensions, shape, and the placement of solder or bond pads. While libraries of pre-designed schematics are available for most commercial off-the-shelf components, the symbols representing the sample space are custom made. Fig. 3.2 shows the sample space on the “21-021 Sample Board”.

Once the schematic is finalized, modifications to the number of components or their connectivity should be avoided as those will often reset any progress. Passive components, such as resistors and capacitors, are a partial exception to this rule. While these components are typically assigned specific values during the design process, their values can often be adjusted later without affecting their physical footprint.

Once the schematic is complete the physical PCB is designed. The signals are routed e.g. through various layers according to the schematic. Depending on their purpose these traces are then fine-tuned by e.g. impedance matching. Strategic placement of vias ensures proper connections between layers while minimizing parasitic effects and improving shielding of RF signals. The final layout of “21-021 Sample Board” v.1 is shown in Fig. 3.3**b** with Fig. 3.3**a** showing only the top layer.

Tests revealed several problems with the first version of this PCB. A floating ground plane between layers increased crosstalk between high frequency lines. Stacked vias caused connectivity issues and were susceptible to failure when exposed to stress. Subsequent versions of this PCB aimed to address these shortcomings. Due to delays in the design and manufacturing process the experiments in Chapter 4 and Chapter 5 did not make use of this PCB.

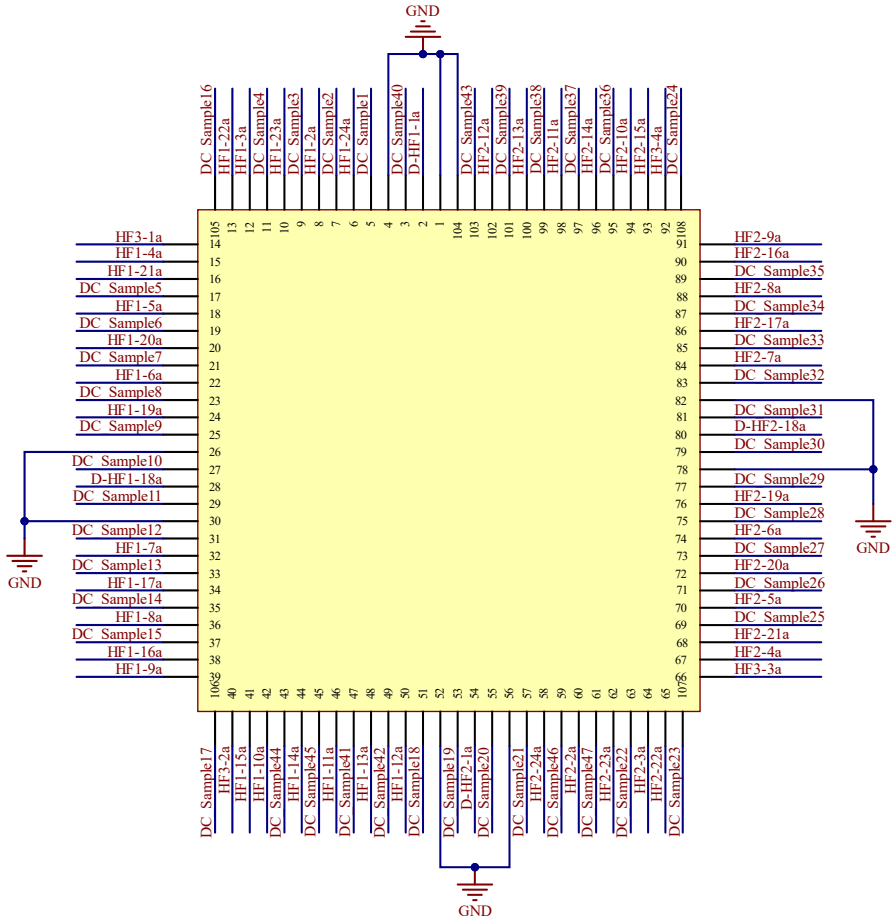


**Figure 3.2: Schematic of the sample space of the “21-021 Sample Board” v.1.** The schematic of the sample space shows all lines that will become bond pads. DC and RF lines are evenly distributed around the sample space, i.e. all four sides of the sample have 12 bond pads connected to lines including RF signals. This eases the on-chip fanout for larger 2D arrays. Additional grounded bond pads (GND) are included on each side to enable coplanar waveguides on the sample.

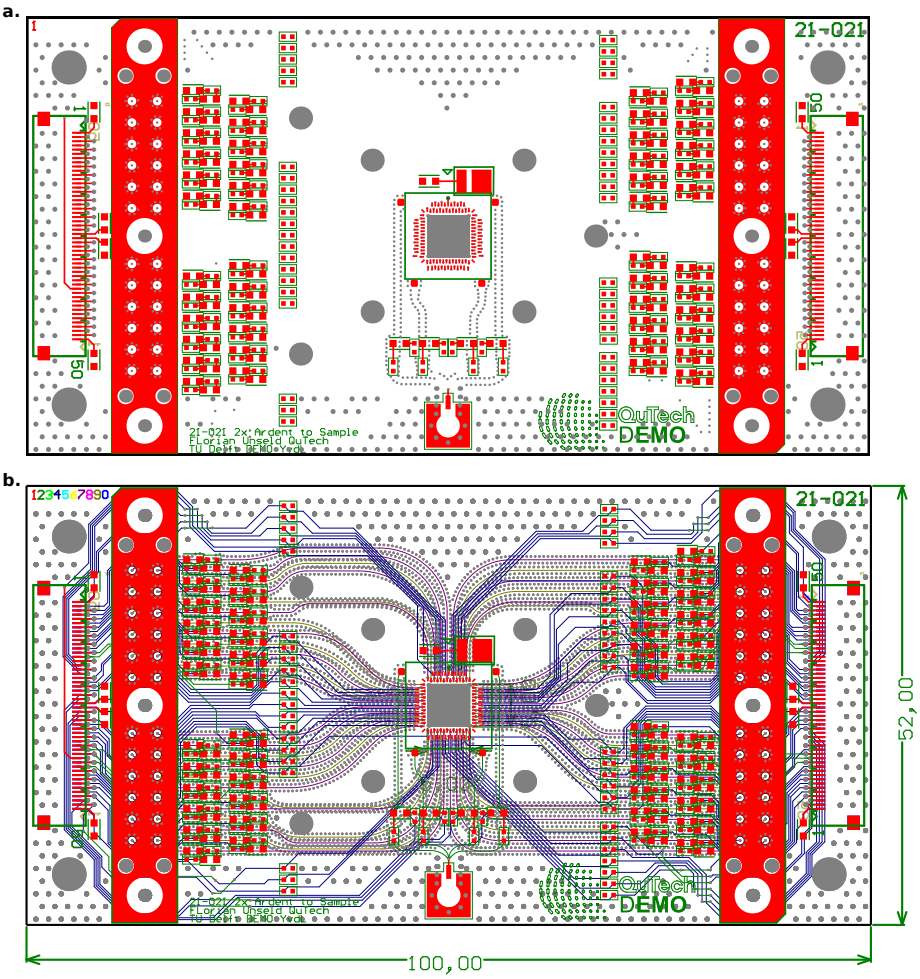


**Figure 3.3: Layout of the “21-021 Sample Board” v.1. a.** Top layer of the “21-021 Sample Board” v.1 showing in red the solder pads for e.g. FFC connectors, bond pads for the sample and the mating area of the two TR40 connectors. Holes and cut outs to mount the back plate and shield as well as vias are marked in light gray . The green lines indicate miscellaneous markings. **b.** Full Layout of the “21-021 Sample Board” v.1 with the colour representing the layer as indicated by the numbers in the top left corner of the PCB.

## 3.3. SAMPLE FABRICATION

Sample fabrication for the samples presented in this work is categorised into two major stages, “Prefab” and “Postfab”. Prefab includes the growth of the heterostructure, implantation of dopants, formation of ohmic contacts and fabrication of test structures. Detailed discussions of these steps are beyond the scope of this dissertation and can be found in [15].

Postfab refers to the fabrication of the gate stack ultimately defining the quantum dots. As common practice in academic nano fabrication, the gate stack is fabricated using electron beam lithography (EBL) and a lift-off procedure. A wide variety of materials are in principle suited as gate metal, though, all popular choices have some disadvantages. Table 3.1 gives a qualitative overview of common materials and key criteria. The titanium (Ti)/palladium (Pd) stack is notable for its small grain size and relatively good conductivity, making it suitable for producing fine gate structures [16]. However, Pd as a noble metal does not form a stable native oxide, therefore additional oxide layers are needed to separate different metal layers of the gate stack. The additional thickness reduces the lever arms of higher layers and also introduces additional defects [17].

Al addresses this issue as it forms a stable native oxide. Additionally, at low magnetic fields, Al becomes superconducting, eliminating electrical resistance as a concern at low enough fields and currents. However, it comes with some drawbacks, including a larger mismatch in thermal expansion coefficients and a larger grain size. The thermal expansion mismatch compared to the silicon substrate can introduce additional strain, leading to a disorder potential that may result in the formation of unintended quantum dots [18, 19]. The larger grain size makes the fabrication of finer gates challenging. Techniques such as the deposition of Al onto a cooled sample can, however, mitigate this [20].

The high kinetic inductance of niobium (Nb) based superconducting compounds such as NbTi or NbTi-Nitride makes them particularly suitable when involving resonators. Like Ti/Pd the lack of native oxides requires additional oxide layers to separate multiple gate stack layers. Unlike Al and Ti/Pd the gates are typically produced by etching.

In contrast to these approaches, poly Si gates - more commonly used in industrial fabrication than in university clean rooms - offer distinct advantages. Its grain size is small and thermal expansion is close to SiGe [16]. Decades of research also managed to produce some of the best interfaces between oxides, gates and heterostructure [21]. Two notable downsides are its low electrical conductance at high frequencies and the required thermal budget to deposit poly Si.

The gate stack for the samples discussed in Chapter 4 and Chapter 5 is fabricated using Ti/Pd. Table 3.2 summarizes three representative fabrication recipes of the nine fabrication cycles that were made for this

**Table 3.1:** Qualitative comparison of common gate materials.

| Material | Resistivity | | Grain Size | Interfaces | Strain |
|---|---|---|---|---|---|
| | Low freq. | High freq. | | | |
| Ti/Pd | Good | OK | Good | Bad | OK |
| Al | Good | Good | Bad | OK | Bad |
| NbTi(N) | Good | Good | Good | Bad | |
| Poly Si | Good | Bad | Good | Good | Good |



project: an initial fabrication cycle (Device A, cycle 1-6) and the runs that produced the devices used in Chapters 4 (Device B, cycle 7) and 5 (Device C, cycle 8-9). Intermediate runs, not shown here, involved minor variations such as adjustments to gate design, gate height, cleaning steps, or electron beam doses. The fabrication cycles one through seven (including Device A and Device B) were executed by me under the supervision of S. V. Amitonov. Cycles eight (Device C) and nine were done by S. Karwal. The yield of all cycles varied widely between all devices being defective and all tested devices producing four quantum dots.

Fig. 3.4 illustrates the layout of the quantum dot region for the three designs. All fabrication runs used one or two 20 mm by 20 mm coupons, each divided into 16 cells. Four cells were allocated to test structures, the remaining twelve housed the devices, occasionally with deliberate design variations.

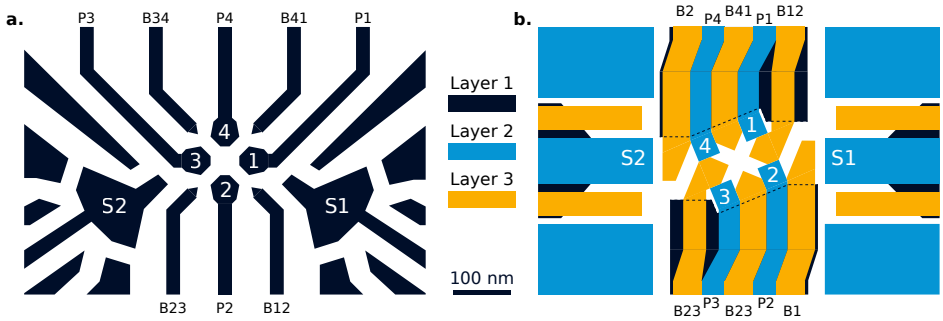


**Figure 3.4: Design schematics of the 2x2 quantum dot arrays.** The design schematics of the 2x2 quantum dot arrays mark the four quantum dots (1-4) with the respective plunger gates (P1-P4), the barriers between (B12-B41) and the two SETs used as charge sensors (S1, S2). **a.** Design schematic of Device A in which most gates are fabricated in a single layer. A global screening gate and a micromagnet were fabricated in the second layer with two lithography steps, without intermediate oxide. For clarity, both are not shown. **b.** Design of Device B and Device C where a multi layer process was used to improve performance. Barriers B1 and B2 are used to control the tunnel coupling of dot $D_2$ and $D_4$ to the adjacent SETs. Also here the micromagnet was omitted from the schematic. Details on the fabrication process are listed in Table 3.2.

**Table 3.2:** Fabrication steps of three exemplary fabrication runs. Excluded in this list are various AFM measurements i.e. after most development and/or lift off steps as well as spin coating and baking of photoresist before dicing the wafer into coupons is omitted. For legibility reasons the table shortens room temperature as RT, isopropyl alcohol as IPA, spin coatings as Spin, Allresists E-Beam resist AR-P 6200.XX to CSAR 0.XX, Shipleys photoresist Microposit S1813 to the product number, optical lithography with a laser writer as OL, development as Dev, Pentyl acetate as Pent.Ac., Shipleys developer Microposit MF-321 to its product number, Evaporation to Evap, Lift-Off as LO, Allresists Remover AR 600-71 to its product number, trimethylaluminium as TMA. Beyond that all spin coatings are done at 4000RPM and the acceleration voltage for all EBL steps was 100kV. The beam step size (BSS) of the EBL correlates with the current, where 86 pA corresponds to a BSS of 1 nm, 1114 pA to 2 nm and 97 nA to 40 nm.

| | Device A | Device B | Device C |
|---|---|---|---|
| Cleaning | $H_2O$ 1 min RT<br>IPA 10 min RT<br>Acetone 5 min RT<br>$H_2O$ 1 min RT | $H_2O$ 1 min RT<br>IPA 10 min RT<br>AR600 15 min 40 °C \| Acetone 5 min RT<br>$H_2O$ 1 min RT | |
| [cntd.] | | | |

| | Device A | | Device B | Device C |
|---|---|---|---|---|
| L1’ | Spin | CSAR 0.04 | Spin | S1813 |
| | Bake | 3 min 150 °C | OL | 321uJ/cm2 |
| | EBL | 250 µC cm$^{-2}$ 86 pA | Bake | 1 min 115 °C |
| | Dev | Pent.Ac. 3 min RT<br>IPA 1 min RT | Dev/Etch | MF321 7 min RT \| MF321 4 min RT<br>$H_2O$ 10+50 s RT |
| | Evap | Ti 1 Å s$^{-1}$ 3 nm,<br>Pd 2 Å s$^{-1}$ 17 nm | Clean | Acetone 1 min RT<br>IPA 1 min RT |
| | LO | AR600-71 15 min 40 °C<br>IPA 1 min RT | Clean | $HNO_3$ 10 min<br>$H_2O$ 1 min |
| L1 | Spin | CSAR 0.04 | Spin | CSAR 0.04 |
| | Bake | 3 min 150 °C | Bake | 3 min 150 °C |
| | EBL | 350 µC cm$^{-2}$ 97 nA | EBL | 250 µC cm$^{-2}$ 86 pA<br>350 µC cm$^{-2}$ 97 nA |
| | Dev | Pent.Ac. 3 min RT<br>IPA 1 min RT | Dev | Pent.Ac. 3 min RT<br>IPA 1 min RT |
| | Evap | Ti 1 Å s$^{-1}$ 3 nm<br>Pd 2 Å s$^{-1}$ 37 nm | Evap | Ti 1 Å s$^{-1}$ 3 nm<br>Pd 2 Å s$^{-1}$ 17 nm |
| | LO | AR600-71 15 min 40 °C<br>IPA 1 min RT | LO | AR600-71 15 min 40 °C<br>IPA 1 min RT |
| | ALD | 50 cycles TMA $H_2O$ | ALD | 50 cycles TMA $H_2O$ |
| L2’ | | | Spin | S1813 |
| | | | OL | 321uJ/cm2 |
| | | | Bake | 1 min 115 °C |
| | | | Dev/Etch | MF321 7 min RT \| MF321 4 min RT<br>$H_2O$ 10+50 s |
| | | | Clean | Acetone 1 min RT<br>IPA 1 min RT |
| L2 | Spin | CSAR 0.04 | Spin | CSAR 0.04 |
| | Bake | 3 min 150 °C | Bake | 3 min 150 °C |
| | EBL | 350 µC cm$^{-2}$ 97 nA | EBL | 250 µC cm$^{-2}$ 86 pA<br>350 µC cm$^{-2}$ 97 nA |
| | Dev | Pent.Ac. 3 min RT<br>IPA 1 min RT | Dev | Pent.Ac. 3 min RT<br>IPA 1 min RT |
| | Evap | Ti 1 Å s$^{-1}$ 3 nm<br>Pd 2 Å s$^{-1}$ 37 nm | Evap | Ti 1 Å s$^{-1}$ 3 nm<br>Pd 2 Å s$^{-1}$ 27 nm |
| | LO | AR600-71 15 min 40 °C<br>IPA 1 min RT<br>Dicing | LO | AR600-71 15 min 40 °C<br>IPA 1 min RT |
| | | | ALD | 50 cycles TMA $H_2O$ |
| L3’ | | | Spin | S1813 |
| | | | OL | 321uJ/cm2 |
| | | | Bake | 1 min 115 °C |
| | | | Dev/Etch | MF321 7 min RT \| MF321 4 min RT<br>$H_2O$ 10+50 s RT |
| | | | Clean | Acetone 1 min RT<br>IPA 1 min RT |
| L3 | | | Spin | CSAR 0.04 |
| | | | Bake | 3 min 150 °C |
| | | | EBL | 250 µC cm$^{-2}$ 86 pA<br>350 µC cm$^{-2}$ 97 nA |
| | | | Dev | Pent.Ac. 3 min RT<br>IPA 1 min RT |
| | | | Evap | Ti 1 Å s$^{-1}$ 3 nm<br>Pd 2 Å s$^{-1}$ 27 nm |
| | | | LO | AR600-71 15 min 40 °C<br>IPA 1 min RT |
| | | | ALD | 50 cycles TMA $H_2O$ |
| [cntd.] | | | | |

| | Device A | Device B | Device C |
|---|---|---|---|
| umag' | | Spin<br>OL<br>Bake<br>Dev/Etch<br>Clean | S1813<br>321uJ/cm2<br>1 min 115 °C<br>MF321 4 min RT<br>$H_2O$ 10+50 s RT<br>Acetone 1 min RT<br>IPA 1 min RT |
| umag | | Bake<br>Spin<br>Bake<br>EBL<br>Dev<br>Evap<br>LO | 150 °C 1 min<br>Spin CSAR 0.13<br>Bake 3 min 150 °C<br>EBL 250 µC cm$^{-2}$ 1114 pA<br>Dev Pent.Ac. 3 min RT<br>IPA 1 min RT<br>Evap Ti 0.5 Å s$^{-1}$ 5 nm<br>Evap Co 1.5 Å s$^{-1}$ 200 nm<br>AR600-71 RT-RT 15-5M<br>AR600-71 50C 60M<br>IPA 1 min RT<br>Dicing |

Even though Device A had a total of three EBL steps and two isolated metallic layers the design was dubbed single-layer design. The second layer (L2) only featured a global screening gate, meant to adjust the overall potential landscape. It was also intended to provide the planned micromagnet (added in subsequent fabrication cycles) with a well defined electrical potential. The first cleaning step strips the photoresist applied before dicing a wafer into the coupons. The first metallic layer is split into a thin (L1') and thick (L1) deposition step. All gates were fabricated using the thin deposition, their fan-out as well as the ohmic contacts used a thicker metallisation to prevent climbing issues at the implantation regions. Eventually conductance measurements found this unnecessary and the two depositions were combined into a single thin deposition (see L1 for Device B/C).

Having all metallic layers and their fan-out in a single layer proved to be suboptimal for control. Isolating four quantum dots with each a single electron was possible, however, the design constraints around the barrier gates diminished their effectiveness and restricted their pulsing range. Most detrimentally, the barrier gate B23 in Fig 3.2**a** caused the quantum dot $D_2$ to merge with the SET S2. The barrier gate was not able to modulate the tunnel coupling between quantum dots $D_2$ and $D_3$ in meaningful ways.

With the development of a reliable multi-layer fabrication process a new design was developed and fabricated. A more aggressive cleaning procedure was used to reduce resist residues from the Prefab steps for Device B. Furthermore before each metal layer an etching step was introduced (L1', L2', L3'). In this step the gate oxide that would otherwise remain below the bond pads is removed such that at ambient temperatures all gates are shorted to the substrate; a measure taken to reduce electrostatic discharge (ESD) related failures. At cryogenic temperature, the substrate no longer conducts and the pads become

electrically isolated again. Device C follows largely the steps of Device B. Notable differences are adjustments to the design, the return to the first cleaning procedure and the additional etching step (umag').

# REFERENCES


[1] F. Pobell. *Matter and Methods at Low Temperatures*. Springer Berlin Heidelberg, 2007. doi: 10.1007/978-3-540-46360-3.

[2] A. T. A. M. de Waele. “Basic Operation of Cryocoolers and Related Thermal Machines”. In: *Journal of Low Temperature Physics* 164.5–6 (June 2011), pp. 179–236. doi: 10.1007/s10909-011-0373-x.

[3] International Telecommunication Union. *ITU-R Recommendation V.431-8: Nomenclature of the Frequency and Wavelength Bands Used in Telecommunications*. https://www.itu.int/dms_pubrec/itu-r/rec/v/R-REC-V.431-8-201508-I!!PDF-E.pdf. [Accessed: 02-01-2025]. Aug. 2015.

[4] Lakeshore. *Cryogenic wire — lakeshore.com*. https://www.lakeshore.com/products/categories/specification/temperature-products/cryogenic-accessories/cryogenic-wire. [Accessed 20-01-2025].

[5] J. M. Martinis, M. H. Devoret, and J. Clarke. “Experimental tests for the quantum behavior of a macroscopic degree of freedom: The phase difference across a Josephson junction”. In: *Physical Review B* 35.10 (Apr. 1987), pp. 4682–4698. doi: 10.1103/physrevb.35.4682.

[6] F. P. Milliken, J. R. Rozen, G. A. Keefe, and R. H. Koch. “50 Ω characteristic impedance low-pass metal powder filters”. In: *Review of Scientific Instruments* 78.2 (Feb. 2007). doi: 10.1063/1.2431770.

[7] K. Bladh, D. Gunnarsson, E. Hürfeld, S. Devi, C. Kristoffersson, B. Smålander, S. Pehrson, T. Claeson, P. Delsing, and M. Taslakov. “Comparison of cryogenic filters for use in single electronics experiments”. In: *Review of Scientific Instruments* 74.3 (Mar. 2003), pp. 1323–1327. doi: 10.1063/1.1540721.

[8] F. Mueller, R. N. Schouten, M. Brauns, T. Gang, W. H. Lim, N. S. Lai, A. S. Dzurak, W. G. van der Wiel, and F. A. Zwanenburg. “Printed circuit board metal powder filters for low electron temperatures”. In: *Review of Scientific Instruments* 84.4 (Apr. 2013). doi: 10.1063/1.4802875.

[9] A. Fukushima, A. Sato, A. Iwasa, Y. Nakamura, T. Komatsuzaki, and Y. Sakamoto. “Attenuation of microwave filters for single-electron tunneling experiments”. In: *IEEE Transactions on Instrumentation and Measurement* 46.2 (Apr. 1997), pp. 289–293. doi: 10.1109/19.571834.

[10] Bluefors. *Coaxial Wiring — bluefors.com*. https://bluefors.com/products/measurement-infrastructure/coaxial-wiring/. [Accessed 20-01-2025].

[11] S. Krinner, S. Storz, P. Kurpiers, P. Magnard, J. Heinsoo, R. Keller, J. Lütolf, C. Eichler, and A. Wallraff. “Engineering cryogenic setups for 100-qubit scale superconducting circuit systems”. In: *EPJ Quantum Technology* 6.1 (May 2019). doi: 10.1140/epjqt/s40507-019-0072-0.

[12] M. Sarsby. *Cooling a Hot Photon Wind (part 1) QuTech Blog*. https://blog.qutech.nl/2020/02/20/cooling-a-hot-photon-wind-part-1/. [Accessed 20-01-2025]. 2020.

[13] Qblox. *Qubit Control Module, Cluster Series 19 Rack Mounted*. https://cdn.prod.website-files.com/653289e64ff83c71222f6bf2/6542566d356461b2605de342_QBLOX_PRODUCTSHEET_CLUSTER-QCM_V1_6_1.pdf. [Accessed 20-01-2025]. 2023.

[14] S. Wartenberg. *RF measurements of die and packages*. en. Microwave Library. Artech House, May 2002.

[15] D. Degli Esposti, B. Paquelet Wuetz, V. Fezzi, M. Lodari, A. Sammak, and G. Scappucci. “Wafer-scale low-disorder 2DEG in 28Si/SiGe without an epitaxial Si cap”. In: *Applied Physics Letters* 120.18 (May 2022). doi: 10.1063/5.0088576.

[16] M. Brauns, S. V. Amitonov, P.-C. Spruijtenburg, and F. A. Zwanenburg. “Palladium gates for reproducible quantum dots in silicon”. In: *Scientific Reports* 8.1 (Apr. 2018). doi: 10.1038/s41598-018-24004-y.

[17] E. J. Connors, J. Nelson, H. Qiao, L. F. Edge, and J. M. Nichol. “Low-frequency charge noise in Si/SiGe quantum dots”. In: *Physical Review B* 100.16 (Oct. 2019). doi: 10.1103/physrevb.100.165305.

[18] T. Thorbeck and N. M. Zimmerman. “Formation of strain-induced quantum dots in gated semiconductor nanostructures”. In: *AIP Advances* 5.8 (Aug. 2015). doi: 10.1063/1.4928320.

[19] J. Park, Y. Ahn, J. A. Tilka, K. C. Sampson, D. E. Savage, J. R. Prance, C. B. Simmons, M. G. Lagally, S. N. Coppersmith, M. A. Eriksson, M. V. Holt, and P. G. Evans. “Electrode-stress-induced nanoscale disorder in Si quantum electronic devices”. In: *APL Materials* 4.6 (June 2016). doi: 10.1063/1.4954054.

[20] S. Fritz, L. Radtke, R. Schneider, M. Weides, and D. Gerthsen. “Optimization of Al/AlOx/Al-layer systems for Josephson junctions from a microstructure point of view”. In: *Journal of Applied Physics* 125.16 (Apr. 2019). doi: 10.1063/1.5089871.

[21] A. Elsayed, M. M. K. Shehata, C. Godfrin, S. Kubicek, S. Massar, Y. Canvel, J. Jussot, G. Simion, M. Mongillo, D. Wan, B. Govoreanu, I. P. Radu, R. Li, P. Van Dorpe, and K. De Greve. “Low charge noise quantum dots with industrial CMOS manufacturing”. In: *npj Quantum Information* 10.1 (July 2024). doi: 10.1038/s41534-024-00864-3.

# 4

# A 2D QUANTUM DOT ARRAY IN PLANAR $^{28}$SI/SIGE

*”All things are difficult before they are easy.”*

Thomas Fuller

*Semiconductor spin qubits have gained increasing attention as a possible platform to host a fault-tolerant quantum computer. First demonstrations of spin qubit arrays have been shown in a wide variety of semiconductor materials. The highest performance for spin qubit logic has been realized in silicon, but scaling silicon quantum dot arrays in two dimensions has proven to be challenging. By taking advantage of high-quality heterostructures and carefully designed gate patterns, we are able to form a tunnel coupled 2 × 2 quantum dot array in a $^{28}$Si/SiGe heterostructure. We are able to load a single electron in all four quantum dots, thus reaching the (1,1,1,1) charge state. Furthermore we characterise and control the tunnel coupling between all pairs of dots by measuring polarisation lines over a wide range of barrier gate voltages. Tunnel couplings can be tuned from about* 30 µeV *up to approximately* 400 µeV*. These experiments provide insightful information on how to design 2D quantum dot array and constitute a first step towards the operation of spin qubits in $^{28}$Si/SiGe quantum dots in two dimensions.*

This chapter has been published in Applied Physics Letters 123, 084002 (08/2023) [1].

Since the original proposal for quantum computation with semiconductor quantum dots [2], remarkable developments have been made. Quantum dot qubits are small in size, compatible with semiconductor manufacturing, and can be operated with single-qubit gate fidelities and two-qubit gate fidelities above 99.9 % [3] and 99 % [4–6] respectively.

The implementation of two-dimensional qubit arrays will allow this technology platform to fully utilize its advantages. In GaAs heterostructures 2x2 and 3x3 quantum dot arrays have already been demonstrated [7–9]. However, hyperfine interaction leads to short dephasing times, preventing high-fidelity operation of qubit arrays. In contrast, group IV materials benefit from nuclear spin-free isotopes, such that quantum coherence can be maintained over much longer times [10].



In recent years, hole quantum dots in Ge/SiGe heterostructures progressed from a single quantum dot to a $4 \times 4$ quantum dot array with shared gate control [11–13]. Parallel to that also silicon based devices have been pushed towards 2D arrays. Using quantum dots confined in the corners of silicon nanowires, several $2 \times N$ quantum dot arrays have been demonstrated, albeit not simultaneously at the single-electron occupancy [14–16]. Furthermore, these devices did not contain separate gates for independent control of the tunnel barriers between neighbouring dots. This limits the controllability for quantum simulations and prevents sweet-spot operation [17–19] of exchange-based quantum gates.

In this work, we present a 2D quantum dot array in gated planar $^{28}$Si/SiGe with barrier gates to control inter-dot tunnel couplings. Four quantum dots in a $2 \times 2$ configuration are formed with occupations controlled down to the last electron. Furthermore, all inter-dot tunnel couplings are characterized as a function of all barrier gate voltages. We demonstrate control over a wide range of tunnel couplings and provide suggestions for future scalable gate designs.

## 4.1. SINGLE ELECTRON OCCUPATION

The $2 \times 2$ quantum dot array investigated in this work is fabricated on a $^{28}Si/Si_{70}Ge_{30}$ heterostructure (see Section 4.4.1). Fig. 4.1**a** shows a false-coloured scanning electron microscope (SEM) image of a nominally identical device, highlighting the three gate layers of the multi-layer gate stack[20]. The screening gates in the first layer (purple) define an active area, reduce the formation of spurious dots and prohibit accumulation of a 2DEG in the gate fan-out region. The second layer (yellow) consists of plunger (P) and accumulation gates. Barrier gates (B) are fabricated in the third layer (red). On top of the gate stack sits a micromagnet. The SEM image in Fig. 4.1**a** is taken before its deposition to highlight the quantum dot gate pattern.

The gate stack defines four quantum dots in a $2 \times 2$ grid (labelled clockwise 1-4) and two SETs (S1 and S2). Gate and dot pitches were loosely adopted from the linear six dot array by Philips et al.[21]. The screening gates around the four quantum dots were kept grounded. Two SETs serve as charge detectors and act as electron reservoirs for the quantum dots $D_2$ and $D_4$ in the $2 \times 2$ array. The quantum dots $D_1$ and $D_3$ are loaded via $D_2$ and $D_4$ respectively. The presented data was taken exclusively with the sensor providing the highest contrast on the chosen dot pair for each measurement.

The 22.5 degree rotation of the square array relative to the micromagnets gives every quantum dot a distinct Zeeman splitting. The relative arrangement of the quantum dots and the SETs allows for sensing charge movements between all possible dot pairs. This is favourable for recording charge polarization lines and spin-to-charge conversion.



Off-chip NbTiN inductors connected to the SET reservoirs and parasitic capacitances form a tank circuit that enables RF reflectometry readout, allowing for fast and accurate detection of the charge occupation of all four quantum dots.

During the device tune-up, we measure the cross-capacitive coupling of all gates to all dots and virtualise them as described in [22] with $vP_i$ ($vB_{ij}$) denoting the virtualised plunger (barrier) gates. The chosen virtual gates compensate the cross-talk onto all dot potentials and maintain the operation point of the charge sensors. The cross-capacitive coupling matrix $\mathbb{M}$, translating the real gate space to the virtual gate space via $\vec{V}^{\text{virt}} = \mathbb{M}\vec{V}^{\text{real}}$, is provided in the Section 4.4.3.

To show control over the charge occupation of the entire $2 \times 2$ array, we measure four charge stability diagrams as depicted in Fig. 4.1**b**. We acquire this data by sweeping the voltages on adjacent virtual plungers gates $vP_i$ and $vP_{(i \bmod 4)+1}$ while monitoring the response of the charge sensors. The coloured circles in the top right corner of each charge stability diagram indicate the position of the quantum dots corresponding to the swept plunger gates.

A honeycomb pattern characteristic of double-dot behaviour is observed for all four plunger pairs. We identify the first electron in the four quantum dots by the absence of any more charge transitions in the lower left corner. Thus we can controllably access the $(N_1, N_2, N_3, N_4) = (1, 1, 1, 1)$ charge state, where $N_i$ denotes the charge occupation of quantum dot $D_i$, and isolate a single spin per quantum dot. The honeycomb patterns in Fig. 4.1**b** also show that all four quantum dots are capacitively coupled to each other.

We note that there are apparent differences in the separation between the consecutive charge transition lines as well as in the slopes of successive charge transition lines. These could be caused by inherent differences and gate-voltage dependent variations in size, position or

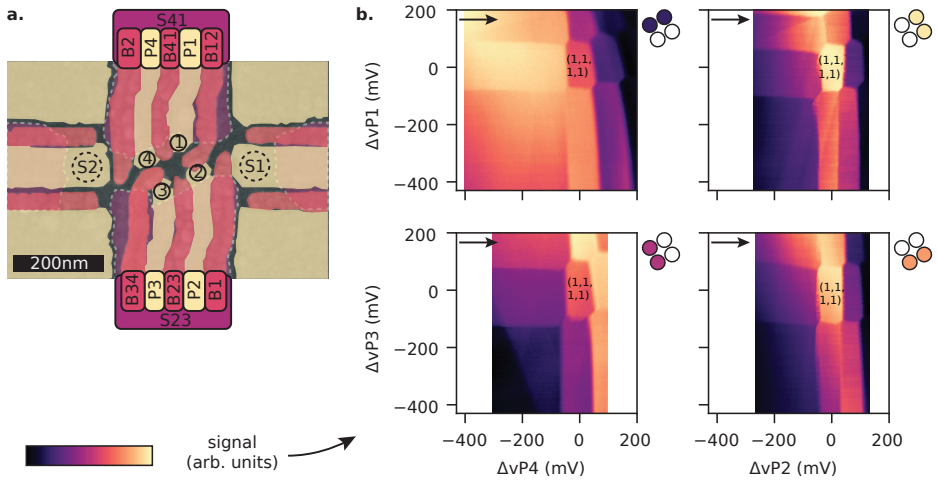


**Figure 4.1: A 2x2 quantum dot array. a.** False coloured SEM image of a nominally identical device to the one used in the measurements. The four quantum dots in the centre are labelled clockwise 1-4 with one sensor on each side marked as S1 and S2. Dashed lines mark the boundaries of the screening gates in the first gate layer. **b.** Charge stability diagrams of nearest-neighbour quantum dots. Coloured circles indicate the quantum dots of the swept virtual plunger gates while the quantum dots corresponding to the white circles remained with one electron each. The point $[0\ \text{mV}, 0\ \text{mV}]$ corresponds to the same gate voltages for all four scans. At this operating point, the (1,1,1,1) charge state is reached, with one electron per quantum dot. For the charge stability diagrams of $D_1D_2$ and $D_2D_3$ sensor S1 was used while for $D_3D_4$ and $D_4D_1$ sensor S2 was chosen. At $\Delta vP_i = 0$ mV, the corresponding physical voltages on the gates are set to 2566 mV, 1831 mV, 3173 mV, 2487 mV for plungers 1-4, respectively. The arrows in the top left corner of each charge stability diagram indicate the direction of the scans.

lever arm of the four intended quantum dots. Alternatively, they might be the charging signature of additional quantum dots in the close vicinity. While we cannot fully rule out the presence of such stray dots at higher occupations, we can reliably reach the (1,1,1,1) charge state in the 2 × 2 configuration of the array.

Next to the expected charge transitions, we observe additional diagonal features e.g. in Fig. 4.1**b**, which we associate with spurious defects in our system. These defects capacitively couple to the charge sensor but there is no or only very weak capacitive interaction with the four intentional quantum dots of the 2 × 2 array.

## 4.2. INTER-DOT TUNNEL COUPLING

Besides a well-defined charge state, controlled inter-dot tunnel couplings are essential for the implementation of robust exchange-based quantum gates or the execution of analog quantum simulation. Therefore, we probe the system evolution as a function of the voltage applied to the virtual barrier gates $vB_{ij}$ located between the plunger gates of quantum dot $D_i$ and $D_j$ with $j = (i \bmod 4) + 1$. The tunnel coupling diagonally between $D_1$ and $D_3$ and anti-diagonally between $D_2$ and $D_4$ has no dedicated barrier gate and thus is not independently controllable. The influence of other barrier gates on the (anti-)diagonal tunnel coupling is presented in Fig. 4.3.

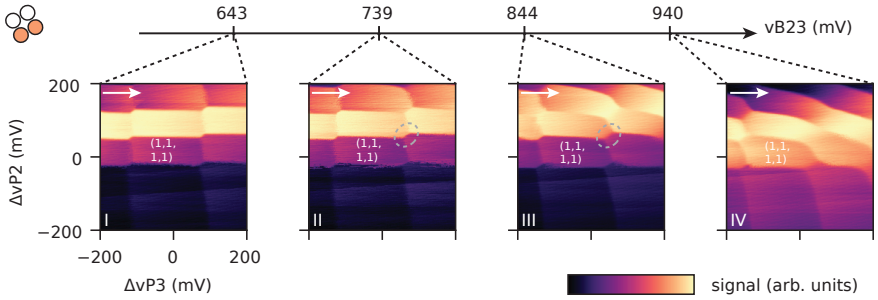


**Figure 4.2: Inter-dot tunnel coupling.** Response of the charge stability diagram of $D_2$ and $D_3$ to changes of virtual barrier voltage $vB_{23}$, as indicated by the arrow above the charge stability diagrams. Small arrows in the top left corner of each panel indicate the scan direction. From panel I to IV, we observe a gradual increase in both the capacitive and tunnel coupling between the two dots. Similar data were taken for all other nearest-neighbouring pairs and are displayed in the Fig. 4.5.

Fig. 4.2 shows the evolution of the charge stability diagram of $D_2$ and $D_3$ while changing the virtual barrier gate voltage $vB_{23}$. The sequence of panels allows us to qualitatively assess the influence of the barrier on the capacitive coupling and tunnel coupling between the involved quantum dots. From panel I through IV, we observe that the separation between the triple points increases, which indicates an increase in the capacitive coupling between the dots. In addition, we observe that the interdot charge transition is increasingly blurred (see the circled transitions) and the boundaries of the charge stability diagram are increasingly rounded. Both are indicative of an increased interdot tunnel coupling. In panel IV, for transition lines with $N_2 + N_3 \geq 4$ the rounding is so strong that the quantum dots have mostly merged into a single large dot.

To quantitatively determine the effect of the barrier voltage on the tunnel coupling, we measure polarisation lines along the detuning

axis $\epsilon_{ij}/\alpha_{\epsilon ij} = \mathrm{vP}_i - \mathrm{vP}_j$, with $\alpha_{\epsilon ij}$ denoting the lever arm, across the $(N_i, N_j) = (1, 0)$ to $(0, 1)$ interdot transition, as shown in Fig. 4.3**a**. The remaining dots were kept in the (1,1) charge occupation. Scanning along this detuning axis moves the electron from dot 2 to dot 3 ($(N_1, N_2, N_3, N_4) = (1, 1, 0, 1)$ to $(1, 0, 1, 1)$), resulting in a step response in the sensor signal as seen in Fig. 4.3**b**. This step response is broadened by both the electron temperature $T_e \leq 78.5 \pm 2.2$ mK and the tunnel coupling $t$, and can be fitted using $S_{\mathrm{Sig}} = \frac{\epsilon}{\Omega} \tanh \frac{\Omega}{2k_b T_e}$ with $\Omega = \sqrt{\epsilon^2 + 4t^2}$ and $\epsilon$ the detuning between the two quantum dots [23]. Additional slopes and offsets of the sensor signal caused by imperfect virtualisation or drifts are taken into account in the used fitting procedure [24]. We note that the error in the extracted tunnel coupling values is dominated by the uncertainty in the lever arms.

We systematically extract the dependency of the inter-dot tunnel couplings $t_{n,m}$ between all dot pairs $(\mathrm{D}_n, \mathrm{D}_m)$ with respect to all barrier voltages $\mathrm{vB}_{ij}$. Fig. 4.3**c** shows the resulting tunnel couplings $t_{n,m}$ grouped by barrier gates $\mathrm{vB}_{ij}$. As in previous works, fading contrast along the polarization lines prevented us from characterizing tunnel couplings up to higher values. We observe that changing the barrier voltage $\mathrm{vB}_{ij}$ affects only the corresponding tunnel couplings $t_{ij}$ significantly, while keeping the other tunnel couplings largely constant. Note that the virtual gate matrix compensates for cross-talk of the barrier gates onto all dot potentials, but does not account for possible cross-talk on the tunnel couplings.

We furthermore find that below a given voltage (which is different for each $\mathrm{vB}_{ij}$), the influence of the barrier gate voltage on the corresponding tunnel coupling vanishes and a residual tunnel coupling remains. Across all four neighbouring dot pairs, the residual tunnel coupling is in the range between 30 $\mu$eV and 200 $\mu$eV.

We extend this characterisation to the (anti-)diagonal tunnel couplings. Fig. 4.3**d** presents the influence of the four barrier gates on the diagonal and anti-diagonal tunnel coupling respectively. While the anti-diagonal tunnel coupling $t_{2,4}$ is elevated and can be modulated using $\mathrm{vB}_{12}$ in particular, the diagonal tunnel coupling $t_{1,3}$ is not systematically influenced by any barrier gate and remains in many cases lower than all other tunnel couplings, albeit far from zero.

## 4.3. DISCUSSION AND OUTLOOK

We demonstrated the first 2D quantum dot array in a planar silicon technology and operated the four quantum dots in the single electron regime, consistently achieving the $(1, 1, 1, 1)$ charge state. Furthermore, the barrier gates allow us to independently control the interdot tunnel couplings. However, the residual tunnel couplings observed in this sample are higher than the typical tunnel coupling of 1-10 $\mu$eV used

in spin qubit experiments [25]. Presumably the close proximity of the screening gates to the centre of the plunger gates compresses the quantum dots towards the centre of the 2 × 2 array and hence towards each other, leading to rather large tunnel couplings. Furthermore, we see in Fig. 4.3 that at low tunnel coupling values, the tunnel coupling barely responds to the barrier gate voltages anymore. The compressed position of the quantum dots in the centre region enhances also the diagonal coupling between them. While analog quantum simulation and quantum computation can benefit from diagonal tunnel coupling, the lack of dedicated control over magnitude and directionality i.e. diagonal versus anti-diagonal, also poses limitations. Suppressing any diagonal coupling with a centre gate as demonstrated in a GaAs 2 × 2 array could be a suitable way to circumvent this issue [26].



The encountered challenges help to identify possible improvements in the design of planar 2 × 2 $^{28}$Si/SiGe quantum dot arrays. Specifically, moving the screening gates away from the centre of the array is expected to yield lower tunnel couplings, as the electrons are not squeezed towards each other as much. The experiments also offer relevant learnings for scaling to larger arrays. For instance, changing the device architecture from a square array to a triangular array will alleviate the issues regarding undesired diagonal tunnel couplings [27, 28]. Furthermore, in order to maintain control of individual tunnel couplings, either more sophisticated patterning techniques must be applied to route gates to the inside of a larger array [29], or crossbar addressing must be employed [13, 30, 31]. In both cases, the observations made for the present device provide guidance for suitable plunger and barrier gate pitches and dimensions.

## 4.4. SUPPLEMENTARY INFORMATION

### 4.4.1. DEVICE FABRICATION AND SCREENING

This device is fabricated on a $^{28}$Si/Si$_{70}$Ge$_{30}$ heterostructure. A 2.5 $\mu$m strain relaxed Si$_{70}$Ge$_{30}$ buffer layer makes the foundation. On top of it the isotopically enriched $^{28}$Si quantum well is grown. It has a residual $^{29}$Si concentration of 0.08% and was measured to be 9.0 ± 0.5 nm thick. Afterwards a 30 nm thick Si$_{70}$Ge$_{30}$ spacer is grown to reduce strain relaxation in the quantum well and separate it from the gate dielectric. The heterostructure is finalized with a 1 nm silicon cap [32]. The gate stack is separated from the heterostructure by 10 nm $Al_2O_3$, formed by atomic-layer deposition (ALD) at 300 °C. The three gate layers of the gate stack are made from Ti:Pd with thicknesses of 3:17, 3:27 and 3:27 nm and are patterned using electron beam lithography, electron beam evaporation and lift off. Each layer is electrically isolated from the previous layer by a 5 nm $Al_2O_3$ dielectric grown by ALD. Above the three gate layers a micromagnet is fabricated from Ti:Co (5:200 nm).

After fabrication every device was screened by measuring turn-on curves and testing for gate leakage or shorted gates at 4.2 K with a dipstick in liquid helium. This high turnaround testing allows to verify the basic functionality of the device and quickly filter out defective devices. After verifying the functionality of all gates, NbTiN inductors are added to the ohmic contacts to enable RF-readout. To address electrostatic discharge concerns during rebonding, we screen the device a second time in liquid helium to verify that no damage has been done. Then we cool down the devices in a Bluefors LD400 dilution refrigerator to its base temperature of around 10 mK.



### 4.4.2. SETUP

The room-temperature control electronics to operate this device are separated into ac electronics in one rack and dc electronics in a second one. In the latter, several in-house built serial peripheral interface (SPI) racks host 18 bit digital-to-analog converter (DAC) modules which provide the required dc voltages. Voltage dividers were used to apply an accurate source-drain bias when needed. The currents are measured with a Keithley 2000 Multimeter (placed in the ac rack) via an in-house developed transconductance amplifier. The dc rack is powered by batteries which are continuously charged via gyrators and filters.

The ac rack comprises the host computer, a Keysight chassis (M9019A) and an additional dedicated RF SPI rack. The circuitry for RF reflectometry measurements consists of two in-house built RF sources, a combiner (Mini-Circuits ZFSC-2-5-S+), a 15 dB coupler (Mini-Circuits ZEDC-15-2B) at the mixing chamber stage, a cryo-amplifier at the 4K stage (Cosmic Microwave Technology Inc. CITLF3), a room temperature amplifier, two IQ-mixers and a Keysight digitizer (M3102A). The coaxial lines from 4 K to the mixing chamber flange are made from NbTiN to ensure a high signal quality and low thermal conductance. From 4 K to room temperature, SCuNi-CuNi cables are used. Discrete attenuators with a total attenuation of 23 dB are distributed over the various temperature stages on the downward path.

Next to the digitizer, several Keysight AWG modules (M3202A) are situated in the same chassis and connected via a PCIe connection to a host computer. SCuNi-CuNi 0.86 mm coaxial cables are used from room temperature to the mixing chamber plate. Also on these lines discrete attenuators are mounted, with a total attenuation ranging from 12 dB to 20 dB (typically we equip the barrier gates with lower attenuation than the plunger gates). From the mixing chamber flange to the sample PCB, hand-formable 0.086" coaxial cables were used to route both RF and AWG signals. Bias tees on the sample PCB combine the ac pulses and dc voltages. Ferrite cores and dc blocks were installed at room temperature to suppress 50 Hz noise.

### 4.4.3. VIRTUAL GATE MATRIX

The virtual gate matrix defining the virtual gates in the charge stability diagrams of Fig. 4.1 is displayed in Fig. 4.4. Note that we constantly adapted the virtual gate matrices throughout the measurements to improve the compensation of cross capacitive effects on the plunger gates of the quantum dots and SETs.

### 4.4.4. QUALITATIVE TUNNEL COUPLING CONTROL

Fig. 4.5 shows the influence of all barrier gates on the charge stability diagrams of their neighbouring quantum dots. Fig. 4.5**b** is replicated from Fig. 4.2. All barriers show similar influence on the charge stability diagram as discussed by way of example for barrier $vB_{23}$ in the main text.



### 4.4.5. ELECTRON TEMPERATURE AND DETUNING LEVER ARM CALCULATION

To estimate the electron temperature, we measure the thermal broadening of Coulomb peaks of SET S1 using the equations provided by [33]. We sweep gate $B_1$ as it has a smaller lever arm compared to the SET plunger gate and therefore allows us to sweep across a Coulomb peak with a much finer resolution, improving the fit quality. Fig. 4.6**a** shows the Coulomb diamonds that were used to calculate the lever arm of gate $B_1$. We combine the slopes $m_S$ and $m_D$ of the Coulomb diamonds to compute the lever arm $\alpha_{B1}$ with $\alpha_{B1} = |\frac{m_S m_D}{m_S - m_D}| \approx 0.027 \pm 0.003$. The stated uncertainty is based on bounding the slopes extracted from the Coulomb diamond from below and from above by eye. The horizontal trace at $V_{SD} \approx -1150$ $\mu$V shown in Fig. 4.6**c** was used to upper bound the electron temperature to $T_e \leq 80$ mK.

Furthermore we require the lever arms of the plunger gates to convert the detuning axis $\epsilon_{ij}$ from gate voltage to energy. Due to the high tunnel coupling, photon-assisted tunnelling measurements with the available microwave source were unsuccessful. Instead we estimate the lever arms of the quantum dots via the slope of their interdot transitions.

We convert the lever arm of gate $B_1$ to the lever arm of virtual plunger gate $vS_1$ using the ratio of the sensing dot peak spacing as measured when scanning gate voltage $vS_1$ versus that measured when scanning $B_1$. We estimate the error introduced by estimating the peak spacing of the Coulomb peaks to be below 10%. From here we can successively use the angle of the interdot transitions to calculate the lever arm ratio between all other gates. For example, Fig. 4.6**b** shows the manually fitted interdot transition used to calculate the lever arm ratio of plunger gate of $vS_1$ and $vP_2$. Similar as before, we bound the error by over- and underestimating the slope of the interdot transition by eye. For

the plunger gates vP1 through vP4 we find lever arms of $0.071 \pm 0.016$ (vP1), $0.073 \pm 0.013$ (vP2), $0.044 \pm 0.009$ (vP3), $0.080 \pm 0.017$ (vP4). The square geometry allows for a consistency check as the lever arm of e.g. $D_4$ can be calculated via S1-$D_2$-$D_3$-$D_4$ but also via S1-$D_2$-$D_1$-$D_4$. The found differences from using different paths fell within error of the final value.

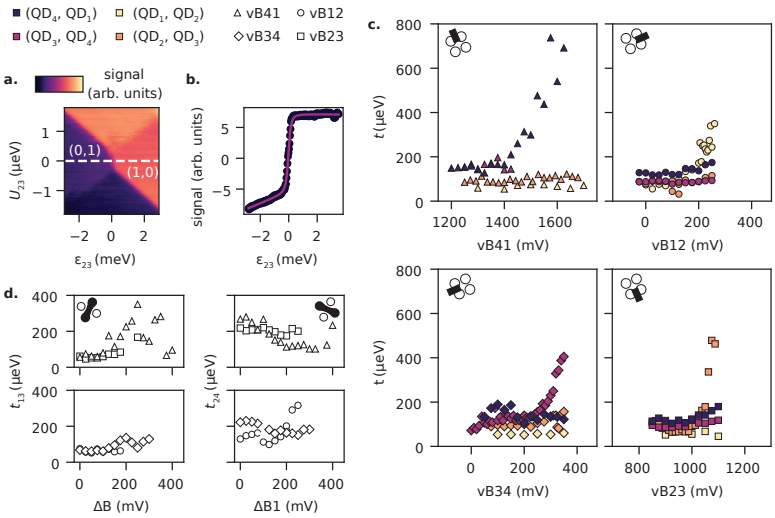


**Figure 4.3: Controllability of inter-dot tunnel couplings.** **a.** Exemplary charge stability diagram around the (1,0) to (0,1) transition for $D_2$ and $D_3$ as a function of the interdot detuning $\epsilon_{23}$ and $U_{23}/\alpha_{U23} = vP_2 + vP_3$. The dashed line indicates the detuning axis used to measure polarisation lines. **b.** Example of a measured (dots) and fitted (solid line) polarisation line for $D_2$ and $D_3$. **c.** Dependence of the tunnel couplings extracted from polarization lines between neighbouring quantum dots on each of the four virtual barrier gate voltages. The plots are ordered to follow the physical position of the barrier gate e.g. barrier $vB_{41}$ situated in the top left corner of the quantum dot array is depicted in the top left plot. The legend for symbols and colours is shown above panels **a** and **b**. We note that the dc voltages of barriers $vB_{12}$ ($vB_{23}$) and $vB_{34}$ ($vB_{41}$) are of comparable values, which is consistent with the symmetries of the gate pattern. Between scans we adjusted gate voltages of uninvolved gates to retain a high visibility. These adjustments were done in such a way that all uninvolved barrier gates remained in the small (residual) tunnel coupling regime. On several occasions, insufficient contrast between the (1,0) and (0,1) charge states limited the data we were able to reliably fit. These data points are thus not available. **d.** Diagonal tunnel coupling and anti-diagonal tunnel coupling as a function of all four virtual barrier gate voltages. The panels were split into two parts for both the diagonal and anti-diagonal coupling to keep the data points visible. The physical gate voltages used at $\Delta vB = 0$ mV varies between data sets, as the voltages were slightly adjusted. As in **c** uninvolved barrier gates remained in the residual tunnel coupling regime. Note also that in **c** and **d** the charge states vary between scans, depending on which dots each polarization line connects.

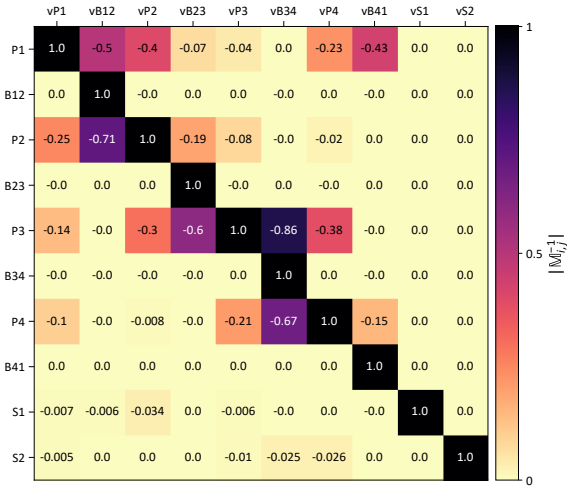


**Figure 4.4: Virtual gate matrix.** Virtual gate matrix ($\mathbb{M}^{-1}$) during the recording of the charge stability diagrams of Fig. 4.1

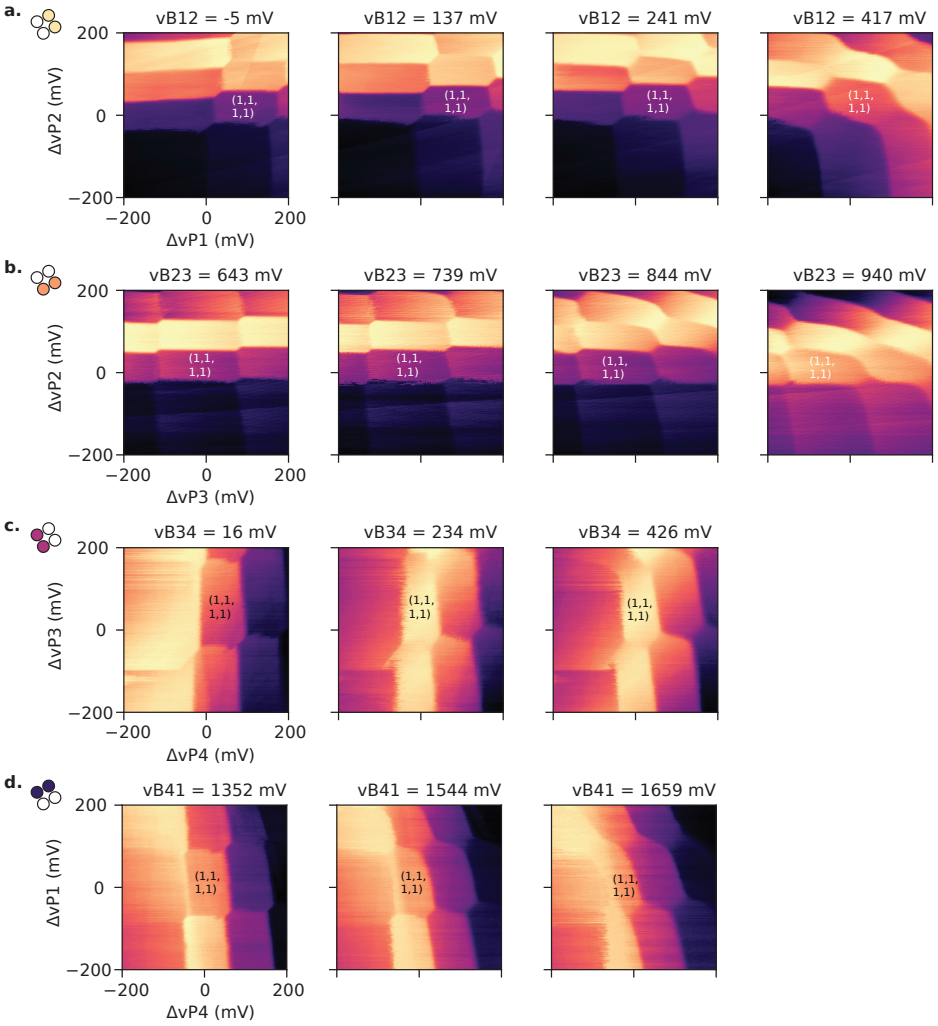


**Figure 4.5: Inter-dot tunnel coupling.** Charge stability diagrams for all four quantum dot pairs for several values of the voltage on the barrier gate between the respective dots. Pictograms on the left indicate the quantum dot pair used in the respective row. To ensure comparability every scan is around the (1,1,1,1) regime as indicated.

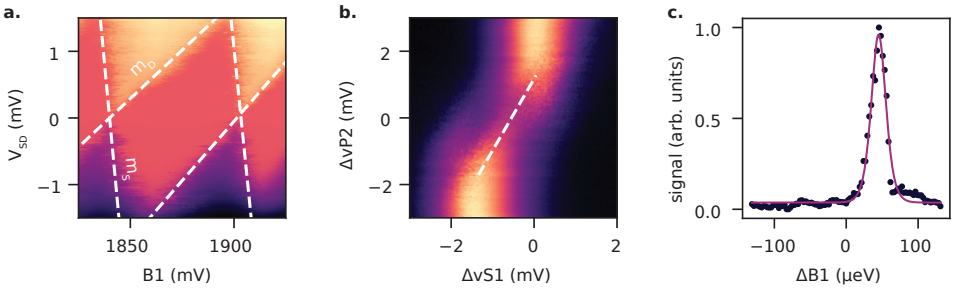


**Figure 4.6: Electron temperature and detuning lever arm calculation. a.** Coulomb diamonds used to extract the lever arm of gate B1. White dashed lines indicate the used slopes. **b.** High resolution interdot transition of sensing dot S1 and $D_2$ showing the manual fit (dashed line) to determine the lever arm ratio between the respective plunger gates. **c.** Measured (dots) and fitted (solid line) Coulomb peak used to estimate the electron temperature. The Coulomb peak is the smallest measured peak at the effective zero bias voltage.

# REFERENCES


[1] F. K. Unseld, M. Meyer, M. T. Madzik, F. Borsoi, S. L. de Snoo, S. V. Amitonov, A. Sammak, G. Scappucci, M. Veldhorst, and L. M. K. Vandersypen. “A 2D quantum dot array in planar 28Si/SiGe”. In: *Applied Physics Letters* 123.8 (Aug. 2023). doi: 10.1063/5.0160847.

[2] D. Loss and D. P. DiVincenzo. “Quantum computation with quantum dots”. In: *Physical Review A* 57.1 (Jan. 1998), pp. 120–126. doi: 10.1103/physreva.57.120.

[3] J. Yoneda, K. Takeda, T. Otsuka, T. Nakajima, M. R. Delbecq, G. Allison, T. Honda, T. Kodera, S. Oda, Y. Hoshi, N. Usami, K. M. Itoh, and S. Tarucha. “A quantum-dot spin qubit with coherence limited by charge noise and fidelity higher than 99.9%”. In: *Nature Nanotechnology* 13.2 (Dec. 2017), pp. 102–106. doi: 10.1038/s41565-017-0014-x.

[4] X. Xue, M. Russ, N. Samkharadze, B. Undseth, A. Sammak, G. Scappucci, and L. M. K. Vandersypen. “Quantum logic with spin qubits crossing the surface code threshold”. In: *Nature* 601.7893 (Jan. 2022), pp. 343–347. doi: 10.1038/s41586-021-04273-w.

[5] A. Noiri, K. Takeda, T. Nakajima, T. Kobayashi, A. Sammak, G. Scappucci, and S. Tarucha. “Fast universal quantum gate above the fault-tolerance threshold in silicon”. In: *Nature* 601.7893 (Jan. 2022), pp. 338–342. doi: 10.1038/s41586-021-04182-y.

[6] A. Mills, C. Guinn, M. Feldman, A. Sigillito, M. Gullans, M. Rakher, J. Kerckhoff, C. Jackson, and J. Petta. “High-Fidelity State Preparation, Quantum Control, and Readout of an Isotopically Enriched Silicon Spin Qubit”. In: *Physical Review Applied* 18.6 (Dec. 2022). doi: 10.1103/physrevapplied.18.064028.

[7] J. P. Dehollain, U. Mukhopadhyay, V. P. Michal, Y. Wang, B. Wunsch, C. Reichl, W. Wegscheider, M. S. Rudner, E. Demler, and L. M. K. Vandersypen. “Nagaoka ferromagnetism observed in a quantum dot plaquette”. In: *Nature* 579.7800 (2020), pp. 528–533. doi: 10.1038/s41586-020-2051-0.

[8] P.-A. Mortemousque, B. Jadot, E. Chanrion, V. Thiney, C. Bäuerle, A. Ludwig, A. D. Wieck, M. Urdampilleta, and T. Meunier. “Enhanced Spin Coherence while Displacing Electron in a Two-Dimensional Array of Quantum Dots”. In: *PRX Quantum* 2.3 (Aug. 2021). doi: 10.1103/prxquantum.2.030331.

[9] F. Fedele, A. Chatterjee, S. Fallahi, G. C. Gardner, M. J. Manfra, and F. Kuemmeth. “Simultaneous Operations in a Two-Dimensional Array of Singlet-Triplet Qubits”. In: *PRX Quantum* 2.4 (Oct. 2021). doi: 10.1103/prxquantum.2.040306.

[10] P. Stano and D. Loss. “Review of performance metrics of spin qubits in gated semiconducting nanostructures”. In: *Nature Reviews Physics* 4.10 (Aug. 2022), pp. 672–688. doi: 10.1038/s42254-022-00484-w.

[11] N. W. Hendrickx, W. I. L. Lawrie, M. Russ, F. van Riggelen, S. L. de Snoo, R. N. Schouten, A. Sammak, G. Scappucci, and M. Veldhorst. “A four-qubit germanium quantum processor”. In: *Nature* 591.7851 (Mar. 2021), pp. 580–585. doi: 10.1038/s41586-021-03332-6.

[12] F. van Riggelen, W. I. L. Lawrie, M. Russ, N. W. Hendrickx, A. Sammak, M. Rispler, B. M. Terhal, G. Scappucci, and M. Veldhorst. “Phase flip code with semiconductor spin qubits”. In: *npj Quantum Information* 8.1 (Oct. 2022). doi: 10.1038/s41534-022-00639-8.

[13] F. Borsoi, N. W. Hendrickx, V. John, S. Motz, F. van Riggelen, A. Sammak, S. L. de Snoo, G. Scappucci, and M. Veldhorst. “Shared control of a 16 semiconductor quantum dot crossbar array”. In: *arXiv* (2022). doi: 10.48550/ARXIV.2209.06609.

[14] W. Gilbert, A. Saraiva, W. H. Lim, C. H. Yang, A. Laucht, B. Bertrand, N. Rambal, L. Hutin, C. C. Escott, M. Vinet, and A. S. Dzurak. “Single-Electron Operation of a Silicon-CMOS 2 $\times$ 2 Quantum Dot Array with Integrated Charge Sensing”. In: *Nano Letters* 20.11 (Oct. 2020), pp. 7882–7888. doi: 10.1021/acs.nanolett.0c02397.

[15] E. Chanrion, D. J. Niegemann, B. Bertrand, C. Spence, B. Jadot, J. Li, P.-A. Mortemousque, L. Hutin, R. Maurand, X. Jehl, M. Sanquer, S. D. Franceschi, C. Bäuerle, F. Balestro, Y.-M. Niquet, M. Vinet, T. Meunier, and M. Urdampilleta. “Charge Detection in an Array of CMOS Quantum Dots”. In: *Physical Review Applied* 14.2 (Aug. 2020). doi: 10.1103/physrevapplied.14.024066.

[16] F. Ansaloni, H. Bohuslavskyi, F. Fedele, T. Rasmussen, B. Brovang, F. Berritta, A. Heskes, J. Li, L. Hutin, B. Venitucci, B. Bertrand, M. Vinet, Y.-M. Niquet, A. Chatterjee, and F. Kuemmeth. “Gate reflectometry

in dense quantum dot arrays". In: *New Journal of Physics* 25.3 (Mar. 2023), p. 033023. doi: 10.1088/1367-2630/acc126.

[17] F. Martins, F. K. Malinowski, P. D. Nissen, E. Barnes, S. Fallahi, G. C. Gardner, M. J. Manfra, C. M. Marcus, and F. Kuemmeth. "Noise Suppression Using Symmetric Exchange Gates in Spin Qubits". In: *Physical Review Letters* 116.11 (Mar. 2016). doi: 10.1103/physrevlett.116.116801.

[18] M. Reed, B. Maune, R. Andrews, M. Borselli, K. Eng, M. Jura, A. Kiselev, T. Ladd, S. Merkel, I. Milosavljevic, E. Pritchett, M. Rakher, R. Ross, A. Schmitz, A. Smith, J. Wright, M. Gyure, and A. Hunter. "Reduced Sensitivity to Charge Noise in Semiconductor Spin Qubits via Symmetric Operation". In: *Physical Review Letters* 116.11 (Mar. 2016). doi: 10.1103/physrevlett.116.110402.

[19] B. Bertrand, H. Flentje, S. Takada, M. Yamamoto, S. Tarucha, A. Ludwig, A. D. Wieck, C. Bäuerle, and T. Meunier. "Quantum Manipulation of Two-Electron Spin States in Isolated Double Quantum Dots". In: *Physical Review Letters* 115.9 (Aug. 2015). doi: 10.1103/physrevlett.115.096801.

[20] W. I. L. Lawrie, H. G. J. Eenink, N. W. Hendrickx, J. M. Boter, L. Petit, S. V. Amitonov, M. Lodari, B. P. Wuetz, C. Volk, S. G. J. Philips, G. Droulers, N. Kalhor, F. van Riggelen, D. Brousse, A. Sammak, L. M. K. Vandersypen, G. Scappucci, and M. Veldhorst. "Quantum dot arrays in silicon and germanium". In: *Applied Physics Letters* 116.8 (Feb. 2020), p. 080501. doi: 10.1063/5.0002013.

[21] S. G. J. Philips, M. T. Mądzik, S. V. Amitonov, S. L. de Snoo, M. Russ, N. Kalhor, C. Volk, W. I. L. Lawrie, D. Brousse, L. Tryputen, B. P. Wuetz, A. Sammak, M. Veldhorst, G. Scappucci, and L. M. K. Vandersypen. "Universal control of a six-qubit quantum processor in silicon". In: *Nature* 609.7929 (Sept. 2022), pp. 919–924. doi: 10.1038/s41586-022-05117-x.

[22] C. Volk, A. M. J. Zwerver, U. Mukhopadhyay, P. T. Eendebak, C. J. van Diepen, J. P. Dehollain, T. Hensgens, T. Fujita, C. Reichl, W. Wegscheider, and L. M. K. Vandersypen. "Loading a quantum-dot based "Qubyte" register". In: *npj Quantum Information* 5.1 (Apr. 2019). doi: 10.1038/s41534-019-0146-y.

[23] L. DiCarlo, H. J. Lynch, A. C. Johnson, L. I. Childress, K. Crockett, C. M. Marcus, M. P. Hanson, and A. C. Gossard. "Differential Charge Sensing and Charge Delocalization in a Tunable Double Quantum Dot". In: *Physical Review Letters* 92.22 (June 2004). doi: 10.1103/physrevlett.92.226801.

[24] C. J. van Diepen, P. T. Eendebak, B. T. Buijtendorp, U. Mukhopadhyay, T. Fujita, C. Reichl, W. Wegscheider, and L. M. K. Vandersypen. “Automated tuning of inter-dot tunnel coupling in double quantum dots”. In: *Applied Physics Letters* 113.3 (July 2018), p. 033101. doi: 10.1063/1.5031034.

[25] T. J. Knapp, R. T. Mohr, Y. S. Li, B. Thorgrimsson, R. H. Foote, X. Wu, D. R. Ward, D. E. Savage, M. G. Lagally, M. Friesen, S. N. Coppersmith, and M. A. Eriksson. “Characterization of a gate-defined double quantum dot in a Si/SiGe nanomembrane”. In: *Nanotechnology* 27.15 (Mar. 2016), p. 154002. doi: 10.1088/0957-4484/27/15/154002.

[26] U. Mukhopadhyay, J. P. Dehollain, C. Reichl, W. Wegscheider, and L. M. K. Vandersypen. “A $2 \times 2$ quantum dot array with controllable inter-dot tunnel couplings”. In: *Applied Physics Letters* 112.18 (Apr. 2018), p. 183505. doi: 10.1063/1.5025928.

[27] A. Noiri, K. Kawasaki, T. Otsuka, T. Nakajima, J. Yoneda, S. Amaha, M. R. Delbecq, K. Takeda, G. Allison, A. Ludwig, A. D. Wieck, and S. Tarucha. “A triangular triple quantum dot with tunable tunnel couplings”. In: *Semiconductor Science and Technology* 32.8 (July 2017), p. 084004. doi: 10.1088/1361-6641/aa7596.

[28] H. Flentje, P.-A. Mortemousque, R. Thalineau, A. Ludwig, A. D. Wieck, C. Bäuerle, and T. Meunier. “Coherent long-distance displacement of individual electron spins”. In: *Nature Communications* 8.1 (Sept. 2017). doi: 10.1038/s41467-017-00534-3.

[29] W. Ha, S. D. Ha, M. D. Choi, Y. Tang, A. E. Schmitz, M. P. Levendorf, K. Lee, J. M. Chappell, T. S. Adams, D. R. Hulbert, E. Acuna, R. S. Noah, J. W. Matten, M. P. Jura, J. A. Wright, M. T. Rakher, and M. G. Borselli. “A Flexible Design Platform for Si/SiGe Exchange-Only Qubits with Low Disorder”. In: *Nano Letters* 22.3 (Nov. 2021), pp. 1443–1448. doi: 10.1021/acs.nanolett.1c03026.

[30] M. Veldhorst, H. G. J. Eenink, C. H. Yang, and A. S. Dzurak. “Silicon CMOS architecture for a spin-based quantum computer”. In: *Nature Communications* 8.1 (Dec. 2017). doi: 10.1038/s41467-017-01905-6.

[31] R. Li, L. Petit, D. P. Franke, J. P. Dehollain, J. Helsen, M. Steudtner, N. K. Thomas, Z. R. Yoscovits, K. J. Singh, S. Wehner, L. M. K. Vandersypen, J. S. Clarke, and M. Veldhorst. “A crossbar network for silicon quantum dot qubits”. In: *Science Advances* 4.7 (July 2018). doi: 10.1126/sciadv.aar3960.

[32] D. Degli Esposti, B. Paquelet Wuetz, V. Fezzi, M. Lodari, A. Sammak, and G. Scappucci. “Wafer-scale low-disorder 2DEG in 28Si/SiGe without an epitaxial Si cap”. In: *Applied Physics Letters* 120.18 (May 2022). doi: 10.1063/5.0088576.

[33] L. Petit, J. Boter, H. Eenink, G. Droulers, M. Tagliaferri, R. Li, D. Franke, K. Singh, J. Clarke, R. Schouten, V. Dobrovitski, L. Vandersypen, and M. Veldhorst. “Spin Lifetime and Charge Noise in Hot Silicon Quantum Dot Qubits”. In: *Physical Review Letters* 121.7 (Aug. 2018). doi: 10.1103/physrevlett.121.076801.

# 5

# BASEBAND CONTROL OF SINGLE-ELECTRON SILICON SPIN QUBITS IN TWO DIMENSIONS

*Shoot for the moon.*
*Even if you miss, you'll land among the stars.*

Les Brown

*Micromagnet-enabled EDSR is an established method of high-fidelity single-spin control in silicon. However, the resulting architectural limitations have restrained silicon quantum processors to one-dimensional arrays, and heating effects from the associated microwave dissipation exacerbates crosstalk during multi-qubit operations. In contrast, qubit control based on hopping spins has recently emerged as a compelling primitive for high-fidelity baseband control in sparse two-dimensional hole arrays in germanium. In this work, we commission a $^{28}$Si/SiGe 2x2 quantum dot array both as a four-qubit device with pairwise exchange interactions using established EDSR techniques and as a two-qubit device using baseband hopping control. In this manner, we can evaluate the two modes of operation in terms of fidelity, coherence, and crosstalk. We establish a lower bound on the fidelity of the hopping gate of*

This chapter has been submitted to Nature Communications [1].

*99.50(6) %, which is similar to the average fidelity of the resonant gate of 99.54(4) %. Lowering the external field to reach the hopping regime nearly doubles the measured $T_2^H$, suggesting a reduced coupling to charge noise. Finally, the hopping gate circumvents the transient pulse-induced resonance shift. To further motivate the hopping gate approach as an attractive means of scaling silicon spin-qubit arrays, we propose an extensible nanomagnet design that enables engineered baseband control of large spin arrays.*

## 5.1. INTRODUCTION

Industrial fabrication compatibility is a flagship argument for semiconductor spin qubits in gate-defined quantum dots as a candidate for large-scale quantum computation and simulation [2–6], but this promise can only be fully realized if the spin physics utilized to control qubits is also extensible. Currently, on-chip micromagnets have enabled state-of-the-art devices to exhibit powerful primitives including high-fidelity universal gate sets [7–9], high-fidelity initialization and readout of multiple qubits [10, 11], and coherent spin shuttling [8, 12].

The micromagnet typically serves two purposes. It produces a longitudinal gradient parallel to the quantization axes to give each spin a unique frequency and a transversal gradient that allows microwave electric fields to drive single-qubit gates via EDSR [13–15]. While this method of operation has been extended to 12 qubits [16], the linear charge-noise sweet spot of present magnet designs has motivated scaling in only one dimension. The limited connectivity and stringent fault tolerance thresholds of linear arrays imply that entering the second dimension is all but essential [17]. Although proposals exist for scaling EDSR control into two-dimensional arrays using on-chip magnets [18, 19], an experimental demonstration beyond 1D has, until now, been lacking.

Even in 1D arrays the dissipation of microwaves used for EDSR control is known to produce heating effects that complicate multi-qubit operation [20–23]. Typically, this manifests as qubit frequency shifts that are contextual upon the magnitude and duration of preceding microwave bursts. Circumventing this issue by working at warmer device temperatures is possible, but microwaves may be bypassed altogether. Whereas Singlet-Triplet (ST) and Exchange-Only (EO) encoded qubits allow for universal baseband control, aspects like state leakage and gate complexity have limited error rates to higher levels than for the single-spin encoding. Recently, single-hole spins in a 2D germanium array have been manipulated with high fidelity using baseband hopping control exploiting large differences in the quantization axis arising from dot-to-dot variations in the $g$-tensor [24, 25]. It is therefore intriguing whether such control can be engineered with on-chip magnets and, if so, what implications this poses for future architectures.

Here, we commission a 2x2 silicon quantum dot device for qubit control in two distinct regimes. First, we demonstrate that conventional micromagnet-based EDSR control of all four spins is possible in the 2D array, and we also demonstrate nearest-neighbour exchange control. We benchmark the performance of the four-qubit system with a particular emphasis on the crosstalk caused by off-resonant driving. Next, we lower the external magnetic field of the half-filled array to demonstrate qubit operation via hopping gates, whereby the tip in quantization axis is induced by the engineered magnetic stray field. We further analyse the

qubit coherence, fidelity, and crosstalk properties of the hopping gate. Finally, we propose how a repeated nanomagnet pattern can be used to engineer hopping control across an arbitrarily large 2D array, thereby illustrating how baseband control of single-electron spins in silicon may be a compelling control method for future devices.

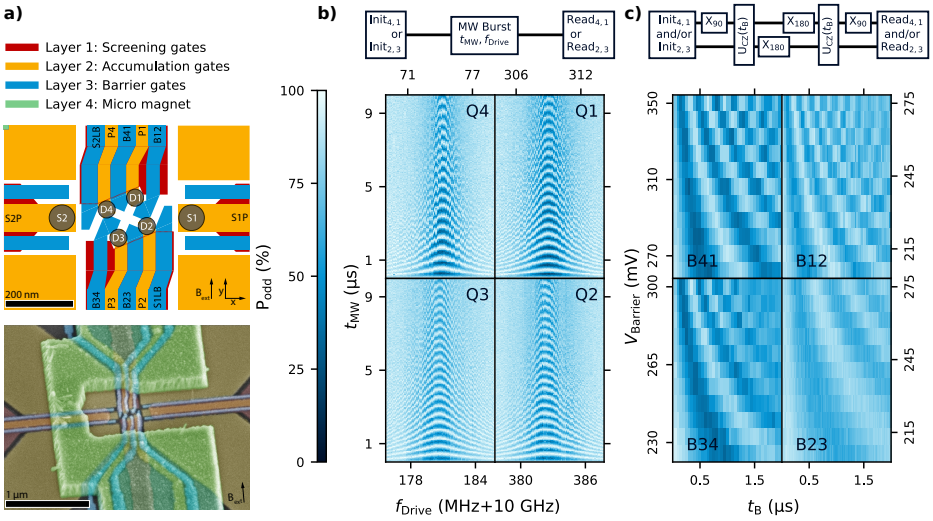


**Figure 5.1: A 2x2 Silicon Spin Qubit Array.** **a.** Design schematic and false coloured SEM image of a device nominally identical to the one measured. In the schematic, SET sensor positions are marked with S1 and S2, and the quantum dots are labelled clockwise with D1 through D4. We refer to each qubit as Q1 through Q4 according to the dot it primarily inhabits. The SEM image includes the micromagnet on top of the gate stack (not shown in the schematic). **b.** Odd parity probability after driving the qubit with a microwave burst as indicated by the block diagram. The respective Chevron patterns of all qubits are arranged according to their physical position. The drive power and modulation amplitude were adjusted per qubit to achieve a Rabi frequency around 2 MHz. **c.** Decoupled controlled phase oscillations of adjacent qubit pairs using the pulse sequence indicated in the block diagram. The Ising-like interaction $U_{CZ}$ is controlled by the voltage $V_{Barrier}$ on the barrier gate located between the respective plunger gates. We chose a static operating point such that the extrapolated exchange strength $J_{off} < 20$ kHz and apply a pulse on the barriers large enough such that $J_{on} > 1$ MHz. The large amplitudes for these barrier pulses as well as the particular fanout of gates B34, P3, and B23 often caused substantial degradation of the readout signal (see Section 5.6).

## 5.2. A 2x2 SILICON QUANTUM PROCESSOR BASED ON EDSR

The most straightforward progression from a one-dimensional silicon spin-qubit array to a two-dimensional array is the adoption of existing control strategies with only minor accommodations [10]. A 2x2 quantum dot array as shown in Fig. 5.1**a** was fabricated on a $^{28}$Si/SiGe heterostructure (residual nuclear spins of 800 ppm) and is used to accumulate four single electrons under each plunger gate as has been previously demonstrated in Chapter 4 [26]. After magnetizing the micromagnet at a field of 2 T along the positive y-axis as indicated in the SEM and schematic of Fig. 5.1**a**, the external field is reduced to 200 mT. We use PSB for initialization and measurement on the horizontal pairs ($Q_1Q_4$ and $Q_2Q_3$) along with EDSR to perform addressable single-qubit rotations. The 22.5° rotation of the 2x2 array combined with the longitudinal field gradient gives good spectral separation of the spins with a minimum frequency difference of 74 MHz. Using adequate parameters we find reasonable agreement with micromagnet simulations (see Extended Data Fig. 5.9 for details). The Rabi frequency of all four spins was tuned to 2 MHz to stay within the linear amplitude scaling regime (see Extended Data Fig. 5.2) to observe the Chevron patterns in Fig. 5.1**b**.

Despite the qubits not lying along the decoherence sweet axis of the micromagnet, we observe coherence metrics similar to [10]. The measured Ramsey decay times are $T_2^* = \{3.31(9), 2.03(2), 3.57(8), 2.90(5)\}$ µs for qubits $Q_1$ through $Q_4$ respectively with integration times of around 30 min. Similarly, we measured Hahn-echo decay times of $T_2^{\mathrm{H}} = \{30.21(24), 16.22(18), 40.38(21), 21.77(38)\}$ µs. Notably, the trend of coherence times is not strictly correlated to the designed decoherence gradients at each dot location (see Extended Data Fig. 5.9). There are three possible reasons for such discrepancies. First, the decoherence gradient is not isotropic in the plane of the quantum well, and the observed coherence times will depend on the microscopic orientation of the local charge noise fluctuators for each qubit. Second, large variations in coherence may occur for sufficiently sparse charge noise baths depending on the nature of the constituent fluctuators [27]. Third, hyperfine noise due to residual nuclear spins in the heterostructure may also contribute to decoherence that does not couple to the spins via the micromagnet gradient [28].

Two-qubit interactions are controlled using the barrier gates located between neighbouring plunger gate pairs to modulate the Ising-like exchange interaction. We observe the characteristic CPhase oscillations for all four nearest-neighbour pairs of qubits as a function of time and barrier pulse height as depicted in Fig. 5.1**c**. Although we operate at the symmetry point to minimize the sensitivity to charge noise,

the quality factor $T_2^{\mathrm{DCZ}}/t_{\mathrm{CZ}}$ of the oscillations for all pairs is limited to $Q_{2Q} = \{17(2), 7.5(7), 7.1(4), 12.2(7)\}$ for B12, B23, B34, and B41 respectively, which bounds the achievable two-qubit gate fidelities to modest values. Extended Data Fig. 5.8 shows state tomography results before and after applying a calibrated CZ gate for qubit pairs $Q_4Q_1$ and $Q_2Q_3$, highlighting the universal capability of this processor.

One reason for the suboptimal two-qubit performance may be the magnitude of pulses, ranging from 275 mV to 350 mV, required to achieve a satisfactory on/off exchange ratio as a result of the small barrier lever arms. Such large pulses jeopardize device stability and, in some cases, degrade readout visibility (see Fig. 5.1). Although we apply large pulse amplitudes, the maximum achievable exchange couplings of 1 MHz–4 MHz are small with respect to the dephasing times of the qubits.

Despite this shortcoming, we can still draw valuable insights about multi-qubit control with such an EDSR-based architecture. The quality factors $T_2^{\mathrm{Rabi}}/t_{180}$ of the four qubits are measured to be $Q_{1Q} = \{64(4), 67(6), 65(5), 64(7)\}$, and we estimate the resonant $X_{90}$ fidelity averaged across all four qubits to be 99.54(4)% using RB as displayed in Fig. 5.2**a**. By comparing the infidelity expected from both quasi-static qubit frequency fluctuations ($T_2^*$) and decoherence of the spins subject to driving ($T_2^{\mathrm{Rabi}}$), we conclude that it is the latter that predominantly limits the resonant single-qubit gate fidelity we observe from randomized benchmarking (see Supplementary Information Section 5.8.5 for details). It is possible that higher fidelities could be achieved by taking advantage of the higher possible Rabi frequencies on some of the qubits (see Extended Data Fig. 5.2). Having established a good single-qubit gate set for each qubit, we can probe the crosstalk such gates impart on neighbouring qubits. Controlling crosstalk is critical for multi-qubit operation, and while the absolute amount of crosstalk is relevant for calibration, its contextuality in time and number of gates is particularly indicative of how difficult this calibration becomes in practice. For EDSR, crosstalk commonly manifests as a spurious pulse-induced resonance shift (PIRS). We probe this “heating effect” on idling qubits using a modified Hahn echo sequence as depicted in Fig. 5.2**b** [21]. The sequence includes an off-resonant microwave burst that simulates the drive of another qubit, and we quantify the magnitude of this burst in relation to the average power required to perform single-qubit rotations across all four qubits in this device.

A nontrivial transient phase pickup is observed for all qubits for off-resonant bursts that are energetically comparable to those used for single-qubit gates. A particular instance is shown in Fig. 5.2**c**, though all qubits exhibit the same qualitative behaviour (see Extended Data). With increasing delay time and amplitude, more phase is picked up until an apparent saturation is reached. This transient response has been documented in previous studies [21]. However, when the

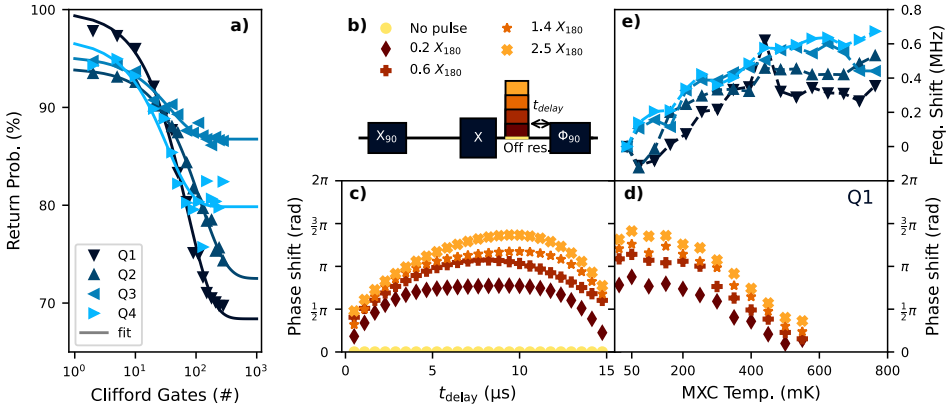


**Figure 5.2: EDSR Operation and PIRS Effects. a.** Return probability as function of the number of applied Clifford gates averaged over twenty different gate sequences for all four qubits. As each qubit readout has a different visibility, the curves decay to different values. The fitted Clifford gate fidelities are $F_{\text{Clif}}^{\text{res}} = \{99.28(5)\,\%, 99.58(4)\,\%, 98.7(2)\,\%, 98.5(3)\,\%\}$ for $Q_1$ through $Q_4$ respectively. The Clifford gate set is compiled using only $X_{\pm 90}$ and $Y_{\pm 90}$ primitive gates (see Methods), and the corresponding average physical gate fidelities are, respectively, $F_{\text{avg}}^{\text{res}} = \{99.67(2)\,\%, 99.80(2)\,\%, 99.39(8)\,\%, 99.31(15)\,\%\}$. **b.** Adapted Hahn Echo sequence to measure crosstalk effects as introduced in [21]. The off-resonant burst simulates the drive of a different qubit. By substituting the last $X_{90}$ with a $\Phi_{90} = X_{90}Z(\Phi)$ operation in the echo sequence and sweeping the phase $\Phi$, the relative phase pickup due to the off-resonant burst can be inferred. The transient behaviour is detected by varying the temporal position $t_{\text{delay}}$ of the off-resonant burst with respect to $\Phi_{90}$. **c.** Example of phase pickup as a function of $t_{\text{delay}}$ for $Q_1$ at 100 mK for different amplitudes of the off-resonant burst (see panel **b** for legend). We use a standard Hahn-echo sequence (yellow data points) as a reference to remove constant artifacts introduced by the echo pulse sequence. **d.** The maximum phase shift extracted from measurements as in panel **c** as a function of mixing chamber temperature for qubit $Q_1$ for four different off-resonance bursts (see panel **b** for legend). All qubits exhibit similar behaviour (see Extended Data Fig. 5.3). **e.** Temperature dependence of the bare qubit frequencies as measured by a Ramsey experiment relative to the frequency at base temperature. Symbols refer to different qubits as in panel **a**.

off-resonant burst occurs closer in time to the resonant echo pulse, less phase is picked up. The most likely origin of this counterintuitive behaviour is the transient heating caused by the resonant echo pulse:

the heating induced by the decoupling pulse reduces the transient effect of the off-resonant burst. The nonlinear combination of the two transients has severe consequences for crosstalk calibration: the required compensation will be sensitive to both pulse scheduling and amplitude.

It has previously been observed that pulse induced resonance shift (PIRS) is dependent on the temperature of the device [22]. To verify this, we repeat the above experiment on all qubits for different mixing chamber temperatures. From the fitted data (e.g. Fig. 5.2**c**) we extract and compare the maximum phase pickup as a function of temperature. Fig. 5.2**d** shows how increasing the mixing chamber temperature reduces the magnitude of the PIRS effect for Q1 (see Extended Data Fig. 5.3 for Q2-Q4). This substantial temperature increase, however, also has an impact on qubit coherence. Although the $T_2^*$ of all qubits is relatively unaffected by temperature, the $T_2^{\mathrm{H}}$ generally decreases monotonically as the mixing chamber temperature is raised (see Extended Data Fig. 5.5). Additionally, an increase in spin Larmor frequency as a function of temperature is observed for all quantum dots as seen in Fig. 5.2**e**.



While these results are qualitatively in agreement with a previous study of a six-spin array [22], there are three notable differences. First, the generally monotonic increase in frequency of all four qubits studied here contrasts with the previous measurement of a non-monotonic trend across the six-qubit array. Second, the heating effect is more moderate than the 1 MHz frequency shifts observed by Undseth et al. when using similar microwave bursts [22]. In this work, PIRS was observed through residual phase pick-up corresponding to a frequency shift on the order of 10 kHz–100 kHz. Last, the measured PIRS phase pickup is consistent with a *negative* Larmor frequency shift opposite to the frequency shift seen when raising the device temperature. This suggests that although the device temperature clearly plays a meaningful role in how PIRS manifests, the dissipated heat of the microwave burst may not be the only PIRS mechanism in this device. It has been proposed that thermally-sensitive environmental fluctuators can significantly contribute to the temperature dependence of the qubit frequencies [29]. Our observations underscore the difficulty of predicting and compensating multi-qubit crosstalk with resonant control.

## 5.3. BASEBAND OPERATION

In light of the crosstalk challenges arising from microwave control, the operation of spin qubits using exclusively baseband pulses makes for a compelling alternative while retaining the Loss-DiVincenzo qubit encoding. Such control was recently demonstrated by hopping a hole spin qubit between germanium quantum dots with different quantization

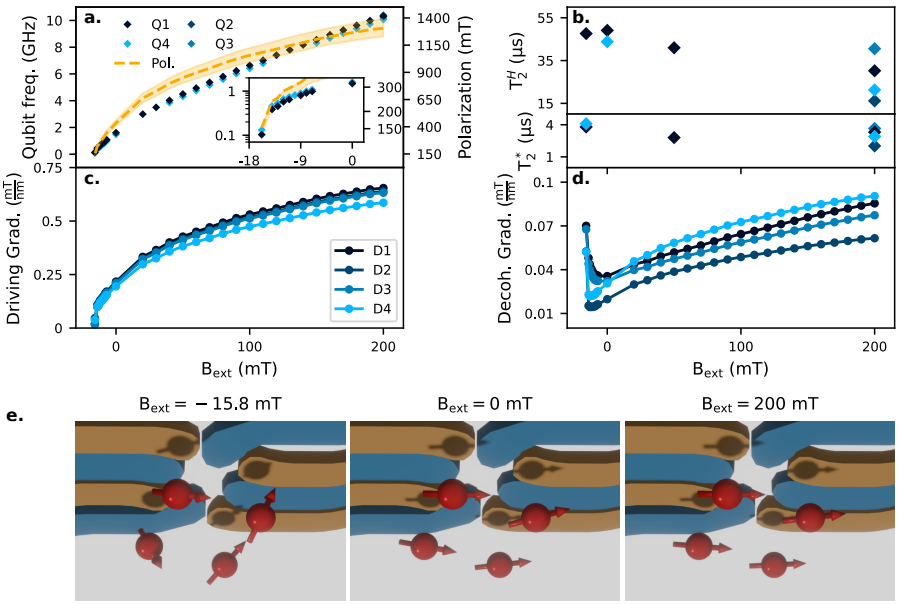


**Figure 5.3: Magnetic Field Dependence of Device and Qubit Properties.** **a.** Dependence of the qubit frequencies on the external magnetic field. Adiabatic inversion pulses are used for external fields above $B_{\text{ext}} = -15\,\text{mT}$ (qubit frequencies above 400 MHz) while Ramsey experiments with hopping control is used for lower fields. The dashed line shows the predicted homogeneous polarization of the micromagnet as extracted by fitting the measured qubit frequencies to a simplified micromagnet model (see Supplementary Information Section 5.8.2). The shaded area provides a generous estimate of uncertainty by displacing the micromagnet model ±15 nm out-of-plane and repeating the fits. The inset zooms in onto the behaviour below $B_{\text{ext}} = 0\,\text{mT}$ with the qubit frequencies and polarization plotted on a logarithmic scale. **b.** (lower) $T_2^*$ integrated for 30 minutes at various external field settings. Ramsey decay times are relatively unchanged by the magnitude of the external field and, consequently, the decoherence gradient. Symbols as in panel **a**. **b.** (upper) $T_2^{\text{H}}$ integrated for 30 minutes at various external field settings showing an inverse relation to external field and decoherence gradient. From the extracted micromagnet polarization in panel **a** we extract **c.** the driving gradient along the y-axis and **d.** the decoherence gradient magnitude at the centre of the plunger gates. The driving gradient decreases monotonically with decreasing external field while the decoherence gradient shows a sweet spot close to $B_{\text{ext}} = 0\,\text{mT}$. [cntd.]

**Figure 5.3: Magnetic Field Dependence of Device and Qubit Properties. e.** Renders of the plunger and barrier gates (yellow, blue) from below with the four electron spins (red, from left-to-right: Q3, Q2, Q4, Q1) for three different external field settings. The arrows indicate the quantization axes at the dot location which, approximating an isotropic $g$-factor of 2 in the silicon quantum well, is effectively assumed to be colinear with the total magnetic field vector. At $B_{\text{ext}} = 200\,\text{mT}$ the quantization axes are almost perfectly aligned with each other within a few degrees. At $B_{\text{ext}} = 0\,\text{mT}$, some deviation becomes evident. At $B_{\text{ext}} = -15.8\,\text{mT}$ the differences in quantization axes are very pronounced. Based on the micromagnet simulation, the tips are estimated to be between about 30° and 60° depending on the exact locations of the quantum dot in the micromagnet stray field.



axes [25] and bears resemblance to the strong-driving flopping mode regime proposed by [30]. Similarly, the 2x2 silicon array allows us to take advantage of quantization axis variation originating from the inhomogeneous magnetic field introduced by the micromagnet. However, even in the 2x2 array a large external field forces the spins' quantization axes to be nearly colinear. In order to accentuate the inhomogeneous magnetic field and limit Larmor frequencies for baseband control, the external field is reduced.

First, the micromagnet is magnetized in a 0.8 T external field. We populate the array with a single electron in dots 1 and 4, allowing us to keep PSB readout on the pair $Q_4Q_1$ while dots 2 and 3 remain empty. We track the qubit frequencies of $Q_1$ and $Q_4$ using adiabatic inversion pulses as the external field is reduced step-by-step as shown in Fig. 5.3**a**. We observe the qubit frequencies dropping both as a result of the lower external field as well as the demagnetization of the micromagnet. The polarization of the micromagnet is inferred by fitting the measured frequencies to a simplified magnet model where the magnetization is assumed to be homogeneous with no crystalline domains or shape anisotropy coming into consideration (see Supplementary Information Section 5.8.2). Even so, this model provides a firm basis for understanding the qualitative qubit properties across a wide range of external field settings.

Even at zero external field, the remanence of the micromagnet forces the quantization axes to be reasonably colinear and provides a driving gradient large enough for conventional EDSR operation. Notably, the Hahn-echo coherence times of $Q_1$ and $Q_4$ nearly double from 30.2 µs and 21.3 µs to 49.1 µs and 43.8 µs respectively as shown in Fig. 5.3**b**. Curiously, the $T_2^*$ coherence times do not change significantly with the magnetic field and decoherence gradient. This suggests the limiting low-frequency noise may be different than the noise inducing

Hahn-echo decay. The amplitude with which these spins are driven with $f_{\mathrm{Rabi}} \approx 2\,\mathrm{MHz}$ also increases by about a factor of 3. These observations are compatible with the estimated change in decoherence and driving gradients at the dot locations: Fig. 5.3**c** shows that the decoherence gradient permitting charge noise to couple to the spins has approximately halved while Fig. 5.3**d** shows the driving gradient has been reduced by a factor of 3. As predicted by simulations, the 100 MHz frequency separation between $Q_1$ and $Q_4$ is retained and becomes the main contribution to the decoherence gradient. This suggests that EDSR operation in the absence of an external solenoid, a mundane but material obstacle for the near-term scalability of semiconductor spin qubits, is a realistic possibility.

Decreasing the external field further, we reach a regime where the local magnetic field in the dot region is increasingly inhomogeneous owing to the competition between the remaining micromagnet polarization and the opposed external field. The spin quantisation axes at the quantum dots will no longer align but instead point in different directions. This is most clearly illustrated by rendering the quantization axes at each dot location as shown in Fig. 5.3**e**. Despite the extreme inhomogeneity and low effective polarization of the micromagnet, we observe no pronounced instability of the spin frequencies. On the contrary, the measured Ramsey and Hahn-echo decay times universally improve upon the coherence measured at $B_{\mathrm{ext}} = 200\,\mathrm{mT}$ with EDSR control (Fig. 5.3**b**). However, at a nominal external field setting of $B_{\mathrm{ext}} = -15.8\,\mathrm{mT}$ the driving gradient is too small for resonant control. Fortunately, the large quantization axis tips enable coherent control by hopping the electrons from dots $D_1$ and $D_4$ to the vacant dots $D_2$ and $D_3$. Furthermore, the $Q_1$ and $Q_4$ Larmor frequencies of 131 MHz and 103 MHz, respectively, are practical for AWG control.

Fig. 5.4**a** illustrates the pulse sequence required for a hopping gate between dots $D_1$ and $D_2$. During each ramp, the charge transfer between dots should be adiabatic (see Fig. 5.4**b**), hence a sufficiently large tunnel coupling $t_c$ should be maintained between dots. A fast detuning ramp $v = \epsilon/t_{\mathrm{ramp}}$ is desirable to minimize dephasing while the spin is most strongly hybridized with the charge at $\epsilon = 0\,\mu\mathrm{eV}$. Within the subspace of the adiabatic charge transition, the spin state transfer should be diabatic (see Fig. 5.4**c**) which is ensured by traversing the Hamiltonian "step" sufficiently fast. Provided these conditions are met (see Supplementary Information Section 5.8.6), a universal gate set may be calibrated with the appropriate choice of parameters $t_1$, $t_2$, and $t_{\mathrm{add}}$ [25]. One repetition of two cycles as drawn is sufficient to calibrate an $X_{90}$ provided the quantization axis tip between dots lies between 22.5° and 157.5°. For quantization axis tips between 45° and 135°, one repetition of a single cycle suffices. The additional idling time parameter $t_{add}$ between subsequent repetitions ensures the axis of rotation is

consistent when concatenating multiple $X_{90}$ gates.

To quantify the quantization axis tip experimentally, we apply multiple repetitions of spin hopping for varying times $t_1$ and $t_2$ and measure the resulting spin fraction. For the presented data the ramp time between $t_1$ and $t_2$ was set to be 2 ns. This is comparable to the minimum rise time of the AWG output signal and was chosen to minimize decoherence during the shuttling process. The tunnel coupling was estimated to be roughly 48 µeV for all hopping gate experiments unless otherwise noted (see Extended Data Fig. 5.7). The measured pattern sensitively depends on the tip angle and may be fit numerically to the expected unitary evolution of the spin (see Methods). An example of a 2-cycle-4-repetition-protocol measurement and fit is shown in Fig 5.4**d** and yields a tip angle of $\theta_{1,2} = 37.3(2)^\circ$. Similarly, we measure $\theta_{4,3} = 47.5(2)^\circ$ (see Extended Data Fig. 5.6). In the latter case, we observe that pulsing on P3 causes severe degradation to the readout signal (as was also the case for probing two-qubit interactions in Fig 5.1). We therefore opt to only benchmark the $Q_1$ hopping gate.



To coarsely calibrate the $t_1$, $t_2$ and $t_{\text{add}}$ idling times for a high-fidelity single-qubit gate, we select parameters where the $X_{90}$ fidelity is theoretically maximized as shown in Fig. 5.4**d**. We then fine tune the parameters by running a sequence of $X_{90}$ gates and select the precession times that produce a periodicity of 4 as exemplified for $t_1$ in Fig. 5.4**e**. Consequently, we observe discretized Rabi oscillations of around 5 MHz. By padding idling times with $2\pi$ rotations, we intentionally do not operate the gates as fast as is theoretically possible in order to minimize artifacts that occur at the limit of the AWG time resolution. Z-rotations are implemented with a physical wait time calibrated by a Ramsey measurement of the spin Larmor frequency. Constructing a Clifford gate set comprised of $X_{90}$ hopping gates and physical Z-rotations, single-qubit randomized benchmarking of $Q_1$ yields an average Clifford gate fidelity of about $F^{\text{hop}}_{\text{Clif,odd}} = 99.01(11)\,\%$ and $F^{\text{hop}}_{\text{Clif,even}} = 99.49(7)\,\%$ as shown in Fig. 5.4**f**. By attributing all errors to the $X_{90}$ hopping gate we can provide a lower bound on its fidelity $F^{\text{hop}}_{X_{90}} = 99.50(6)\%$ (see Methods). This is directly comparable to the physical resonant gate fidelities achieved with EDSR control at high field. Using blind randomized benchmarking, we estimate that the hopping gate fidelity is bounded by the tunnel coupling tunability in this device leading to non-adiabatic charge shuttling and state leakage (see Supplementary Information Section 5.8.6 and Section 5.8.7 for further discussion) [31]. When applied to the data of Fig. 5.4**f**, we obtain a leakage rate of 0.13(5) % and a corresponding Clifford gate fidelity of 99.26(5) %.

We may also compare the performance of the EDSR and hopping mechanisms with regards to crosstalk (Fig. 5.4**g**). We employ the same

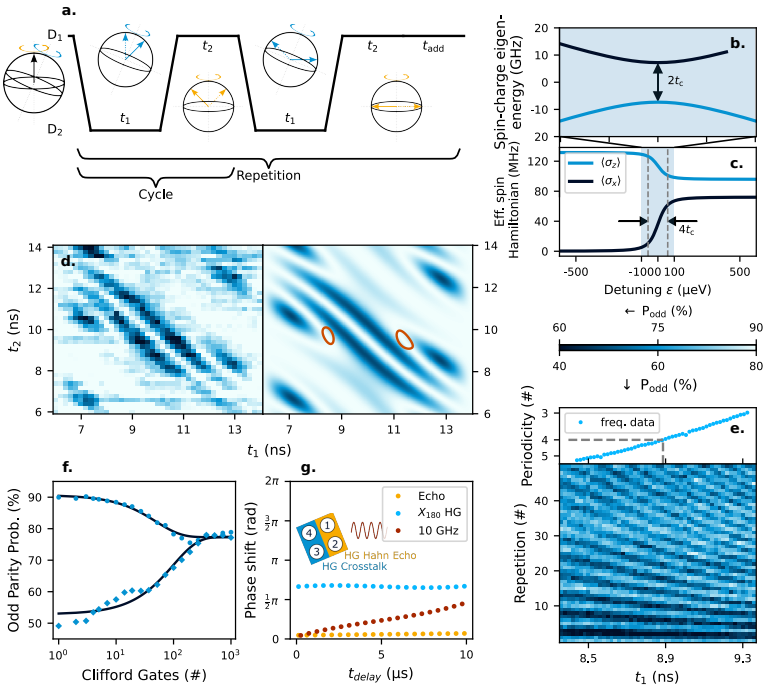


**Figure 5.4: Implementation and Characterization of a Hopping Gate. a.** Hopping sequence and sketched evolution of the spin state vector at each step. The dashed (solid) arrow indicates the initial (final) vector at each step while yellow (blue) correspond to the original (secondary) quantum dot. The sequence results in a 90 degree rotation around the x-axis in $D_1$. **b.** Spin-charge energy level diagram for the $D_{1,2}$ double-dot system illustrating the charge avoided-crossing. The spin-splitting is too small to resolve compared to the much larger energy scale of the tunnel coupling. **c.** Components of the effective spin qubit Hamiltonian $H'$ with respect to the quantization axis of $D_1$ in the subspace of the charge ground state given by $\langle\sigma_i\rangle = \mathrm{Tr}(\sigma_i H')$ for the $D_{1,2}$ double-dot system (see Supplementary Information Section 5.8.6). **d.** Experimental (left) and fitted (right) odd-parity probability using two cycles and four repetitions [refer to **a**] while sweeping $t_1$ and $t_2$ for the $D_{1,2}$ double-dot system with $t_{add}$ fixed to 3.6 ns. The quantization axis tip is fit to 37.3(2)° with a unitary model (see Methods for details). A precise combination of $t_1$, $t_2$ and $t_{add}$ will create an accurate $X_{90}$. The red regions highlight the $t_1$ and $t_2$ where each one of the four repetitions achieves a high fidelity $X_{90}$ gate. The tunnel coupling for this measurement was estimated to be roughly 18 μeV. Additional data, fits and fidelity contours for one, two, and four repetitions of qubits $Q_1$ and $Q_4$ are shown in Extended Data Fig. 5.6. [cntd.]

**Figure 5.4: Implementation and Characterization of a Hopping Gate. e.** Fine calibration of $t_1$ by repeating the roughly calibrated gate many times with minor adjustments to one of the timing parameters. We extract the periodicity of the pattern and select the $t_1$ that matches a periodicity of 4 for the benchmarked gate. The difference in $t_1$ with respect to the experimental data in **c** is due to adjustments in $t_{\text{add}}$. **f.** Randomized benchmarking using both initial basis states. The Clifford set is compiled using only $X_{90}$ hopping gates and physical Z-rotations (see Methods). The fitted Clifford gate fidelities are $F_{\text{Clif}}^{\text{hop,odd}} = 99.01(11)\,\%$ and $F_{\text{Clif}}^{\text{hop,even}} = 99.49(7)\,\%$ for the odd and even parity inputs respectively (see Methods). **g.** PIRS-like measurements showing the phase accumulation of a hopping gate and a 10 GHz burst when included in an echo sequence as depicted in Fig 5.2 **b**. The hopping gate is implemented as an $X_{180}$ gate on $Q_4$. The microwave burst carries the same energy as an average $X_{90}$ gate in this device during conventional EDSR operation.



PIRS methodology as in Fig. 5.2 and perform a Hahn echo sequence on qubit $Q_1$ using hopping gates. As $Q_4$ is used for parity readout, we calibrate an $X_{180}$ hopping gate on this qubit and embed it within the echo sequence (in place of the off-resonant burst) to measure the resulting phase pickup from the physical shuttling. In contrast to the EDSR-based gates, the hopping mechanism imparts a constant phase pick-up regardless of its temporal position in the echo sequence. We attribute this shift to the change in electrostatic conditions caused by both the gate voltage pulses and movement of the $Q_4$ electron in the quantum well which shifts the position of $Q_1$ in the magnetic field gradient. The qubit pair is maintained with very little residual exchange, hence negligible conditional phase is acquired during the sequence.

We also introduce a 10 GHz burst commensurate with an $X_{90}$ gate in the standard EDSR regime. We observe a transient phase pickup analogous to the experiments executed at high-field. Notably, the nonlinear "masking" due to the resonant echo pulse is not observed here as the decoupling is performed with a hopping gate. The total transient phase pickup due to PIRS is reduced compared to Fig. 5.2. This is likely a consequence of the low magnetic field environment, as either a $g$-factor change or electron displacement in the gradient will result in a smaller shift in qubit Larmor frequency. In any case, the shuttling gate avoids the transient effect of the microwave burst, and the magnitude of the effect would decrease as the distance between local operations is increased, making a low-field shuttling implementation of single-qubit gates an appealing approach to reduce crosstalk and improve multi-qubit control.

## 5.4. ARCHITECTURE PROPOSAL

The design of on-chip magnets for EDSR control of extensible 2D spin arrays presents a design challenge: engineering controllability and spectral addressability with a small pitch requires nanoscale magnetic variation. With magnets or current-carrying wires that are an order-of-magnitude larger than the quantum dots themselves, this is difficult to achieve. Proposals making use of nanomagnets, with features similar in size to a $\approx 100\,\text{nm}$ dot pitch, are a promising solution [18, 19, 32–35].

Inspired by these ideas, nanomagnets may also be used for hopping control. Compared to the microscopic $g$-tensor variations in germanium quantum dot arrays and similar platforms, local magnetic field variations could be engineered more deterministically. It is therefore worthwhile to revisit the design requirements for on-chip nanomagnets with hopping control in mind. Two specifications stand out compared to EDSR. First, qubit addressability with hopping gates is more localized and does not rely on the spectral separation of qubit frequencies. Second, the transverse gradient required for EDSR control effectively mandates a total magnetic field magnitude on the order of tens of mT, whereas tips in the quantization axis for hopping control (i.e. inhomogeneity of the magnetic field vector) are possible at more modest magnetic fields as illustrated by this work.



Exploiting these features of hopping control, we propose a periodic nanomagnet design as depicted in Fig. 5.5**a**. After applying an external magnetic field along the y-axis, the shape anisotropy imposed by the $40\,\text{nm} \times 120\,\text{nm} \times 50\,\text{nm}$ iron magnet geometry causes the magnetization to persist even at ambient conditions [32]. The relaxed magnetization, simulated by the OOMMF software package [36] (see Supplementary Information Section 5.8.3), generates an inhomogeneous magnetic field that enables hopping conditions in a quantum well situated about 100 nm below the magnetic layer. Owing to the inhomogeneous magnetic vector field, a predictable pattern of quantization axis tips (relative to a fixed reference point) of around 90° occurs with a periodicity of 200 nm as shown in Fig. 5.5**b**. Fig. 5.5**c** shows this smoothly-varying tip along two shuttling axes in which hopping gates may be implemented between adjacent sites with a pitch of about 100 nm.

A sparse 2D array of silicon quantum dots may therefore be populated with flexible occupancy to realize different spin connectivity within the magnetic landscape. Fig. 5.5**d** (upper) illustrates an instance where many dots may be left vacant to facilitate not only hopping gates but also shuttling to peripheral sensing regions or to implement two-qubit gates between distant spins. Fig. 5.5**d** (lower) depicts a denser array where all qubits still have access to single-qubit logic via hopping. As any quantization axis tip between 45° and 135° allows Hadamard gates to be performed with a single shuttling cycle, this architecture is robust to some variation in both the placement/shape of the magnets and

formation of the dots. As the nanomagnets can be fabricated over a large area, edge effects are relegated far beyond the extent of any finite quantum dot array. Of course, such a periodic array would also have to grapple with gate patterning and fanout as any other dense 2D array of dots would, but the issue of qubit controllability would not compound the difficulties. Provided such a fanout can accommodate the sparse magnetic layer, the design space for potential architectures becomes very large.

The nanomagnet array presented here confers two additional benefits beyond enabling hopping control that can also be leveraged in other potential designs. First, the qubit frequencies are distributed in a range below 400 MHz without any applied external field. This removes the need for a solenoid in the cryogenic setup provided the magnets can be polarized at room temperature. Second, a periodic pattern of decoherence sweet spots also emerges to form a natural template upon which to place idling spins as seen in Fig. 5.5**e**. The proposed shuttling channels plotted in Fig. 5.5**f** show that even the maximum decoherence gradient encountered in the quantum well is not substantially larger than typical EDSR addressability gradients that range from 0.05 mT/nm to 0.1 mT/nm. We note that different combinations of ferromagnetic materials and nanomagnet geometries may be used to achieve similar outcomes.

The hopping approach is not without drawbacks. High fidelity hopping control requires voltage pulses with very precise timing on the order of tens of picoseconds and mandates working with physical phase gates as opposed to virtualized phase tracking in a rotating frame. In the case of silicon, the microscopic valley degree of freedom may interfere with charge shuttling in cases where the valley phase difference between dots modifies the effective tunnel coupling[30, 37–39]. Also, the nanomagnets compete for space with the fanout of the gate electrodes that define the dots. Beyond engineering for single-qubit control, considering Zeeman energy differences for high-fidelity two-qubit gates [40] and Pauli spin blockade readout [11] would be necessary to demonstrate a viable architecture. Engineering locations with zero magnetic field could also be useful for parking spins to alleviate the task of phase-tracking while idling qubits. Although we do not anticipate anything inhibiting these features with nanomagnet designs, we leave their details for future studies.

## 5.5. CONCLUSION

We have used a 2x2 $^{28}$Si/SiGe quantum dot device to explore two ways in which future 2D arrays of single-electron spins in silicon may be controlled. Using microwave driving and barrier gate voltage pulses, we demonstrated universal control over a four-qubit system using

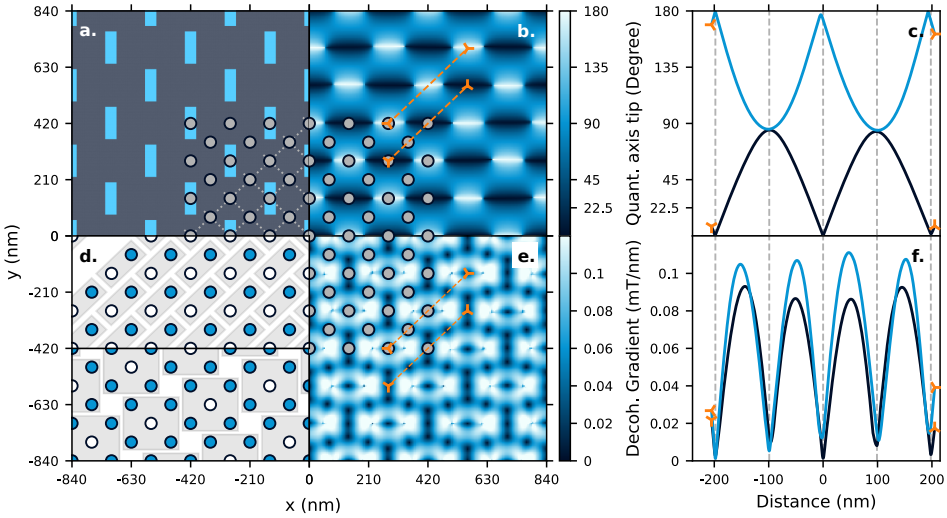


**Figure 5.5: Nanomagnet Based Tileable Architecture Utilizing Hopping Gates.** **a.** Zoomed in section of the proposed nanomagnet pattern with the magnetic material shown in bright blue. Each iron nanomagnet is 40 nm × 120 nm in area and 50 nm in out-of-plane height. In the lower right corner we show the envisioned quantum dot positions and their connectivity. These patterns extend across the contiguous panels **a**, **b**, **d** and **e** and pertain to the data contained within them. **b.** The relative change in quantization axis, assuming an isotropic *g*-factor, with respect to the central dot of the panel. The quantum well is located 100 nm below the bottom surface of the nanomagnet layer. The magnetic field is computed at zero external magnetic field after having allowed the nanomagnet magnetization to relax according to their shape anisotropy and material properties. **c.** Line cuts corresponding to the orange markings in panel **b** illustrating the relative change in quantization axis tips along two potential hopping axes. The observed asymmetries are a consequence of the finite mesh size used for simulation and interpolation artifacts. The grey dashed lines indicate the quantum dot positions. **d.** Versatile filling of the quantum dot array: the bright blue filled dots indicate a quantum dot with an electron, the white markers indicate an empty quantum dot. The upper section shows a 50% filling, the lower section a denser filling with 80% occupancy. The grey shaded areas indicate the repeated unit cell. **e.** The calculated decoherence gradient resulting from the nanomagnet stray field as described in **b**. **f.** Line cuts corresponding to the orange markings in panel **e** illustrating the decoherence gradient along two potential hopping axes. Minor artifacts from the finite mesh size and field interpolation are visible.

conventional strategies from 1D arrays with only mild alterations. The performance was primarily limited by poor exchange control owing to the weak tunability of nearest-neighbour tunnel couplings. One potential remedy would be to modify the geometry of the barriers and invert the gate layers in fabrication to increase the lever arm controlling exchange. Another possibility would be the inclusion of a central gate to facilitate the decoupling of spins without requiring such large pulse amplitudes. Regardless, this demonstration of a 2D silicon spin array shows that established qubit control methods are sufficient for scaling beyond linear architectures. Longer bilinear arrays and perhaps trilinear devices ought to be compatible with established micromagnet designs. However, we also found that resonant single-qubit control causes crosstalk that complicates multi-qubit operation.

By opposing the polarization of the micromagnet with the external field to create a net vector field that varies over the scale of the array, we implement hopping gates that allow for baseband control of single spin qubits. Our initial characterization indicates several advantages of this operating regime. First, the baseband control pulses do not impart the transient phase crosstalk that was observed with resonant control. This may be attributed to the reduced power dissipation per logical operation which in turn reduces local heating effects [25]. Second, the reduced magnetic field reduces the coupling strength to charge noise thus increasing the Hahn echo coherence substantially. Whereas the device was not optimized for hopping gate operation, we already demonstrate a hopping gate that is competitive with the EDSR control demonstrated in this device both in terms of speed and fidelity. We believe the same aforementioned improvements in tunnel coupling control would permit better fidelities in future implementations, and the gate speed would effectively double by increasing the tip of the quantization axis between dots to above 45°.

Finally, we explore how engineering on-chip magnets for hopping spins alleviates many of the challenges that impede scaling EDSR control. We put forward an illustrative example of a periodic nanomagnet pattern that creates a deterministic pattern of decoherence sweet spots and nearest-neighbour tip angles for implementing hopping spins in an arbitrarily large 2D array. These conditions can further enhance coherence times, increase the single-qubit gate speed, and do not require a superconducting solenoid to provide an external field. We believe further investigation into nanomagnet designs for hopping spin control would be very fruitful.

## 5.6. METHODS

### 5.6.1. DEVICE DESIGN AND FABRICATION

The device layout used in this work is similar to the ones used in our previous work [26]. The heterostructure comprises a $Si_{0.69}Ge_{0.31}$ strained relaxed buffer (SRB), a 7 nm tensile-strained $^{28}Si$ quantum well (isotopic enrichment 800ppm), and a 30 nm $Si_{0.69}Ge_{0.31}$ barrier passivated by an amorphous Si-rich layer [41]. Substantial noise from the magnet power supply in driven mode prevented a reliable magnetospectroscopic measurement of the valley splittings in this device. The average valley splittings of 240 µeV measured in [41] are representative of what we would expect in this device, though it is possible that local microscopic disorder may yield outliers for particular quantum dots.

On top of the heterostructure we fabricate a multilayer gate stack isolated by a native SiOx layer and a 10 nm thick layer of AlOx deposited using atomic layer deposition (ALD). The first metallic layer (3:17 nm Ti:Pd) connects to the ohmic contacts and defines screening gates. The screening gates define the area that will host the four quantum dots and two SETs and prevent electron accumulation or spurious dot formation in the fanout. Furthermore, the screening gates confining the 2x2 array are designed as coplanar waveguides to effectively deliver microwave signals for EDSR control. The second layer (3:27 nm Ti:Pd) includes all plunger and accumulation gates, while the third layer (3:27 nm Ti:Pd) contains all barrier gates. The top layer of the gate stack (3:200 nm Ti:Co) contains only the micromagnet. Each layer is electrically isolated from the ones before by 5 nm $AlO_X$ grown with ALD.

The SETs are measured using RF reflectometry implemented using the split-gate approach [42]. The size of the accumulation gates was substantially increased compared to [26] to increase the capacitance to the 2DEG. The split accumulation gate could be depleted to create a high-resistance path from the 2DEG to the ohmic to prevent signal leakage.

The fanout of the barrier and plunger gates is shown in Extended Data Fig. 5.1. The starred connections indicate the bond pads corresponding to B43, P3 and B23 which have uniquely circuitous traces to adapt to the distribution of fast-lines on the sample PCB. We consistently observe readout degradation on a timescale at least as long as a 10 µs single-shot measurement when applying baseband pulses to these gates. As the cross-capacitance between these traces and adjacent bondpads (many of which connect to unvirtualized gates) is much larger in the fan out than at the scale of the quantum dot array, we suspect their suboptimal routing is correlated with the drop in readout quality and that these problems can be alleviated in future designs.

### 5.6.2. INITIALIZATION, CONTROL, AND READOUT

A single-shot measurement includes initialization, manipulation and readout. Initialization and readout are performed using Pauli spin blockade and post-selection similar to [10]. While PSB could be achieved in 4 qubit pairs in this device, we focus on pairs (4,1) and (2,3) as they offered superior performance. All shots begin with a round of parity-mode PSB measurement where parallel spin states are blockaded in the (1,1) charge state and antiparallel spin states are permitted to tunnel to the doubly-occupied singlet state S(2,0). A fast diabatic ramp is used to pulse from the readout point to the (1,1) charge state. When the post-selected initial state is S(2,0), the fast ramp yields a mostly-entangled state (see Extended Data Fig. 5.8) with consistently higher single-qubit visibility than what is obtained with an adiabatic ramp to the (1,1) charge state. Prior to measurement, a wait-time of 1 µs to 5 µs is included to permit both antiparallel spin states to decay to the S(2,0) state. The charge sensor signal is integrated for 1 µs to 20 µs. Some datasets are post-processed to shift the readout threshold to an optimal point.



While a longer integration time improves readout quality somewhat, there appear to be other fundamental limits to the qubit visibilities we can achieve. One factor is the limited tunnel coupling tunability in this particular device upon which the PSB mechanism depends very sensitively. At the high-field operating condition, the spins' quantization axes are estimated to be aligned within a few degrees. However, at low-field operation the expected tip between quantization axes in the PSB pair is estimated to be about 20 degrees. This causes an opening of the S(2,0)-$|\downarrow\downarrow\rangle$ avoided crossing which may impede a linear adiabatic ramp from the S(2,0) state to the $|\downarrow\uparrow\rangle$ for high-fidelity initialization. Pulse-shaping and active feedback may be used to mitigate this, but these were not investigated in this work. Alternatively, an adiabatic ramp through a sizeable S(2,0)-$|\downarrow\downarrow\rangle$ avoided crossing may permit initialization directly into the $|\downarrow\downarrow\rangle$ state as is often done with hole spin qubits. In the future, spin qubit designs could make use of separate zones for readout and control, which are individually optimized by local nanomagnets, for example.

Qubit manipulation includes resonant drive and diabatic spin shuttling for single-qubit gates. The Hamiltonian for the single-qubit gates are discussed in Supplementary Information Section 5.8.1 and Section 5.8.6 respectively. All microwave pulses are padded with 5 ns wait times to allow for a transient ring-down of the microwave source. Furthermore, the IQ amplitudes and phases are adjusted for each qubit at its centre-frequency to suppress LO-leakage, unwanted sidebands and other spurious tones during IQ modulation. In all cases, a square pulse shape is used for the I and Q waveforms.

The exchange interaction, given by $H_{\text{exch}} = 2\pi\hbar J\mathbf{S}\cdot\mathbf{S}$, is turned

on and off via square barrier pulses for the DCZ oscillations shown in Fig. 5.1**c**. Due to the large Zeeman energy difference present between all qubit pairs, we take the two-qubit unitary evolution to be $U_{CZ}(t) = \mathrm{diag}(1, \exp(i\pi Jt), \exp(i\pi Jt), 1)$.

The presented single- and two-qubit experiments were run at a wide variety of temperatures and fields. The chevron patterns in Fig. 5.1**b** and the randomized benchmarking in Fig. 5.4 **a** were run at 250 mK and 200 mT to prevent heating effects. The decoupled CZ oscillations were measured at the same field but at base temperature (around 20 mK). All external field sweeps and shuttling gate experiments were conducted at base temperature.

### 5.6.3. RANDOMIZED BENCHMARKING

In this work, we benchmark single-qubit gates implemented via resonant control and hopping control. Here we discuss the implementation of the Clifford gate sets in greater detail to interpret the average gate fidelities that are extracted for both gate flavors. For standard randomized benchmarking, we extract fidelities by fitting the decay curve to:

$$y(N) = A + B(1-p)^N, \tag{5.1}$$

where $N$ is the number of Clifford gates in the RB sequence, and $A$, $B$, and $p$ are fitting parameters. The estimated Clifford gate fidelity is then estimated as $1 - p/2$. The reported error bars correspond to the standard deviations acquired from curve fitting.

When using resonant control, the X/Y compilation is used (see Table II of [43]) whereby all Clifford gates are compiled into ±90 degree rotations about the X and Y axes of the Bloch sphere. A single microwave burst operation is calibrated: it has a constant amplitude, frequency, duration, and a post-burst padding of 5 ns to allow for the microwave source to ring down. The only difference between pulses is the relative phase with which the I and Q modulation channels begin. For a given sequence of Clifford operations, the error contributed by each physical gate should be nominally identical in the absence of any non-Markovian effects. As the X/Y compilation of the 24 Cliffords contains 52 primitive gates in total, the average resonant gate fidelity $F^{\mathrm{res}}_{\mathrm{avg}}$ from the set $\{X_{\pm 90}, Y_{\pm 90}\}$ is estimated to relate to the resonant Clifford gate fidelity $F^{\mathrm{res}}_{\mathrm{Clif}}$ as $F^{\mathrm{res}}_{\mathrm{avg}} = 1 - (1 - F^{\mathrm{res}}_{\mathrm{Clif}}) \cdot \frac{24}{52}$. For $Q_1$ to $Q_4$ respectively, the Clifford gate fidelities are measured to be $F^{\mathrm{res}}_{\mathrm{Clif}} = \{99.28(5)\,\%, 99.58(4)\,\%, 98.7(2)\,\%, 98.5(3)\,\%\}$. We use 20 random Clifford circuits per data point, and average the result of about 1200 post-selected single shot measurements per circuit. The corresponding average resonant gate fidelities are, respectively, $F^{\mathrm{res}}_{\mathrm{avg}} = \{99.67(2)\,\%, 99.80(2)\,\%, 99.39(8)\,\%, 99.3(2)\,\%\}$.

When using hopping control, the X/Z compilation is used (see again Table II of [43]) as the gate set is comprised of a unique $X_{90}$ hopping operation as well as Z rotations implemented with physical idling times. Negative rotation about the X axis is implemented by a $Z_{180}$ prior to a $X_{90}$ hopping gate. In contrast to the resonant gate compilation, the X and Z operations are of a fundamentally different nature and therefore contribute to the error rate in distinct ways. First, $X_{90}$ operations require more time than Z rotations and therefore pick up more error through dephasing. Second, $X_{90}$ operations require four precise intervals of Larmor precession whereas Z rotations require only one. This means that any uncorrelated jitter in the AWG ramps will cause more error in the $X_{90}$ operations. Third, as $X_{90}$ operations involve shuttling, errors may arise due to imperfect charge or spin transfer between dots. Therefore, $X_{90}$ gates should be more prone to error than any Z rotation.

Interleaved randomized benchmarking data was not taken to directly estimate individual gate fidelities, so we propose two ways of interpreting the fidelity of the individual physical operations. From randomized benchmarking, we obtain a Clifford gate fidelity $F^{\text{hop}}_{\text{Clif}}$. We use 250 random Clifford circuits per data point, and average the result of about 1500 (200 circuits) and 750 (50 circuits) post-selected single- shot measurements per circuit. The X/Z Clifford set is compiled from 89 physical gates in the set $\{X_{\pm 90}, Z_{\pm 90}, Z_{180}\}$, so one may estimate the average gate fidelity of this set as $F^{\text{hop}}_{\text{avg}} = 1-(1-F^{\text{hop}}_{\text{Clif}})\cdot\frac{24}{89}$. Alternatively, one may estimate a lower bound of the $X_{90}$ gate fidelity by attributing all of the error to the $X_{90}$ operations on the basis that all Z operations are effectively brief extensions to the preceding $X_{90}$ sequence. As each Clifford gate in the X/Z compilation contains exactly 2 $X_{90}$ gates, the $X_{90}$ fidelity may be bounded as $F^{\text{hop}}_{X_{90}} = 1-(1-F^{\text{hop}}_{\text{Clif}})\cdot\frac{1}{2}$. We run standard randomized benchmarking of the baseband gate set after initializing both in the odd and even parity states as shown in Fig. 5.4(f). While both exponential trends decay to the same mixed state probability, the even parity branch contains a small oscillatory artifact that persists even with substantial averaging. While readout crosstalk or state leakage during the protocol may play a role, we are unsure of the true origin of this artifact. To be conservative in our evaluation of the X90 hopping gate quality, we extract the Clifford gate fidelity of $F^{\text{hop}}_{\text{Clif,odd}} = 99.01(11)\%$ for $Q_1$ from the odd parity decay. It follows that $F^{\text{hop}}_{\text{avg,odd}} = 99.73(3)\%$ and $F^{\text{hop}}_{X_{90},\text{odd}} = 99.50(6)\%$. This latter value is the estimated fidelity bound reported in the abstract. For the even parity branch we fit $F^{\text{hop}}_{\text{Clif,even}} = 99.49(7)\%$, $F^{\text{hop}}_{\text{avg,even}} = 99.86(2)\%$ and $F^{\text{hop}}_{X_{90},\text{even}} = 99.74(4)\%$. The even parity branch contains a small oscillatory artifact that persists even with substantial averaging, and we are unsure of the origin of this artifact.

To gain insight about possible state leakage during hopping operation, we also employ the fitting method of blind randomized benchmarking (blind RB) [31]. Blind RB was developed to estimate the influence of leakage on the operation fidelity within an encoded subspace. We can use a similar interpretation here to estimate the role of leakage for the hopping gate. Blind RB makes use of two separate RB decay curves: one, $y_0(N)$, where the inverting Clifford is calculated to return the qubit to the initial state, and another, $y_1(N)$, where the inverting Clifford is modified to result in a net qubit-flip. Our implementation is imperfect in the sense that the even-parity decay curve was prepared with a physical $X_{180}$ gate that introduces additional SPAM errors compared to the odd-parity decay curve, but this effect should be small. The two RB curves can be fit to the following system of equations:

$$y_0(N) = A + B(1-p)^N + C(1-q)^N \tag{5.2}$$

$$y_1(N) = A - B(1-p)^N + C(1-q)^N, \tag{5.3}$$



where $N$ is the number of Clifford gates in the RB sequence, and $A$, $B$, $C$, $p$, and $q$ are fitting parameters. The estimated SPAM-normalized leakage rate per Clifford operation is estimated as:

$$\Gamma = -Cq/B, \tag{5.4}$$

the total SPAM-normalized error rate per Clifford operation is estimated as:

$$\epsilon = p/2 - Cq/2B, \tag{5.5}$$

and the error rate within the qubit subspace is inferred to be $\epsilon_q = \epsilon - \Gamma$ (see [31] for derivations). For the hopping gate benchmarking data shown in Fig. 5.4**f**, blind RB yields a leakage rate of $\Gamma = 0.13(5)\%$, a total error rate of $\epsilon = 0.74(5)\%$, and a qubit error rate of $\epsilon_q = 0.61(5)\%$ for a Clifford gate fidelity estimate of $1-\epsilon = 99.26(5)\%$ which is comparable to the estimates of the standard RB fits. We discuss this observed leakage in Supplementary Section 5.8.7.

We note that neither the X/Y or X/Z compilations used are maximally efficient at compiling Clifford operations from primitive operations. Therefore, the Clifford gate fidelities extracted from randomized benchmarking could themselves be improved by tailoring the gate set to the physical gates. The average gate fidelity estimates should therefore be the most reasonable quantitative benchmark with which to compare the gate performance.

### 5.6.4. TIP ANGLE FITTING

There are multiple strategies to estimate the quantization axis tip $\theta$ between two dots. The visibility of oscillations observed after diabatically

shuttling from one dot to another can be directly related to the tip in quantization axis [24]. This provides a reasonable estimate if the maximum visibility of oscillations can be established and provides good contrast. Alternatively, the Larmor frequency as a function of detuning across the hopping double-dot pair can be measured and fit to Eq. S25 [24, 25]. Both of these methods are made difficult in our case by not having EDSR control at the magnetic field condition at which hopping gates are possible.

Here, we take advantage of the fact that a number of repetitions $r$ of the shuttling sequence as drawn in Fig. 5.4**a** will result in a unique 2D "fingerprint" as a function of the timing parameters $t_1$ and $t_2$. Generally, the pattern will depend more sensitively on the tip $\theta$ as $r$ increases. Exemplary patterns for both dot pairs are shown in Extended Data Fig. 5.6.

We may model the pattern using the two-level Hamiltonian given in Eq. S27 and make the approximation that the change in the Hamiltonian as a function of interdot detuning is perfectly sharp given the nanosecond-scale detuning ramp times [25]. The time evolution is therefore a product of unitary Larmor precessions. In the initial dot, this precession occurs at an angular frequency of $\omega_{\text{init}}$ about a quantization axis $\hat{z} = (0, 0, 1)^T$. In the tipped dot, this precession occurs at an angular frequency of $\omega_{\text{tip}}$ about a quantization axis $\hat{\theta} = (\sin\theta, 0, \cos\theta)^T$. Since the detuning ramp times are still finite, precession occurs during the ramps and can be accounted for by adjusting the nominal precession time such that $t_1' = t_1 - t_{1,\text{offset}}$ and $t_2' = t_2 - t_{2,\text{offset}}$. The unitary evolution for $r$ repetitions of the sequence shown in Fig. 5.4**a** is therefore given by:

$$U(t_1', t_2', t_{\text{add}}, \omega_{\text{init}}, \omega_{\text{tip}}, \theta) = \left(R_z(\omega_{\text{init}}(t_2' + t_{\text{add}}))R_\theta(\omega_{\text{tip}}t_1')R_z(\omega_{\text{init}}t_2')R_\theta(\omega_{\text{tip}}t_1')\right)^r \quad (5.6)$$

where $R_n(\alpha) = \exp(-i\alpha\hat{n}\cdot\vec{\sigma}/2)$ indicates a positive rotation about the unit vector $\hat{n}$ by an angle $\alpha$. The measured pattern is given by:

$$p_{\text{odd}}(t_1', t_2', t_{\text{add}}, \omega_{\text{init}}, \omega_{\text{tip}}, \theta, A, B) = A\,\text{Tr}\left(OU\rho_{\text{odd}}U^\dagger\right) + B, \quad (5.7)$$

where $\rho_{\text{odd}}$ is the initialized odd-parity state, $O = (\mathbb{1} - \sigma_z \otimes \sigma_z)/2$ is the odd-parity observable, and $A$ and $B$ are visibility and offset corrections due to SPAM errors.

We fit the experimental data to Equation. 5.7 with a pixel-by-pixel least-squares optimization over the parameters $t_{1,\text{offset}}$, $t_{2,\text{offset}}$, $\omega_{\text{init}}$,

$\omega_{\text{tip}}$, $A$, $B$, and $\theta$. $t_{\text{add}}$ is known exactly from the experiment definition. As the qubit frequencies, offset times, and visibilities are well-estimated from other experiments, they are optimized within narrow bounds. For $r = 4$, the optimized value for $\theta$ is accurate within a degree. For fewer repetitions, the fit is less accurate, and we instead simulate using the $r = 4$ fit directly.

## 5.7. EXTENDED DATA FIGURES

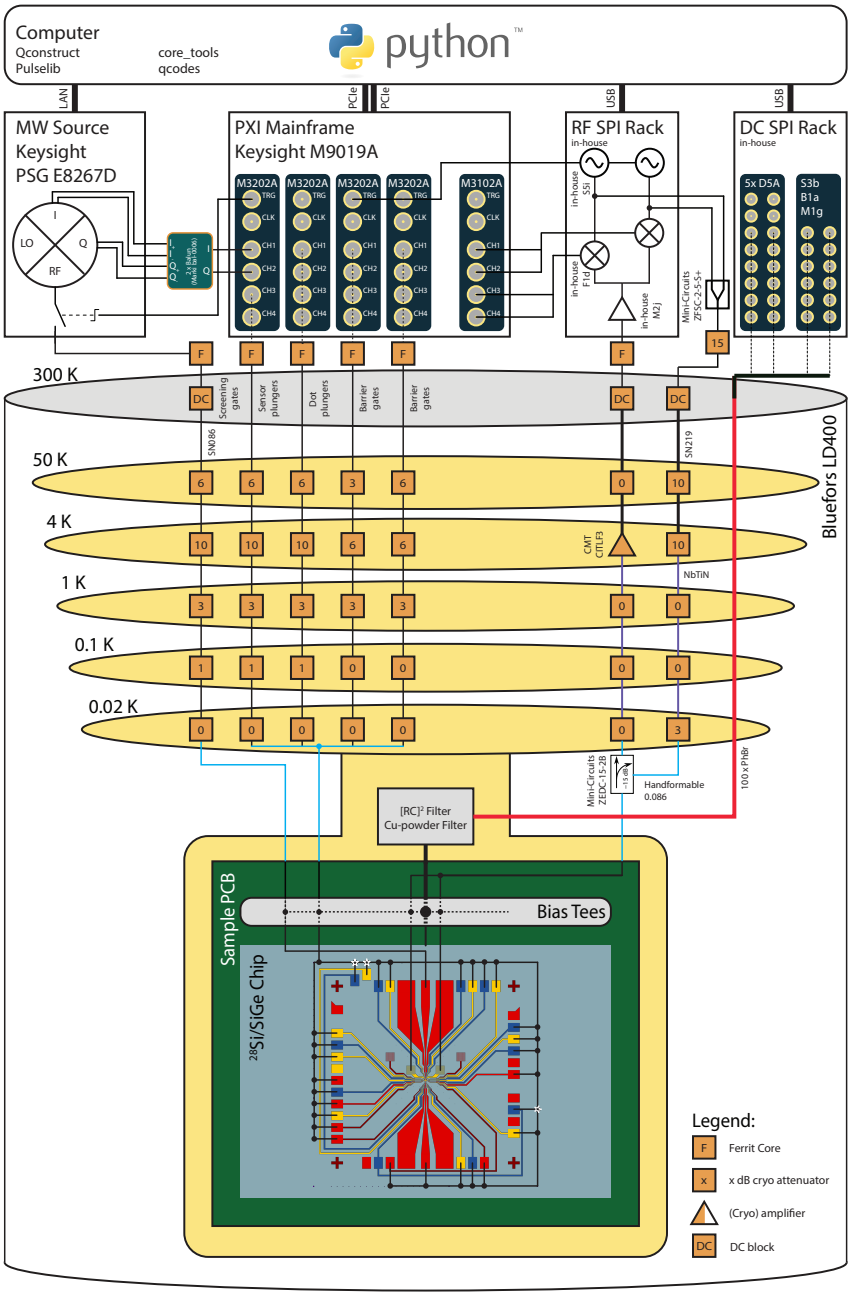


**Extended Data Fig 5.1: Schematic of the experimental setup.** Arbitrary Waveform Generators (AWG, Keysight M3202A) in a PXI chassis are used to generate baseband pulses as well as I/Q input signals for the microwave (MW) vector source (Keysight PSG E8267D). [cntd.]

**Extended Data Fig 5.1: Schematic of the experimental setup.** Baseband signals are supplied to all plunger and barrier gates comprising the 2x2 array along with both sensing dot plunger gates. Lines routed to barrier gates are attenuated less to allow for larger voltage pulses on these gates. Wideband modulation with differential I/Q inputs is implemented using Balun's (Marki bal-0006). Ferrite cores are used to reduce low-frequency noise. Double DC blocks (Pasternack PE8210) are used on the microwave drive line and rf-reflectometry readout lines. DC voltages are supplied by battery-powered low-noise voltage sources and are filtered with low-pass RC filters and copper-powder filters before being combined on the sample PCB using bias tees with RC time constants of 100 ms. Two carrier frequencies are generated using homemade sources that are triggered by AWG marker channels and routed via bias tees to two readout tank circuits which are connected to accumulation gates adjacent to the two sensing dots using the split-gate method [42]. The tank circuit consists of a series NbTiN inductor wirebonded on the PCB, the capacitance between the accumulation gate and the underlying 2DEG, as well as the resistive SET. The path from the 2DEG to the ohmic contact is depleted to minimize resistive leakage to ground. The reflected signal is separated from the incoming carrier with a directional coupler (Mini-Circuits ZEDC-15-2B), amplified at 4 Kelvin (CMT CITLF3) and room temperature before being demodulated and digitized (Keysight M3102A).

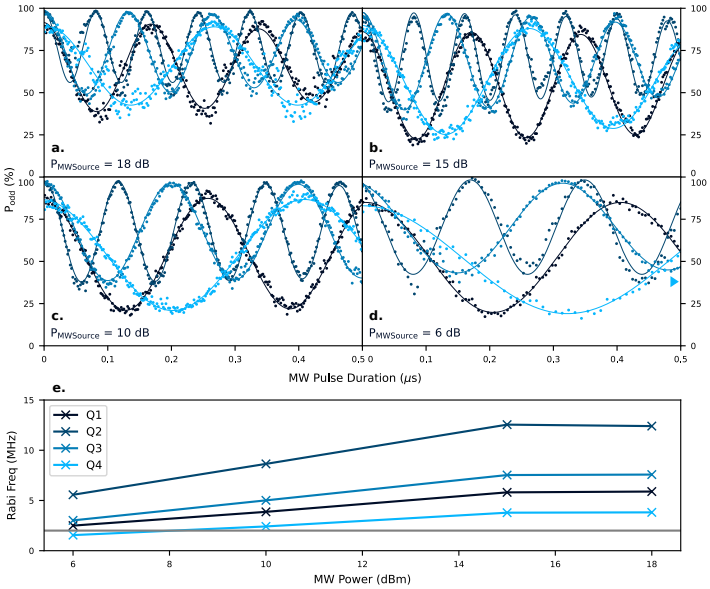


**Extended Data Fig 5.2: Rabi oscillations at various MW powers. a.-d.** Measured (data points) and fitted (solid lines) Rabi oscillations for all four qubits at various powers of the MW-source as annotated in the figures. We point out that the data of $Q_4$ in panel **d** was cropped as indicated by the marker. The fit was performed with the full oscillation. Visibility differences between panel a) and panels b) through d) can be attributed to a retuning of initialization and read out parameters. **e.** Rabi frequencies plotted against the MW-source powers. Above 15 MHz we observe a saturation on all qubits that is caused by the limitations of the microwave source. For the experiments in the main text we used 6 MHz and adjusted the IQ input amplitudes to achieve a Rabi frequency of around 2 MHz (grey line) on all 4 qubits.

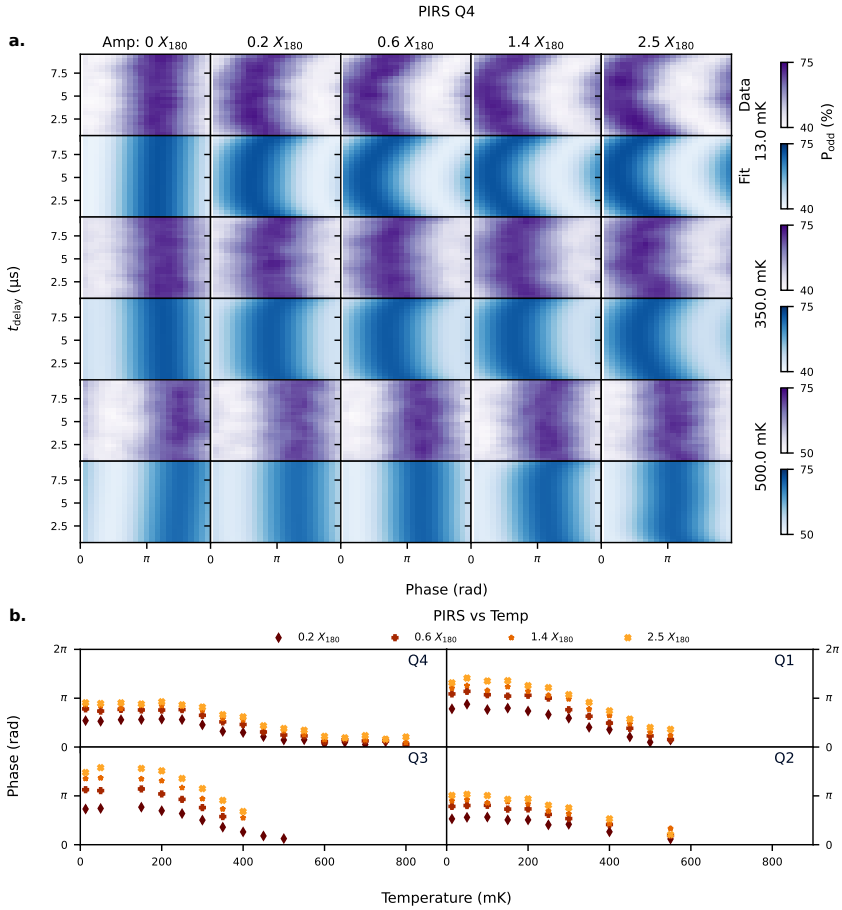


**Extended Data Fig 5.3: PIRS during EDSR operation.** **a.** Experimental data (purple) and respective fits (blue) for different off-resonant burst amplitudes at three exemplary mixing chamber temperatures for Qubit 4 (see Fig. 5.2 for the pulse sequence schematic). As the individual traces at constant $t_{\text{delay}}$ are both low in visibility due to the long echo pulse sequence used and subject to small signal drifts over the course of the long experiments, we fit the 2D datasets to Eq. S24 using a quartic polynomial representation of $\theta_t(t_{\text{delay}}) = \sum_{k=0}^{4} c_k (t_{\text{delay}} - t_0)^k$ to extract the smooth transient phase accumulation from the off-resonant burst as a function of $t_{\text{delay}}$. In the left-most column, the experiment is a standard Hahn-echo sequence, and a constant phase offset is observed at the different temperature settings. We subtract this constant offset from the datasets plotted to the right which are collected at the same temperature in order to isolate the transient effect of the off-resonant burst. [cntd.]

**Extended Data Fig 5.3: PIRS during EDSR operation. b.** To quantify the relation between temperature and non-linear transient phase pick-up, we plot the maximum phase accumulation at as a function of mixing chamber temperature for all four qubits. All qubits exhibit the same behaviour whereby the maximum phase pickup is suppressed by operating at higher device temperatures. The positive phase accumulation is consistent with a negative qubit frequency shift given the definition of the rotating frame used in these experiments (see Supplementary Information Section 5.8.4)

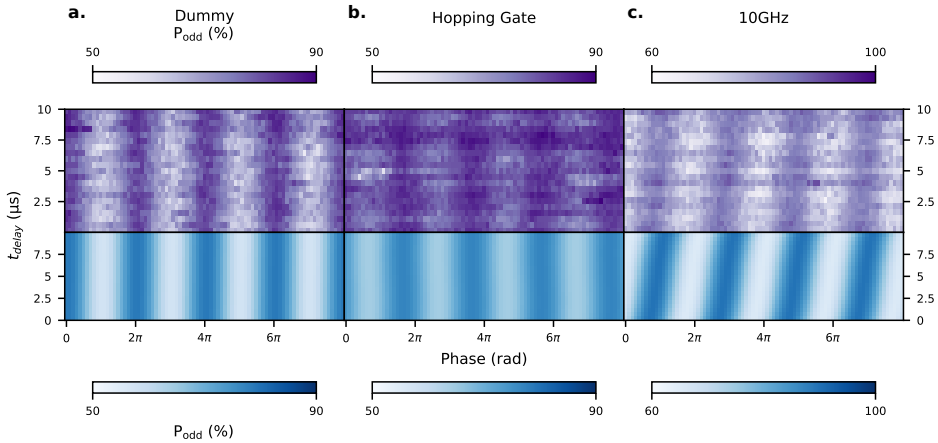


**Extended Data Fig 5.4: PIRS during baseband operation. a.-c.** Experimental data (purple) and respective fits (blue) using three variants of the PIRS experiment. **a.** The Hahn-echo pulse template is implemented on Qubit 1 using hopping gates. The same fitting procedure as described in Extended Data Fig. 5.3 is used. No off-resonant burst or pulse is applied. **b.** An $X_{180}$ hopping gate is applied to Qubit 4 in place of the off-resonant burst. Qubit 1 experiences a non-transient phase pickup in addition to a 180° phase shift due to the change in measurement parity. The visibility is notably degraded compared to the other experiments due to the effect of baseband pulsing on gate P3. **c.** A 10 GHz burst is applied with an amplitude and duration energetically commensurate with $0.6X_{180}$ during standard EDSR operation. A transient phase pickup is observed, but no "saturation" effect as in Extended Data Fig. 5.3 is seen. We believe this is due to the implementation of the decoupling pulse with a hopping gate rather than a resonant gate. The hopping gate itself does not impart a PIRS effect on the device.

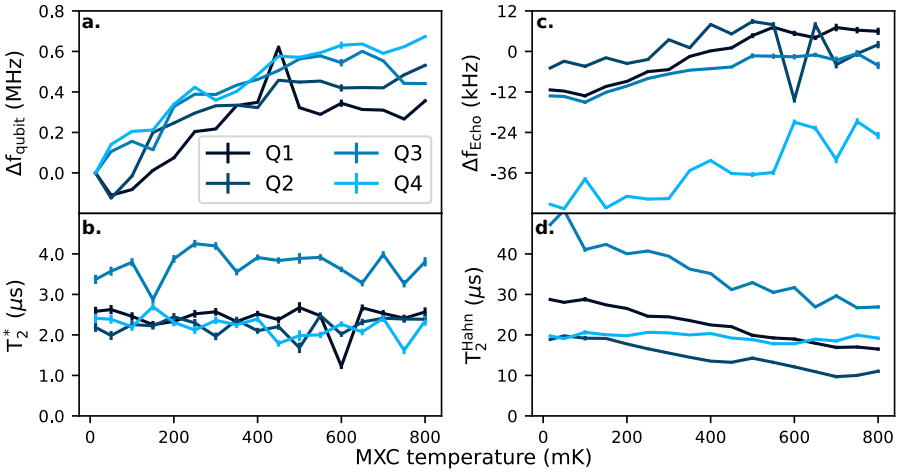


5

**Extended Data Fig 5.5: Temperature dependence of $T_2^*$, $T_2^H$ and qubit frequencies. a.-b.** Data extracted from Ramsey experiments (approx. 30 min) conducted using EDSR control as a function of mixing chamber temperature. The measured oscillations can be fit to extract **a.** the qubit frequency and **b.** the Ramsey decay time $T_2^*$ per Supplementary Information Section 5.8.4. Discounting spurious jumps in qubit frequency on the order of 100 kHz which we attribute to slow charge fluctuators, all qubit frequencies increase monotonically as a function of temperature within the range we are able to measure. The Ramsey decay times are notably unaffected by the device temperature for all four qubits. **c.-d.** Hahn-echo experiments (approx. 30 min) conducted using EDSR control as a function of mixing chamber temperature. The measured oscillations can be fit to extract **c.** the difference in qubit frequency before and after the decoupling pulse and **d.** the Hahn-echo decay time $T_2^H$ per Supplementary Information Section 5.8.4. The systematic difference in qubit frequencies is predominantly attributed to the PIRS induced by the decoupling $X_{180}$ pulse as it has a greater duration than the initial $X_{90}$ pulse. This systematic frequency difference appears to converge to zero as the mixing chamber temperature is increases, which is consistent with the observation that an increased device temperature mitigates the PIRS effect (see Extended Data Fig. 5.3). Hahn-echo decay times for all qubits except Qubit 4 monotonically decrease as a function of mixing chamber temperature. Qubit 4's coherence remains constant with the changing temperature. The plotted error bars in all panels represent the standard deviation of the fitted parameters.

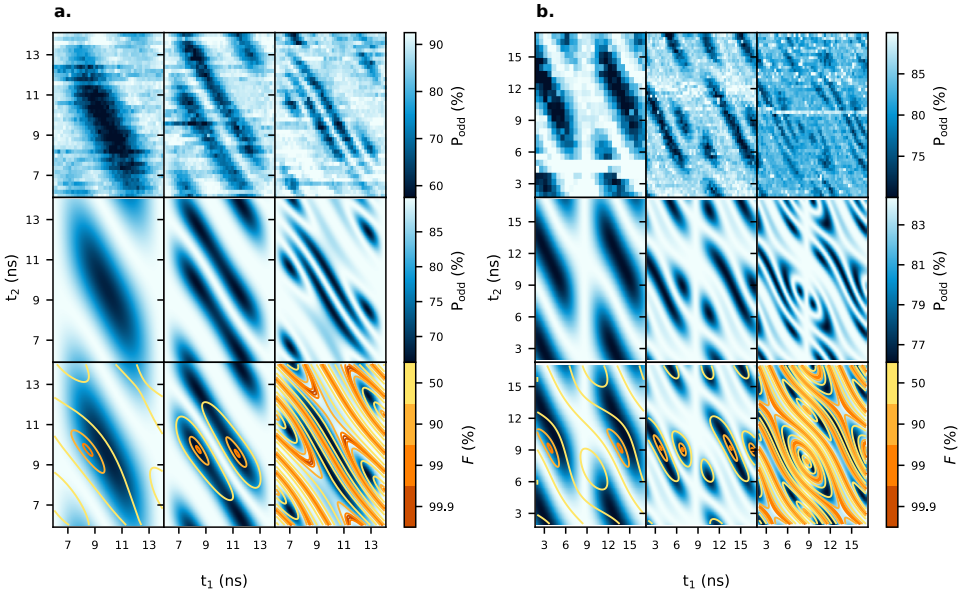


**Extended Data Fig 5.6: Hopping gate characterisation of D1D2 and D4D3.** Raw data (row 1), simulated data (row 2) and estimated gate fidelity (row 3) of one (column 1), two (column 2) and four (column 3) shuttle repetitions for **a.** the qubit in D1 and **b.** the qubit in D4. In both cases we used two shuttle cycles per repetition. To generate the simulated data sets we fit the four-repetition pattern and extract parameters such as the quantisation axis tip and timing offsets due to finite ramp times. Using the simulated data we calculate the gate fidelity as indicated by the contour plots: for one repetition, we calculate the $X_{90}$ fidelity; for two repetitions, we calculate the $X_{180}$ fidelity; and for four repetitions, we calculate the $X_{360}$ fidelity. The fidelity is calculated by assuming instantaneous shuttling between dots and considering only unitary spin state evolution. In the case of shuttling with Qubit 4, we observe the degradation of the readout signal due to the repeated pulsing on gate P3 (see Methods)

**Table 5.1: Lever arm, electron temperature and tunnel coupling measurements.** Lever arms in the 2x2 array. Virtualized sensor dot plungers (vS1P and vS2P) and virtualized loading barriers (vS1LB and vS2LB) are extracted directly via Coulomb diamonds. Virtualized quantum dot plungers (vP1 - vP4) are inferred by propagating the slope of interdot transitions through the array. The uncertainty of the virtual plunger gates is dominated by the uncertainty of propagating the sensor lever arm into the 2x2 array.

| Gate | Lever arm |
|---|---|
| vS1P | $0.1542 \pm 0.0017$ |
| vS1LB | $0.0155 \pm 0.0004$ |
| vS2P | $0.1537 \pm 0.0029$ |
| vS2LB | $0.0151 \pm 0.0002$ |
| vP1 | $0.0289 \pm 0.0083$ |
| vP2 | $0.0455 \pm 0.0131$ |
| vP3 | $0.0290 \pm 0.0084$ |
| vP4 | $0.0349 \pm 0.0101$ |

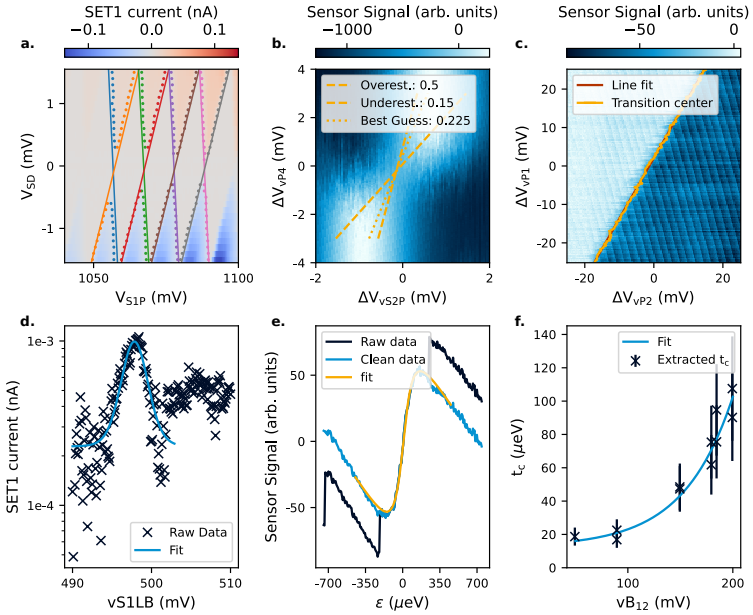


**Extended Data Fig 5.7: Lever arm, electron temperature and tunnel coupling measurements.** **a.** Coulomb diamonds of SET 1 showing the extracted slopes used to calculate the lever arm of the sensing dot plunger. **b.** An exemplary interdot transition of sensing dot 2 and quantum dot 4. The shift of the coulomb peak (bright white line) due to the added charge on quantum do $D_4$ is used for determining the lever arm ratio between the sensing dot plunger and the quantum dot plunger. Dashed and dotted lines show the manual over- and under-estimation as well as the best fit. The latter takes into account that both lever arms for vS1P and vS2P have to be in an agreement when propagated through the array. **c.** An exemplary interdot transition between quantum dots 1 and 2 used for determining the lever arm ratio between the two plunger gates. We fit the interdot transition line-by-line to extract a consistent centre point followed by a linear fit through all centre points to determine the slope. **d.** Coulomb peak and fit to extract a bound on the electron temperature of about $T_e < 175\,\mathrm{mK}$. **e.** Exemplary fit of an interdot transition to extract the tunnel coupling [44]. The detuning lever arm as computed in panels **a-c** as well as the electron temperature from **d** are used in this fitting procedure. The sensing dot plunger is virtualized with respect to the detuning, and discrete steps in the measured signal due to finite AWG resolution are extracted from the measured transition prior to fitting. **f.** Extracted tunnel couplings between dots 1 and 2 plotted against the respective barrier voltage showing the expected exponential dependency. The plotted error bars represent the standard deviation of the fit using the nominal value of the fitted lever arm and electron temperature.

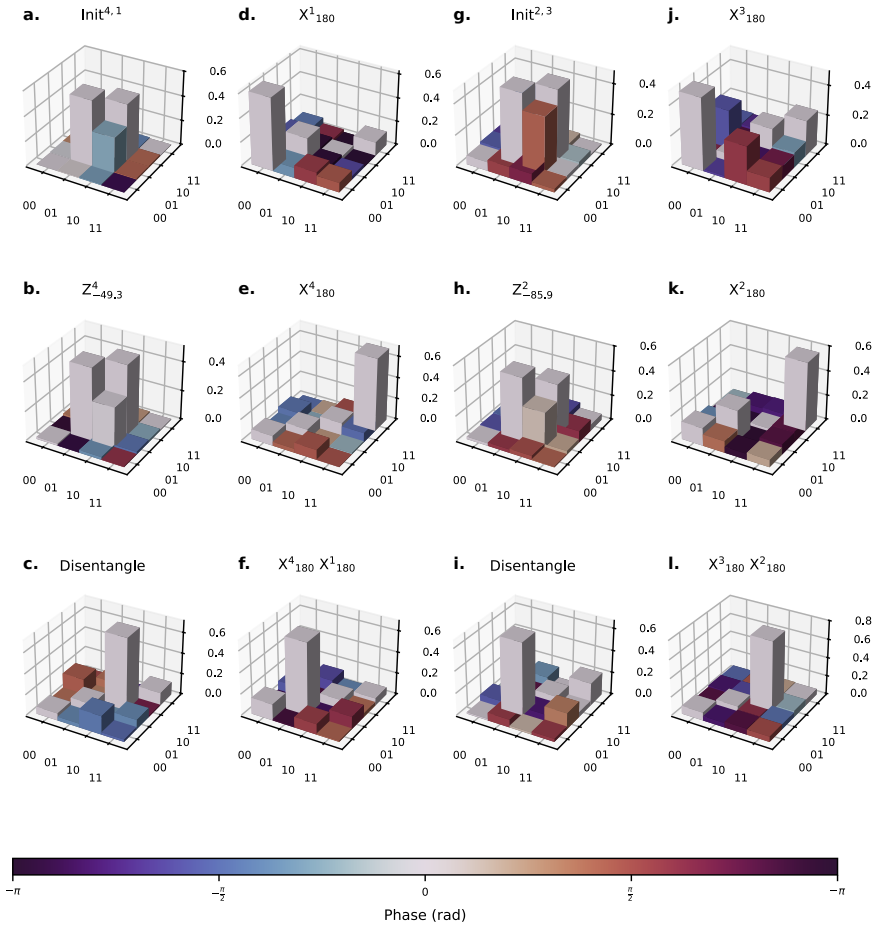


**Extended Data Fig 5.8: Quantum State Tomography of Qubit Pairs Q4Q1 (a.-f.) and Q2Q3 (g.-l.) obtained using EDSR and CZ operations. a./g.** Tomography of the initial state. As we transition quickly out of the (0,2)/(2,0) charge state to the (1,1) charge state, we initialise predominantly in an entangled state in the $\{|01\rangle, |10\rangle\}$ subspace. This diabatic initialization offers more consistent state preparation compared to slow adiabatic ramping. In both cases we still observe a significant classical mixture of the two odd-parity states. For the single-qubit measurement protocols used in this work, a mixed initial state has no impact on the final result. However, such poor initialization has a large impact on most multi-qubit experiments. **b./h.** The initialized state after applying a phase operation to produce a $|T_0\rangle$ state. [cntd.]

**Extended Data Fig 5.8: Quantum State Tomography of Qubit Pairs Q4Q1 (a.-f.) and Q2Q3 (g.-l.) obtained using EDSR and CZ operations. c./i.** The initialized state after disentangling the qubits with a CZ and H gate. **d.-f./j.-l.** The disentangled initial state after various $X_{180}$ gates to transform between the product states. A full two-qubit gate set is required to implement quantum state tomography on both Pauli spin blockade pairs illustrating full quantum logic on this device. The poor fidelity of the initial state as well as the poor quality factors of the two-qubit interactions limit the quality of further multi-qubit characterization on this particular device.

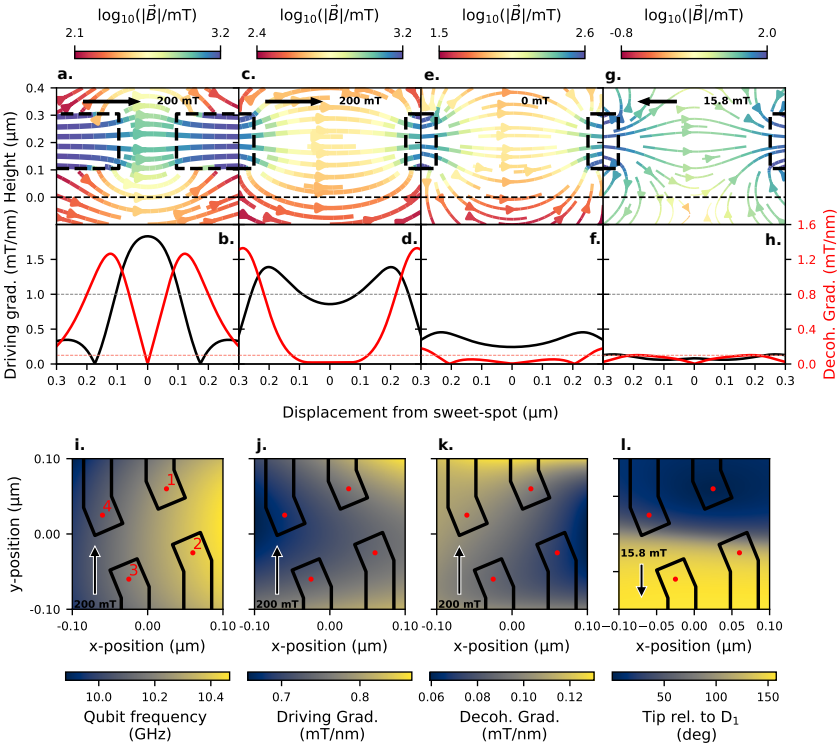


**Extended Data Fig 5.9: Micromagnet Simulations. a.** Magnetic field lines forming in a micromagnet gap of 190 nm as used in [10] when an external field of 200 mT is applied as indicated. No addressability features along the x-axis are included in the magnet design, so the field lines only exist in the y-z plane. The dashed line indicates the level at which the 2DEG and quantum dots would be formed below the magnet. **b.** The simulated driving gradient (black) along the y-axis and estimated decoherence gradient (red) corresponding to the magnet design in **a**. The black dashed line indicates the 1 mT/nm minimum threshold for good EDSR control, and the red dashed line indicates the 0.1 mT/nm maximum threshold for good charge-noise resilience. Although a good driving gradient is present, the decoherence sweet spot is only wide enough to support a linear qubit array. **c.** Magnetic field lines forming in a micromagnet gap of 500 nm similar to the design used in this work when an external field of 200 mT is applied as indicated. **d.** The simulated driving and decoherence gradients corresponding to the magnet design in **c**. Good EDSR is generally possible, and the decoherence sweet spot is wider than in **a-b**. **e.** Magnetic field lines forming in a micromagnet gap of 500 nm when no external field is applied. [cntd.]

**Extended Data Fig 5.9: Micromagnet Simulations. f.** The simulated driving and decoherence gradients corresponding to the magnet design in **e.**. EDSR is only possible with a stronger driving field, but the sweet spot in which to form good qubits is substantially wider. **g.** Magnetic field lines forming in a micromagnet gap of 500 nm when an external field of 15.8 mT is applied as indicated. **h.** The simulated driving and decoherence gradients corresponding to the magnet design in **g**. EDSR is effectively impossible due to the small gradient, but qubits may be controlled via shuttling. The decoherence sweet spot is still wide. **i.** Simulated qubit frequencies using the nominal micromagnet design used in this work and an external field of 200 mT. The polarization of the micromagnet used in simulation is inferred based on the measured qubit frequencies. The gate overlay indicates the approximate locations where Qubits 1-4 are formed in the magnetic field. **j.** The simulated driving gradient along the y-axis with an external field of 200 mT. **k.** The simulated decoherence gradient with an external field of 200 mT. **l.** The simulated tip in quantization axis relative to Dot 1 with an external field of 15.8 mT oriented opposite the micromagnet polarization illustrating the substantial tips formed between dots $D_1D_2$ and $D_3D_4$.

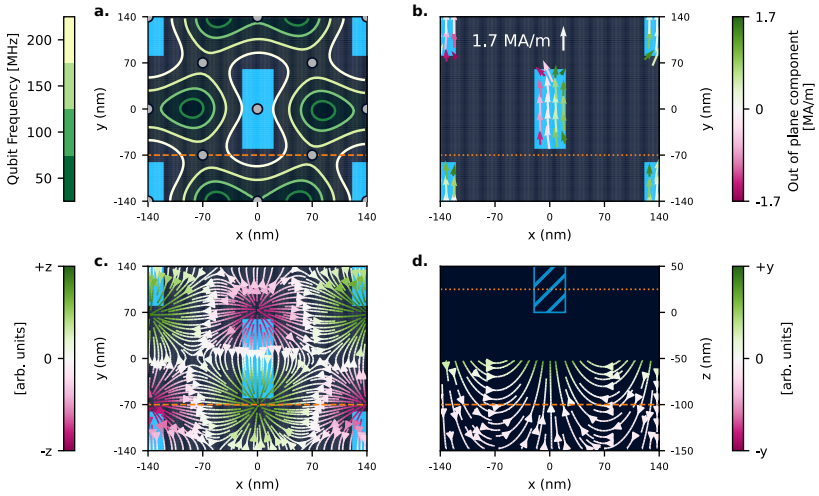


**Extended Data Fig 5.10: Nanomagnet Simulations. a.** Zoomed-in nanomagnet pattern as introduced in Fig. 5.5. The magnets are shown in bright blue. The bottom surface of the magnets is defined as $z = 0$. For the simulations, we choose Fe as the magnetic material [32] with saturation magnetization $M_s = 1.7\,\mathrm{MA/m}$, exchange stiffness $A_{ex} = 21\,\mathrm{pJ/m}^3$, nanomagnet size $\{l_x, l_y, l_z\} = \{40\,\mathrm{nm}, 120\,\mathrm{nm}, 50\,\mathrm{nm}\}$, cell size $x, y, z = 5\,\mathrm{nm}$ and simulated volume $\{L_x, L_y, L_z\} = \{3990\,\mathrm{nm}, 3815\,\mathrm{nm}, 200\,\mathrm{nm}\}$. The grey dots mark quantum dot locations, and the orange dashed line marks the intersection with the plot shown in panel **d**. The contour lines show the estimated qubit frequency distribution in a quantum well at $z = -100\,\mathrm{nm}$ assuming a $g$-factor of 2 for silicon. No external magnetic field is present. **b.** Magnetization of the nanomagnets at $z = 25\,\mathrm{nm}$. The dotted orange line marks the intersection with the plot shown in panel **d**. The color of the quiver arrows shows the z-component of the magnetization. The nanomagnets are originally magnetized along the positive y-axis. After the external field is removed, the shape anisotropy maintains the magnetization predominantly in the y-direction. **c.** Magnetic field lines in the x-y quantum dot plane at $z = -100\,\mathrm{nm}$. The stray field causes the relative quantization axis tips between the dot locations indicated in **a** to be about 90°. The dashed line indicates the intersection with panel **d**. **d.** Stray field lines in the x-z plane at $y = -70\,\mathrm{nm}$. The dashed and dotted orange lines mark the intersections with the planes shown **a**,**b** and **c**. To maintain good visibility, only the region up to $z = -50\,\mathrm{nm}$ is depicted. The crosshatched blue square indicates the position of the magnetic layer, though there is no nanomagnet present in this plane. The inhomogeneity of the stray field extends relatively far below the magnetic layer allowing ample space for independent gate electrodes.

## 5.8. SUPPLEMENTARY INFORMATION

### 5.8.1. DERIVING SPIN PROPERTIES FROM MAGNETIC FIELD SIMULATIONS

Here, we review how the stray field from on-chip magnets is calculated and how this field determines the spin physics in a 2D array of quantum dots. This is salient as much of the existing literature focuses on the simplified case of linear spin arrays and fails to predict qubit properties away from the sweet spot at low external magnetic field amplitudes. The EDSR Hamiltonian is useful as it elucidates both how a transverse gradient permits qubit control as well as how electric field fluctuations due to charge noise couple to the qubit. Similar derivations may be found in [45] and [46]. The Hamiltonian has the form:

$$H = -\frac{E_Z}{2}\sigma_z - \frac{\Delta_o}{2}\tau_z + \frac{\Lambda}{2}\tau_x\sigma_x - \frac{\lambda}{2}\tau_x\sigma_z + E(t)\tau_x. \tag{5.8}$$



$\sigma$ and $\tau$ denote Pauli matrices that act on the 2-level spin state or (truncated) 2-level orbital state respectively. $E_Z = g\mu_B B_{\text{tot}}$ is the Zeeman splitting. $g = 2$ is the electron spin $g$-factor, $\mu_0$ is the Bohr magneton, $B_{tot}$ is the magnitude of the total magnetic field present at the dot, and $\hbar$ is the reduced Planck's constant. We make the simplifying approximation that the $g$-factor for an electron spin in silicon is isotropic such that the spin's quantization axis is effectively set by the direction of the total magnetic field vector.

$\Delta_o$ is the orbital energy splitting of the dot, which is typically on the order of 1 meV. Although some valley-orbit hybridization may take place, for simplicity we assume it is the orbit-like dipole of length $\langle g|\hat{r}|e\rangle = a_0/\sqrt{2}$ that dominates electric coupling to the charge state of the confined electron. $a_0 = \sqrt{\hbar^2/m^*\Delta_0}$ is the length scale of the dot. For the silicon quantum well, $m^*$ is 19% of the free electron mass.

$E(t) = E^{\text{drive}}(t) + E^{\text{noise}}(t)$ represents a time-dependent electric field that may consist of an intentional drive as well as environmental charge noise. The electric driving field is given by $E^{\text{drive}}(t) = eE^{\text{drive}}_{\text{ac}} a_0 \cos(\omega t)/\sqrt{2}$ and is oriented along the in-plane unit vector $\hat{\mathbf{r}} = r_x\hat{\mathbf{x}} + r_y\hat{\mathbf{y}}$. We assume any out-of-plane component does not participate in the EDSR mechanism. $e$ is the elementary charge of the electron and $E^{\text{drive}}_{\text{ac}} \approx 1000$ V/m is the amplitude of the electric field. Similarly, charge noise fluctuations of a particular frequency $\omega'$ may be expressed as $E^{\text{noise}}(t) = eE^{\text{noise}}_{\text{ac}} a_0 \cos(\omega' t)/\sqrt{2}$. The amplitude of the fluctuations $E^{\text{noise}}_{\text{ac}} \approx 10$ V/m may be estimated from charge noise measurements.

$\Lambda = g\mu_B \left|\frac{dB_\perp}{dr}\right| \frac{a_0}{\sqrt{2}}$ gives the energy scale for the synthetic spin-orbit coupling where $\left|\frac{dB_\perp}{dr}\right|$ is the slanting field perpendicular to the

quantization axis calculated along the axis of the time-dependent electric fluctuations. The orientation of $B_\perp$ is ambiguous, because there are two orthogonal axes to the quantization axis. This would give rise to $\tau_x\sigma_x$ and $\tau_x\sigma_y$ couplings in the Hamiltonian. By rotating the spin basis about the quantization axis, these contributions can be combined into a single energy scale. $\lambda = g\mu_B \left|\frac{dB_{tot}}{dr}\right| \frac{a_0}{\sqrt{2}}$ describes the effect of the decoherence gradient, whereby the qubit energy may fluctuate due to charge noise. While we can engineer the orientation of an applied electric drive, charge noise may push the confined electron in any x-y direction, so we aim to calculate a reasonable upper bound of $\left|\frac{dB_{tot}}{dr}\right|$.

Considering the spin-orbit coupling and time-dependent fluctuation energy scales as small with respect to the orbital splitting, Schrieffer-Wolff perturbation theory may be used to derive the relevant off-diagonal element $\Omega$ for driving spin transitions as well as the diagonal element $\delta\omega_0$ coupling electric fluctuations to the effective qubit energy splitting to first order:

$$\Omega = \frac{g\mu_B a_0^2 \left|\frac{dB_\perp}{dr}\right| eE_{ac}^{drive}}{2\hbar\Delta_o}, \tag{5.9}$$

$$\delta\omega_0 = \frac{g\mu_B e\hbar \left|\frac{dB_{tot}}{dr}\right| E_{ac}^{noise}}{m^*\Delta_o^2}. \tag{5.10}$$

The synthetic spin-orbit coupling also introduces a small, constant renormalization to the Zeeman splitting, but this is unimportant in the context of practical qubit calibration as it is the hybridized qubit frequency $\omega_0$ which is measured directly. These relations directly imply the oft-stated conditions that good EDSR control ($f_{Rabi} = \Omega/2\pi > 5\,\text{MHz}$) is achieved when $\left|\frac{dB_\perp}{dr}\right| > 1\,\text{mT/nm}$ and good charge-noise-limited coherence properties ($T_2^* \approx 1/\delta\omega_0 > 10\,\mu\text{s}$) should restrict $\left|\frac{dB_{tot}}{dr}\right| < 0.1\,\text{mT/nm}$. In summary, the total magnetic field, transverse gradient, and decoherence gradient form the most relevant quantities to calculate to predict EDSR behaviour.

In the case of low-field operation when hopping spins may be used for single-qubit gate control, the tip in quantization axes between adjacent quantum dots becomes an important metric. While valley-orbit hybridization and intrinsic spin-orbit coupling will cause some site-to-site variation in the $g$-tensor of the electron spins in the silicon quantum well, the spin quantization axis will predominantly be aligned with the direction of the magnetic field vector at the relevant dot locations [47]. The tip angle can therefore also be predicted from an accurate magnetic field simulation with quantitative accuracy limited by the accuracy of

both the magnet modelling and the electrostatic confinement of the dots.

In Sections 5.8.2 and 5.8.3, we summarize the magnetic field simulation strategies employed in this paper. Regardless of how the magnetic vector field is computed, the relevant quantities for understanding spin control can be computed in the same way. We represent the sum of the constant external field and ferromagnetic stray field as a total vector field:

$$\mathbf{B} = \begin{pmatrix} B_x \\ B_y \\ B_z \end{pmatrix}. \tag{5.11}$$

We assume that the qubit locations are point-like as the field varies slowly over the length scale of the electron wavefunction. The total magnetic field $B_{\text{tot}}$ setting the Zeeman energy is:

$$B_{\text{tot}} = \sqrt{B_x^2 + B_y^2 + B_z^2}. \tag{5.12}$$



With the additional assumption that the $g$-factor of an electron in the conduction band minimum is isotropic, the quantization axis is set by the direction of the total magnetic field:

$$\hat{\mathbf{u}}_{\text{tot}} = \frac{B_x}{B_{\text{tot}}}\hat{\mathbf{x}} + \frac{B_y}{B_{\text{tot}}}\hat{\mathbf{y}} + \frac{B_z}{B_{\text{tot}}}\hat{\mathbf{z}}. \tag{5.13}$$

We can find the perpendicular axes using the Gram-Schmidt process, taking $\{\hat{\mathbf{u}}_{\text{tot}}, \hat{\mathbf{x}}, \hat{\mathbf{z}}\}$ as the starting set of normal vectors:

$$\hat{\mathbf{u}}_{\perp,1} = \hat{\mathbf{x}} - (\hat{\mathbf{u}}_{\text{tot}} \cdot \hat{\mathbf{x}})\hat{\mathbf{u}}_{\text{tot}}, \hat{\mathbf{u}}_{\perp,2} = \hat{\mathbf{z}} - (\hat{\mathbf{u}}_{\text{tot}} \cdot \hat{\mathbf{z}})\hat{\mathbf{u}}_{\text{tot}} - (\hat{\mathbf{u}}_{\perp,1} \cdot \hat{\mathbf{z}})\hat{\mathbf{u}}_{\perp,1}, \tag{5.14}$$

The transverse fields are therefore $B_{\perp,1/2} = \mathbf{B} \cdot \hat{\mathbf{u}}_{\perp,1/2}$ and equal 0 at the qubit locations. The total transverse gradient is found by taking the total directional derivative of each gradient along the driving axis:

$$\left|\frac{dB_\perp}{dr}\right| = \sqrt{(\hat{\mathbf{r}} \cdot \nabla B_{\perp,1})^2 + (\hat{\mathbf{r}} \cdot \nabla B_{\perp,2})^2} \tag{5.15}$$

$$= \sqrt{\left(\frac{\partial B_{\perp,1}}{\partial x} r_x + \frac{\partial B_{\perp,1}}{\partial y} r_y\right)^2 + \left(\frac{\partial B_{\perp,2}}{\partial x} r_x + \frac{\partial B_{\perp,2}}{\partial y} r_y\right)^2}. \tag{5.16}$$

We refer to Equation 5.16 as the driving gradient.

For a particular fluctuation axis $\hat{\mathbf{r}'} = r'_x\hat{\mathbf{x}} + r'_y\hat{\mathbf{y}}$, the decoherence gradient is given by the directional derivative:

$$\left|\frac{dB_{\text{tot}}}{dr}\right| = \left|\hat{\mathbf{r}}' \cdot \nabla B_{\text{tot}}\right|. \tag{5.17}$$

Since we don't know along which axis charge noise will predominantly push the dot, we can estimate a bound by taking the norm of the in-plane gradient:

$$\left|\frac{dB_{\text{tot}}}{dr}\right|_{\text{max}} \approx \sqrt{(\hat{\mathbf{x}} \cdot \nabla B_{\text{tot}})^2 + (\hat{\mathbf{y}} \cdot \nabla B_{\text{tot}})^2}. \tag{5.18}$$

We refer to Equation 5.18 as the decoherence gradient.

Often, the driving axis is designed to align with the same cartesian axis as the external field (e.g. $\hat{\mathbf{y}}$) and the transverse field is dominated by another cartesian component (e.g. $\hat{\mathbf{z}}$) such that the driving gradient can be approximated as $|\partial B_z/\partial y|$. Similarly, the decoherence gradient can be approximated as $|\partial B_y/\partial x| + |\partial B_y/\partial y|$. However, applying these approximations becomes less accurate in regimes where the inhomogeneous stray field of on-chip magnets dominates the uniform external field.

Finally, the quantization axis tip between adjacent spin sites can be computed from the respective magnetic field vectors $\mathbf{B}_1$ and $\mathbf{B}_2$ at each site as:

$$\theta_{\text{tip}} = \cos^{-1}\left(\frac{\mathbf{B}_1 \cdot \mathbf{B}_2}{B_{1,\text{tot}} B_{2,\text{tot}}}\right) \tag{5.19}$$

### 5.8.2. MICROMAGNET SIMULATIONS

For micromagnet simulations where the ferromagnetic material can be approximated as a bulk material, we leverage the efficient magnetic field calculations of the Python package magpylib [48]. Such simulations treat the micromagnet as having a homogeneous polarization with no microscopic crystal structure such that the analytic form of the stray field for constituent magnet shapes can be used to calculate the relevant total magnetic vector field.

There are several sources of uncertainty in such a simulation in our context. At a fundamental level, no time-dynamics or domain wall formation is accounted for in the simulations. See [19] for a detailed discussion of magnet simulation approaches and their limitations. Independent of the simulation method, the accuracy is limited to the level of detail included in the magnet model itself as well as knowledge of the precise location of the accumulated quantum dots.

We therefore aim to extract a useful qualitative picture. First, we model the micromagnet using the nominal design. This excludes roughness due to the underlying gate structure, finite rounding of the magnet edges, and other small misalignments from the fabrication procedure.

Second, we use the experimentally measured qubit frequencies to fit the effective homogeneous polarization of the model at a particular external field setting using a least-squares optimization (see Fig. 3). This requires making an assumption about the location of the spins. We take the centre coordinate of the plunger gates as the point-like dot location (as indicated by the red dots in the bottom row of External Data Fig. 9). A more detailed electrostatic simulation could be leveraged to predict the dot locations with more precision, but it is unclear if this confers any benefit due to the approximate nature of the magnetic simulation itself. With a fitted magnet polarization, a field can be simulated from which relevant parameters may be extracted per Section 5.8.1.

The trends predicted in terms of addressability, driving gradient and decoherence gradient all qualitatively match our experimental observations. While the model also predicts when quantization axis tips become substantial, a quantitative estimate becomes very sensitive to the estimated dot locations and the microscopic demagnetization of the micromagnets. Leveraging hopping spins through a larger array could be a powerful *in situ* method of characterizing micromagnet behaviour. Direct cryogenic magnetic imaging of patterned micromagnets would be another straightforward means of verifying magnet behavior.



### 5.8.3. NANOMAGNET SIMULATIONS

To obtain an accurate picture of the periodic stray fields produced by the nanomagnets in the 2D array, we use the OOMMF package [36]. We set the nanomagnets' initial magnetization along the y-axis (their longest axis), which we would perform experimentally by applying an external B-field along the y-axis. We employ an energy minimization evolver/driver (MinDriver) to find the energy-relaxed state of the entire 2D array. The relaxed magnetization will be defined by the nanomagnets' material parameters, as well as their geometry (shape anisotropy), pitch and initial magnetization direction. For the results presented in the main text, we choose Fe with material parameters similar to those in [32], i.e. saturation magnetization $M_s$ = 1700 kA/m, exchange stiffness $A_{ex}$ = 21 pJ/m, and 0 K temperature. We aim for a quantum dot pitch of 100 nm, which requires a nanomagnet pitch of about 280 nm in both the vertical and horizontal direction (this is the pitch within the same row or column). To minimize edge effects, we simulate a rather large volume of 3990 nm x 3815 nm x 200 nm with a cell size of 5 nm in all directions. The nanomagnet sizes are 40 nm x 120 nm x 50 nm. The results in the main text present stray fields at a distance of 100 nm below the nanomagnets, mimicking a quantum well positioned 100 nm below the nanomagnet array. Additional simulations suggest that the exact distance is not critical, as favourable conditions for hopping occur at a range of 90 to 140 nm for the specific sizes of the Fe nanomagnets

shown here. Moreover, we find that by decreasing the thickness of the Fe nanomagnet to 30 nm, we can decrease the qubit frequency and decoherence gradient further while maintaining the same tip angles. Finally, we note that we are not limited to Fe, as we further varied ferromagnetic materials and nanomagnet geometries and could obtain similar outcomes. We leave these optimizations for future studies.

### 5.8.4. SIGN EXTRACTION FROM CROSSTALK EXPERIMENTS

We make use of EDSR to characterize spin physics and encode a set of universal gates with which to perform state tomography. Using the convention $g > 0$ for the electron spin in silicon, the effective two-level Hamiltonian may be given as:

$$H = \omega_0 S_z + 2\Omega \cos(\omega_{\mathrm{MW}} t + \phi) S_x, \tag{5.20}$$



where $\omega_0 \approx g\mu_0 B_{tot}/\hbar$ is the measured qubit Larmor frequency and $\Omega$ is the Rabi frequency due to the effective ac magnetic drive derived in Section 5.8.1. Here, a microwave drive of frequency $\omega_{\mathrm{MW}}$ and phase $\phi$ are used for EDSR. The Loss-DiVincenzo qubit operators are encoded by the spin operators as $\sigma_z = -2S_z/\hbar$ such that $|\downarrow\rangle = |0\rangle$ and $|\uparrow\rangle = |1\rangle$. Therefore, now taking $\hbar = 1$, Equation 5.20 may be rewritten as:

$$H = -\frac{\omega_0}{2}\sigma_z + \Omega \cos(\omega_{\mathrm{MW}} t + \phi)\sigma_x. \tag{5.21}$$

Experiments at microwave frequencies make use of the rotating frame where $|\tilde{\psi}(t)\rangle = R_z(\omega_{\mathrm{MW}} t)\,|\psi(t)\rangle$. In our notation, the unitary operator $R_n(\alpha) = \exp(-i\alpha\hat{n}\cdot\vec{\sigma}/2)$ represents a positive rotation in the Bloch sphere about the unit vector $\hat{n} = (n_x, n_y, n_z)$ by an angle $\alpha$. The rotating frame Hamiltonian, neglecting fast oscillating terms, is given by:

$$\tilde{H} = R_z(\omega_{\mathrm{MW}} t) H R_z^{\dagger}(\omega_{\mathrm{MW}} t) + i\frac{dR_z(\omega_{\mathrm{MW}} t)}{dt} R_z^{\dagger}(\omega_{\mathrm{MW}} t) \tag{5.22}$$

$$= \frac{\Delta}{2}\sigma_z + \frac{\Omega}{2}(\cos\phi\sigma_x - \sin\phi\sigma_y), \tag{5.23}$$

where $\Delta = \omega_{\mathrm{MW}} - \omega_0$. During free evolution in the lab frame for a time $t$, $H_{\mathrm{free}} = -\frac{\omega_0}{2}\sigma_z$, and the state evolves with $U_{\mathrm{free}}(t) = R_z(-\omega_0 t)$. During free evolution in the rotating frame, $\tilde{H}_{\mathrm{free}} = \frac{\Delta}{2}\sigma_z$, and the state evolves with $\tilde{U}_{\mathrm{free}}(t) = R_z(\Delta t)$.

We use parity-mode Pauli spin blockade for measurement and take our observable as $O = (\mathbb{1} - \sigma_z \otimes \sigma_z)/2$ in all cases where $\mathbb{1}$ is the identity operator. We initialize using post-selection into the subspace spanned by $\{|01\rangle, |10\rangle\}$ (see Extended Data Fig. 8 for further discussion).

Regardless of whether the initial pair is entangled, mixed, or a product state, the following expectation values hold.

We can use a modified Ramsey sequence with a virtual detuning in order to precisely estimate the qubit frequency. After preparation of a superposition state via a gate applied to qubit $i$, an $R_z^i(\omega_{\text{virtual}}t)$ operation is performed via a reference frame update (in the case of resonant control) or a physical wait (in the case of baseband control) prior to measurement:

$$\text{Init} \rightarrow R_x^i(\pi/2) \rightarrow \text{Wait } t \rightarrow R_z^i(\omega_{\text{virtual}}t) \rightarrow R_x^i(-\pi/2) \rightarrow \text{Measure } O. \tag{5.24}$$

The expectation value of the time-ordered sequence is:

$$p_{\text{odd}}(t) = A\cos((\Delta + \omega_{\text{virtual}})t)\exp(-(t/T_2^*)^a) + B, \tag{5.25}$$

where $p_{\text{odd}}(t)$ is the probability of measuring a state in the $\{|01\rangle, |10\rangle\}$ subspace. $A$ and $B$ are visibility and offset corrections due to constant state preparation and measurement (SPAM) errors, $a$ is a decay constant and $T_2^*$ is the decay time. The frequency of the fitted oscillations $\omega_{\text{fit}}^*$ can be related to the Larmor frequency as:

$$\omega_0 = \omega_{\text{MW}} - (\omega_{\text{fit}}^* - \omega_{\text{virtual}}). \tag{5.26}$$

A similar analysis holds for a Hahn echo pulse sequence:

$$\text{Init} \rightarrow R_x^i(\pi/2) \rightarrow \text{Wait } t/2 \rightarrow R_x^i(\pi) \rightarrow \text{Wait } t/2 \rightarrow R_z^i(\omega_{\text{virtual}}t) \rightarrow \\ \rightarrow R_x^i(-\pi/2) \rightarrow \text{Measure } O. \tag{5.27}$$

The expectation value is given as:

$$p_{\text{odd}}(t) = C\cos((\Delta_2 - \Delta_1)/2 + \omega_{\text{virtual}})t)\exp(-(t/T_2^{\text{H}})^b) + D, \tag{5.28}$$

where $C$ and $D$ are once again due to SPAM errors, $b$ is a decay constant and $T_2^H$ is the extracted decay time. Here we observe that, contrary to expectation, the free evolution in the rotating frame with frequency $\Delta_1 = \omega_{\text{MW}} - \omega_{01}$ before the decoupling pulse may be measurably different than the free evolution with frequency $\Delta_2 = \omega_{\text{MW}} - \omega_{02}$ after the pulse. Fitting the decaying oscillations to a frequency $\omega_{\text{fit}}^H$ offers information about this systematic difference in Larmor frequency after the echo pulse, as any quasistatic fluctuations are eliminated by the echo pulse:

$$\omega_{01} - \omega_{02} = 2(\omega_{\text{fit}}^H - \omega_{\text{virtual}}). \tag{5.29}$$

An off-resonant pulse may be embedded into the second half of an echo sequence of fixed duration $T$ to probe the transient phase pickup $\theta_t(t_{\text{delay}})$ over time $t_{\text{delay}}$ as in Fig. 2. In this case, a gate $R_z^i(\theta)$ is swept prior to measurement:

$$\begin{aligned}\text{Init} \rightarrow R_x^i(\pi/2) \rightarrow \text{Wait } T/2 \rightarrow R_x^i(\pi) \rightarrow \text{Wait } T/2 - t_{\text{delay}} \rightarrow \text{Burst} \rightarrow \\ \rightarrow \text{Wait } t_{\text{delay}} \rightarrow R_z^i(\theta) \rightarrow R_x^i(\pi/2) \rightarrow \text{Measure } O.\end{aligned} \tag{5.30}$$

The expectation value is given as:

$$p_{\text{odd}}(\theta, t_{\text{delay}}) = E\cos(T(\Delta_2 - \Delta_1)/2 + \theta_t(t_{\text{delay}}) + \theta) + F, \tag{5.31}$$

where $E$ and $F$ account for the loss of visibility due to the echo decay as well as SPAM errors. As the difference $\Delta_2 - \Delta_1$ is known from the unmodified echo experiment, fitting the oscillation permits extracting $\theta_t$. In the rotating frame, $\theta_t = \int dt_{\text{delay}}\Delta(t_{\text{delay}})$, and it follows that $\omega_0(t_{\text{delay}}) = \omega_{\text{MW}} - d\theta_t/dt_{\text{delay}}$.

### 5.8.5. ESTIMATING THE INFIDELITY OF RESONANT QUBIT CONTROL

We may use the measured $T_2^*$ and $T_2^{\text{Rabi}}$ timescales to infer which error source contributes more to the resonant single-qubit gate fidelities as measured with randomized benchmarking presented in Fig. 5.2**a**.

First, we can consider quasi-static frequency fluctuations as captured by the $T_2^*$ coherence timescale. Assuming this is dominated by Gaussian quasi-static noise, the $T_2^*$ relates to the standard deviation $\sigma_f$ of the qubit frequency fluctuations as $\sigma_f = 1/\sqrt{2}\pi T_2^*$ [49]. Considering the Hamiltonian model for resonant qubit control in Equation 5.23 with $\phi = 0$, the fidelity of an imperfect unitary gate can be analytically derived in terms of the Rabi frequency $\Omega = 2\pi f_{\text{Rabi}}$ and detuning $\Delta \approx \sigma_f$ [50]:

$$F = \frac{d + |\text{Tr}(U_{\text{ideal}}^\dagger U_{\text{actual}})|^2}{d(d+1)}, \tag{5.32}$$

where $U_{\text{ideal}}$ is the desired unitary operation, $U_{\text{actual}}$ is the imperfect operation, and $d = 2$ is the dimension of the single-qubit Hilbert space. In the relevant limit where $\Delta \ll \Omega$, we find the error $\epsilon_{X90} = 1 - F_{X90}$ that originates from quasi-static frequency fluctuations as:

$$\epsilon_{X90}^* \approx \frac{1}{6\pi^2 f_{\text{Rabi}}^2 (T_2^*)^2}. \tag{5.33}$$

Similarly, we can consider the error that originates from decoherence while the qubit is subject to the driving field as captured by the $T_2^{\text{Rabi}}$ timescale or, equivalently, the quality factor $Q_{1Q} = 2f_{\text{Rabi}}T_2^{\text{Rabi}}$ conventionally expressed as the number of complete spin flips that fit within the coherence time. Considering exponential decay, the error originating from decoherence while driving is:

$$\epsilon_{X90}^{\text{Rabi}} \approx \frac{1}{2Q_{1Q}} = \frac{1}{4f_{\text{Rabi}}T_2^{\text{Rabi}}}. \tag{5.34}$$

**Table 5.2:** Comparing the Rabi frequency, $T_2^*$, $T_2^{\text{Rabi}}$, measured X90 gate error $\epsilon_{X90,\text{RB}}$, estimated X90 gate error due to quasi-static noise $\epsilon_{X90}^*$, and estimated X90 gate due to decoherence of the dressed qubit $\epsilon_{X90}^{\text{Rabi}}$.

| Qubit | $f_{\text{Rabi}}$ (MHz) | $T_2^*$ (μs) | $T_2^{\text{Rabi}}$ (μs) | $\epsilon_{X90,\text{RB}}$ (%) | $\epsilon_{X90}^*$ (%) | $\epsilon_{X90}^{\text{Rabi}}$ (%) |
|---|---|---|---|---|---|---|
| Q1 | 2.0412(7) | 3.31(9) | 16(1) | 0.33(2) | 0.037(2) | 0.78(5) |
| Q2 | 2.2413(9) | 2.02(2) | 15(1) | 0.20(2) | 0.082(2) | 0.74(7) |
| Q3 | 2.2685(9) | 3.57(8) | 14(1) | 0.61(8) | 0.026(1) | 0.77(6) |
| Q4 | 1.752(1) | 2.90(5) | 18(2) | 0.7(1) | 0.065(2) | 0.78(8) |

Table 5.2 shows the error estimates from fitting all 4 qubit properties including the measured error $\epsilon_{X90,\text{RB}} = 1 - F_{\text{avg}}^{\text{res}}$ of the primitive $X_{90}$ gate extracted from randomized benchmarking. We can see that the error estimate due to $T_2^{\text{Rabi}}$ decay is about an order of magnitude larger than that originating from quasi-static frequency fluctuations and of the same order as the error measured with randomized benchmarking. We therefore conclude that the $T_2^{\text{Rabi}}$ decay dominates the resonant single-qubit gate infidelity.

Lastly, we note that the estimates from Equations 5.33 and Equations 5.34 can change meaningfully depending on the exponents of the decay curves and the nature of the microscopic noise. Additionally, the qubit coherence properties were extracted at different points in time than the randomized benchmarking data, so some electrostatic drift could be anticipated. This likely accounts for why there is a discrepancy between the measured and estimated error rates, particularly for Q1 and Q2.

### 5.8.6. HOPPING SPIN CONTROL AND THE DIABATICITY CONDITION

Single-spin control via hopping spins can be understood starting from a Hamiltonian describing a single electron in a double quantum dot:

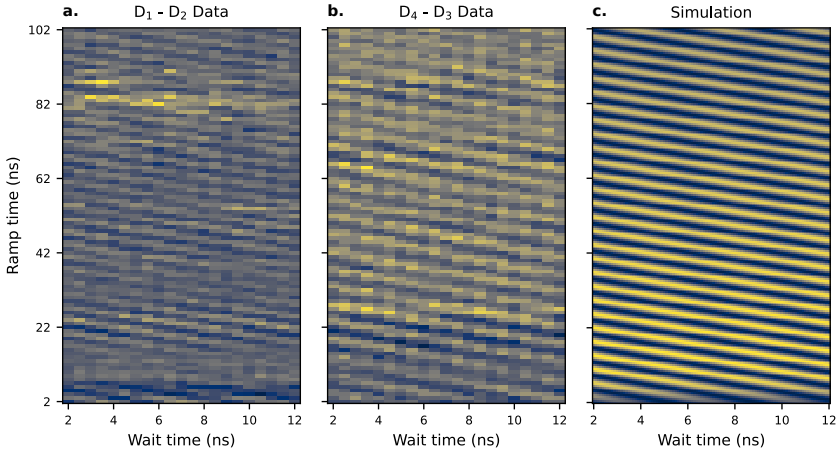




**Extended Data Fig 5.11: Spin Shuttling versus Ramp Time.** Observed spin fraction oscillations when shuttling between **a.** Dots $D_1$ and $D_2$ and **b.** Dots $D_4$ and $D_3$ with a varying ramp time. **c.** Simulation using parameters extracted from Pair 1-2 in experiment. A total detuning ramp of 300 mV is converted to 10 500 μeV with a combined lever arm of 0.07 meV/mV, and a tunnel coupling of 30 μeV is estimated. The measured qubit frequencies of 240 MHz and 270 MHz are used for the two dot positions along with a measured tip angle of 22°. The data in a-b) was collected with an external field of −15 mT. The simulations show that the sudden approximation for spin-state preservation during shuttling is reasonably met in our experiments over a large range of ramp times owing to the very large detuning sweep.

$$H_{\mathrm{DQD}} = H_{\mathrm{charge}} + H_{\mathrm{spin}} = \begin{pmatrix} \epsilon/2 & 0 & t_c & 0 \\ 0 & \epsilon/2 & 0 & t_c \\ t_c & 0 & -\epsilon/2 & 0 \\ 0 & t_c & 0 & -\epsilon/2 \end{pmatrix} + \tag{5.35}$$

$$\frac{g\mu_B}{2} \begin{pmatrix} B_{1,\mathrm{tot}} & 0 & 0 & 0 \\ 0 & -B_{1,\mathrm{tot}} & 0 & 0 \\ 0 & 0 & B_{2,\mathrm{tot}}\cos(\theta_{\mathrm{tip}}) & B_{2,\mathrm{tot}}\sin(\theta_{\mathrm{tip}})e^{-i\phi} \\ 0 & 0 & B_{2,\mathrm{tot}}\sin(\theta_{\mathrm{tip}})e^{i\phi} & -B_{2,\mathrm{tot}}\cos(\theta_{\mathrm{tip}}) \end{pmatrix}, \tag{5.36}$$

where $\epsilon$ and $t_c$ are the detuning and tunnel coupling describing the double dot system. In the second term, the Zeeman energies at the two sites are considered where $\theta_{\mathrm{tip}}$ is the polar angle between the two

quantization axes and $\phi$ is the azimuthal angle. This model is directly analogous to the one employed in [24, 25] with the difference that the tip in quantization is attributed to the magnetic field as opposed to the $g$-tensor. As we are only interested in single-spin physics, we may take $\phi = 0$ with an appropriate choice of coordinate frame.

Fig. 4b) plots the eigenenergies of Equation 5.35. When the detuning is linearly swept $\epsilon(t) = vt$, the Landau-Zener formula provides a means to estimate the condition for which charge transfer between the two dots is not adiabatic:

$$P_{\mathrm{LZ}} = \exp\left(\frac{-2\pi t_c^2}{\hbar v}\right). \tag{5.37}$$

Based on a combined vP1+vP2 lever arm of about 0.07 meV/mV and a ramp time of 5 ns, we estimate a detuning ramp speed of about $v = 3000\,\mu\mathrm{eV/ns}$. With an estimated tunnel coupling of 40 µeV, we roughly estimate that $0.001 < P_{\mathrm{LZ}} \approx 0.01$. We discuss the implications of this shortly.

Assuming the electron charge is transferred adiabatically, the resulting spin physics is clarified by transforming to the diagonal basis of $H_{\mathrm{charge}}$ with a unitary $U = \exp\left(-i\tan^{-1}(-2t_c/\epsilon)\,\sigma_y \otimes \sigma_0\right)$ and investigating $H' = UH_{\mathrm{spin}}U^\dagger$ in the sector corresponding to a ground charge state:

$$\begin{aligned} H' = \frac{g\mu_B}{4}\Bigg[ & \left( B_{1,\mathrm{tot}} \left( 1 - \frac{\epsilon}{\sqrt{\epsilon^2 + 4t_c^2}} \right) \right. \\ & \left. + B_{2,\mathrm{tot}} \cos\theta_{\mathrm{tip}} \left( 1 + \frac{\epsilon}{\sqrt{\epsilon^2 + 4t_c^2}} \right) \right) \sigma_z \\ & + \left( B_{2,\mathrm{tot}} \sin\theta_{\mathrm{tip}} \left( 1 + \frac{\epsilon}{\sqrt{\epsilon^2 + 4t_c^2}} \right) \right) \sigma_x \Bigg] \end{aligned} \tag{5.38}$$

Fig. 4c) plots the components of Equation 5.38. A clear detuning-dependent step arises that is not evident from inspecting the energy level diagram alone. The sudden approximation quantifies how quickly such a Hamiltonian step needs to be traversed in order for the initial quantum state to be preserved:

$$t \ll \frac{2\pi\hbar}{\Delta E}, \tag{5.39}$$

where $\Delta E \approx 0.1\,\mu\mathrm{eV}$ is the difference between the relevant eigenvalues of $H'$. This suggests the time interval needs to be less than 1 ns.

As the energetic width of the step is about $4t_c$ for the case of our linear detuning ramp, the step is crossed in about 60 ps. In fact, even a total ramp time much longer than was used for the logical gate implementation may be sufficient. This is observed in Fig. 5.11 where ramp times extending to several tens of nanoseconds were used while still observing evidence of sudden spin state transfer between both dot pairs $D_1D_2$ and $D_3D_4$. Simulations of the time-dependent Schrodinger equation with estimates of experimental parameters corroborate this. We remark that certain ramp times are nontrivially associated with oscillations of different visibility. For example 12 µs ramps consistently resulted in poor visibility despite longer ramps of 22 µs showing higher visibility. The origin of this effect is unknown to us, but it may be related to the microscopic valley-orbit structure of the double-dot system.

The estimated 0.1-1% probability of a diabatic transition at the charge anticrossing is one of the main limitations for the maximum single-qubit gate fidelity that we achieved via hopping spins. This was due to a particularly limited window of device stability within which DC voltages could be tuned to either increase the tunnel coupling or decrease the detuning range necessary to shuttle the electron. Equation 5.37 and Equation 5.39 represent a fundamental trade-off, as we desire an adiabatic charge transition with a diabatic spin transition. However, the exponential dependence of the Landau-Zener formula implies that even a modest increase of tunnel coupling greatly enhances the quality of charge transfer while still safely satisfying the sudden approximation. Furthermore, the increased susceptibility to charge noise that occurs when the spin and charge are maximally hybridized means that a fast shuttling time is preferable.

As the micromagnet design and gate layout in the present device was not intended for electron shuttling, there is almost certainly substantial room for improved fidelities by tailoring device design to the conditions for performing shuttling gates. Building upon the understanding of the depolarization of the micromagnet under low-field conditions, engineering quantum axis tips well above 45 degrees between adjacent dots should be easily achievable while keeping qubit frequencies on the order of 100 MHz. Furthermore, being able to modulate the tunnel coupling to the range of 50 µeV to 100 µeV would substantially improve the quality of adiabatic charge shuttling and should lead to enhanced gate operation.

### 5.8.7. ESTIMATING LEAKAGE WITH BLIND RANDOMIZED BENCHMARKING

In Fig. 5.12, we present two examples of the blind RB fitting protocol described in the Methods. The two datasets used were calibrated when different Larmor frequencies and tip angles were implemented in the

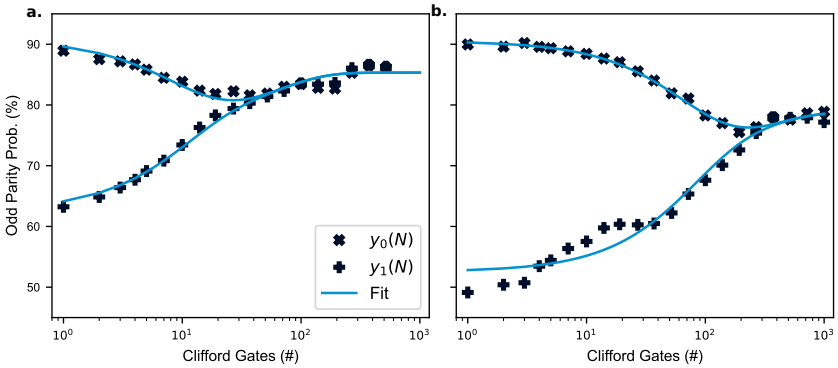


**Extended Data Fig 5.12: Blind Randomized Benchmarking.** **a.** Randomized benchmarking performed when the tunnel coupling is estimated to be approximately 18 μeV. Fitting to the blind RB theory results in $A = 0.853$, $B = 0.141$, $C = -0.086$, $p = 0.098$ and $q = 0.017$ and yields a leakage rate of $\Gamma = 1.0(2)\%$, a total error rate of $\epsilon = 5.4(2)\%$, and a qubit error rate of $\epsilon = 4.4(2)\%$ for a Clifford gate fidelity estimate of 94.6(2)%. Each decay curve is the average of 250 random Clifford circuits. **b.** Randomized benchmarking performed when the tunnel coupling is estimated to be approximately 48 μeV. Fitting to the blind RB theory results in $A = 0.788$, $B = 0.190$, $C = -0.073$, $p = 0.013$ and $q = 0.003$ and yields a leakage rate of $\Gamma = 0.13(5)\%$, a total error rate of $\epsilon = 0.74(5)\%$, and a qubit error rate of $\epsilon = 0.61(5)\%$ for a Clifford gate fidelity estimate of 99.26(5)%. Each decay curve is the average of 250 random Clifford circuits.

dots, so the two results cannot be compared directly. However, the hopping gate tune-up procedure was the same in both cases. The data in Fig. 5.12**a** was taken when the virtual barrier $vB12$ was approximately 100 mV lower than in Fig. 5.12**b**, which is the same data presented in Fig 5.4**f** of the main text, and we estimate the tunnel coupling between dots to be 18 μeV and 48 μeV in the two cases respectively. The hopping gate suffers from substantially worse leakage when the tunnel coupling is lower, and the blind RB protocol estimates this error to be an order of magnitude lower when the tunnel coupling is raised to the condition where the best hopping gate fidelity was achieved in this device. The Clifford gate fidelity extracted from Fig. 5.12**b** is estimated to be 99.52(9)%, which is comparable to the values of 99.01(11)% and 99.49(7)% obtained from standard RB fits for the odd and even parity decay curves respectively.

Blind RB offers limited information about where the state is leaking. In all instances of randomized benchmarking that exhibited signs of leakage, the trend converges towards the odd spin parity signal (i.e. a

(2,0) charge state measurement). One explanation consistent with this observation is leakage to excited valley-orbit states. In the discussion in Section 5.8.6, we did not discuss the role that the valley-orbit state plays in the shuttling physics. Although diabatic passage through the charge avoided crossing may impede charge transfer, it is also possible that the charge does tunnel between dots but excites into a higher valley-like state. If, at the end of the random Clifford circuit, the charge state is excited to a different valley-orbit state, it is possible that Pauli spin blockade is lifted, resulting in tunnelling to the (2,0) charge state during readout.

# REFERENCES


[1] F. K. Unseld, B. Undseth, E. Raymenants, Y. Matsumoto, S. L. de Snoo, S. Karwal, O. Pietx-Casas, A. S. Ivlev, M. Meyer, A. Sammak, M. Veldhorst, G. Scappucci, and L. M. K. Vandersypen. *Baseband control of single-electron silicon spin qubits in two dimensions*. 2024. doi: 10.48550/ARXIV.2412.05171.

[2] R. Maurand, X. Jehl, D. Kotekar-Patil, A. Corna, H. Bohuslavskyi, R. Laviéville, L. Hutin, S. Barraud, M. Vinet, M. Sanquer, and S. De Franceschi. "A CMOS silicon spin qubit". In: *Nature Communications* 7.1 (Nov. 2016). doi: 10.1038/ncomms13575.

[3] A. M. J. Zwerver, T. Krähenmann, T. F. Watson, L. Lampert, H. C. George, R. Pillarisetty, S. A. Bojarski, P. Amin, S. V. Amitonov, J. M. Boter, R. Caudillo, D. Correas-Serrano, J. P. Dehollain, G. Droulers, E. M. Henry, R. Kotlyar, M. Lodari, F. Lüthi, D. J. Michalak, B. K. Mueller, S. Neyens, J. Roberts, N. Samkharadze, G. Zheng, O. K. Zietz, G. Scappucci, M. Veldhorst, L. M. K. Vandersypen, and J. S. Clarke. "Qubits made by advanced semiconductor manufacturing". In: *Nature Electronics* 5.3 (Mar. 2022), pp. 184–190. doi: 10.1038/s41928-022-00727-9.

[4] S. Neyens, O. K. Zietz, T. F. Watson, F. Luthi, A. Nethwewala, H. C. George, E. Henry, M. Islam, A. J. Wagner, F. Borjans, E. J. Connors, J. Corrigan, M. J. Curry, D. Keith, R. Kotlyar, L. F. Lampert, M. T. Mądzik, K. Millard, F. A. Mohiyaddin, S. Pellerano, R. Pillarisetty, M. Ramsey, R. Savytskyy, S. Schaal, G. Zheng, J. Ziegler, N. C. Bishop, S. Bojarski, J. Roberts, and J. S. Clarke. "Probing single electrons across 300-mm spin qubit wafers". In: *Nature* 629.8010 (May 2024), pp. 80–85. doi: 10.1038/s41586-024-07275-6.

[5] P. Steinacker, N. D. Stuyck, W. H. Lim, T. Tanttu, M. Feng, A. Nickl, S. Serrano, M. Candido, J. D. Cifuentes, F. E. Hudson, K. W. Chan, S. Kubicek, J. Jussot, Y. Canvel, S. Beyne, Y. Shimura, R. Loo, C. Godfrin, B. Raes, S. Baudot, D. Wan, A. Laucht, C. H. Yang, A. Saraiva, C. C. Escott, K. D. Greve, and A. S. Dzurak. *A 300 mm foundry silicon spin qubit unit cell exceeding 99% fidelity in all operations*. 2024.

[6] T. Huckemann, P. Muster, W. Langheinrich, V. Brackmann, M. Friedrich, N. D. Komerički, L. K. Diebel, V. Stieß, D. Bougeard, C. Dahl, L. R. Schreiber, and H. Bluhm. *Industrially fabricated single-electron quantum dots in Si/Si-Ge heterostructures*. 2024.

[7] X. Xue, M. Russ, N. Samkharadze, B. Undseth, A. Sammak, G. Scappucci, and L. M. K. Vandersypen. "Quantum logic with spin qubits crossing the surface code threshold". In: *Nature* 601.7893 (Jan. 2022), pp. 343–347. doi: 10.1038/s41586-021-04273-w.

[8] A. Noiri, K. Takeda, T. Nakajima, T. Kobayashi, A. Sammak, G. Scappucci, and S. Tarucha. "Fast universal quantum gate above the fault-tolerance threshold in silicon". In: *Nature* 601.7893 (Jan. 2022), pp. 338–342. doi: 10.1038/s41586-021-04182-y.

[9] A. Mills, C. Guinn, M. Feldman, A. Sigillito, M. Gullans, M. Rakher, J. Kerckhoff, C. Jackson, and J. Petta. "High-Fidelity State Preparation, Quantum Control, and Readout of an Isotopically Enriched Silicon Spin Qubit". In: *Physical Review Applied* 18.6 (Dec. 2022). doi: 10.1103/physrevapplied.18.064028.

[10] S. G. J. Philips, M. T. Mądzik, S. V. Amitonov, S. L. de Snoo, M. Russ, N. Kalhor, C. Volk, W. I. L. Lawrie, D. Brousse, L. Tryputen, B. P. Wuetz, A. Sammak, M. Veldhorst, G. Scappucci, and L. M. K. Vandersypen. "Universal control of a six-qubit quantum processor in silicon". In: *Nature* 609.7929 (Sept. 2022), pp. 919–924. doi: 10.1038/s41586-022-05117-x.

[11] K. Takeda, A. Noiri, T. Nakajima, L. C. Camenzind, T. Kobayashi, A. Sammak, G. Scappucci, and S. Tarucha. "Rapid single-shot parity spin readout in a silicon double quantum dot with fidelity exceeding 99%". In: *npj Quantum Information* 10.1 (Feb. 2024). doi: 10.1038/s41534-024-00813-0.

[12] M. De Smet, Y. Matsumoto, A.-M. J. Zwerver, L. Tryputen, S. L. de Snoo, S. V. Amitonov, A. Sammak, N. Samkharadze, Ö. Gül, R. N. M. Wasserman, M. Rimbach-Russ, G. Scappucci, and L. M. K. Vandersypen. *High-fidelity single-spin shuttling in silicon*. 2024. doi: 10.48550/ARXIV.2406.07267.

[13] R. Neumann and L. R. Schreiber. "Simulation of micro-magnet stray-field dynamics for spin qubit manipulation". In: *Journal of Applied Physics* 117.19 (May 2015), p. 193903. doi: 10.1063/1.4921291.

[14] J. Yoneda, T. Otsuka, T. Takakura, M. Pioro-Ladrière, R. Brunner, H. Lu, T. Nakajima, T. Obata, A. Noiri, C. J. Palmstrøm, A. C. Gossard, and S. Tarucha. "Robust micromagnet design for fast electrical manipulations of single spins in quantum dots". In: *Applied Physics*

5

*Express* 8.8 (July 2015), p. 084401. doi: 10.7567/apex.8.084401.

[15] N. I. Dumoulin Stuyck, F. A. Mohiyaddin, R. Li, M. Heyns, B. Govoreanu, and I. P. Radu. “Low dephasing and robust micromagnet designs for silicon spin qubits”. In: *Applied Physics Letters* 119.9 (Aug. 2021), p. 094001. doi: 10.1063/5.0059939.

[16] H. C. George, M. T. Mądzik, E. M. Henry, A. J. Wagner, M. M. Islam, F. Borjans, E. J. Connors, J. Corrigan, M. Curry, M. K. Harper, D. Keith, L. Lampert, F. Luthi, F. A. Mohiyaddin, S. Murcia, R. Nair, R. Nahm, A. Nethwewala, S. Neyens, B. Patra, R. D. Raharjo, C. Rogan, R. Savytskyy, T. F. Watson, J. Ziegler, O. K. Zietz, S. Pellerano, R. Pillarisetty, N. C. Bishop, S. A. Bojarski, J. Roberts, and J. S. Clarke. “12-Spin-Qubit Arrays Fabricated on a 300 mm Semiconductor Manufacturing Line”. In: *Nano Letters* 25.2 (Dec. 2024), pp. 793–799. doi: 10.1021/acs.nanolett.4c05205.

[17] C. Jones, M. A. Fogarty, A. Morello, M. F. Gyure, A. S. Dzurak, and T. D. Ladd. “Logical Qubit in a Linear Array of Semiconductor Quantum Dots”. In: *Phys. Rev. X* 8 (2 June 2018), p. 021058. doi: 10.1103/PhysRevX.8.021058.

[18] M. Tadokoro, T. Nakajima, T. Kobayashi, K. Takeda, A. Noiri, K. Tomari, J. Yoneda, S. Tarucha, and T. Kodera. “Designs for a two-dimensional Si quantum dot array with spin qubit addressability”. In: *Scientific Reports* 11.1 (Sept. 2021). doi: 10.1038/s41598-021-98212-4.

[19] M. Aldeghi, R. Allenspach, A. Vervelaki, D. Jetter, K. Bagani, F. Braakman, M. Poggio, and G. Salis. *Simulation and measurement of stray fields for the manipulation of spin-qubits in one- and two-dimensional arrays*. 2024.

[20] S. Freer, S. Simmons, A. Laucht, J. T. Muhonen, J. P. Dehollain, R. Kalra, F. A. Mohiyaddin, F. E. Hudson, K. M. Itoh, J. C. McCallum, D. N. Jamieson, A. S. Dzurak, and A. Morello. “A single-atom quantum memory in silicon”. In: *Quantum Science and Technology* 2.1 (Mar. 2017), p. 015009. doi: 10.1088/2058-9565/aa63a4.

[21] K. Takeda, J. Yoneda, T. Otsuka, T. Nakajima, M. R. Delbecq, G. Allison, Y. Hoshi, N. Usami, K. M. Itoh, S. Oda, T. Kodera, and S. Tarucha. “Optimized electrical control of a Si/SiGe spin qubit in the presence of an induced frequency shift”. In: *npj Quantum Information* 4.1 (Oct. 2018). doi: 10.1038/s41534-018-0105-z.

[22] B. Undseth, O. Pietx-Casas, E. Raymenants, M. Mehmandoost, M. T. Madzik, S. G. J. Philips, S. L. de Snoo, D. J. Michalak, S. V. Amitonov, L. Tryputen, B. P. Wuetz, V. Fezzi, D. D. Esposti, A. Sammak, G. Scappucci, and L. M. Vandersypen. “Hotter is Easier: Unexpected Temperature Dependence of Spin Qubit Frequencies”. In: *Physical Review X* 13.4 (Oct. 2023). doi: 10.1103/physrevx.13.041015.

[23] T. Tanttu, W. H. Lim, J. Y. Huang, N. Dumoulin Stuyck, W. Gilbert, R. Y. Su, M. Feng, J. D. Cifuentes, A. E. Seedhouse, S. K. Seritan, C. I. Ostrove, K. M. Rudinger, R. C. C. Leon, W. Huang, C. C. Escott, K. M. Itoh, N. V. Abrosimov, H.-J. Pohl, M. L. W. Thewalt, F. E. Hudson, R. Blume-Kohout, S. D. Bartlett, A. Morello, A. Laucht, C. H. Yang, A. Saraiva, and A. S. Dzurak. “Assessment of the errors of high-fidelity two-qubit gates in silicon quantum dots”. In: *Nature Physics* 20.11 (Aug. 2024), pp. 1804–1809. doi: 10.1038/s41567-024-02614-w.

[24] F. van Riggelen-Doelman, C.-A. Wang, S. L. de Snoo, W. I. L. Lawrie, N. W. Hendrickx, M. Rimbach-Russ, A. Sammak, G. Scappucci, C. Déprez, and M. Veldhorst. “Coherent spin qubit shuttling through germanium quantum dots”. In: *Nature Communications* 15.1 (July 2024). doi: 10.1038/s41467-024-49358-y.

[25] C.-A. Wang, V. John, H. Tidjani, C. X. Yu, A. S. Ivlev, C. Déprez, F. van Riggelen-Doelman, B. D. Woods, N. W. Hendrickx, W. I. L. Lawrie, L. E. A. Stehouwer, S. D. Oosterhout, A. Sammak, M. Friesen, G. Scappucci, S. L. de Snoo, M. Rimbach-Russ, F. Borsoi, and M. Veldhorst. “Operating semiconductor quantum processors with hopping spins”. In: *Science* 385.6707 (July 2024), pp. 447–452. doi: 10.1126/science.ado5915.

[26] F. K. Unseld, M. Meyer, M. T. Madzik, F. Borsoi, S. L. de Snoo, S. V. Amitonov, A. Sammak, G. Scappucci, M. Veldhorst, and L. M. K. Vandersypen. “A 2D quantum dot array in planar 28Si/SiGe”. In: *Applied Physics Letters* 123.8 (Aug. 2023). doi: 10.1063/5.0160847.

[27] M. Mehmandoost and V. V. Dobrovitski. “Decoherence induced by a sparse bath of two-level fluctuators: 1/*f* noise in high-quality qubits”. In: *Physical Review Research* 6.3 (Aug. 2024). doi: 10.1103/physrevresearch.6.033175.

[28] L. Cvitkovich, P. Stano, C. Wilhelmer, D. Waldhör, D. Loss, Y.-M. Niquet, and T. Grasser. *Coherence limit due to hyperfine interaction with nuclei in the barrier material of Si spin qubits*. 2024. doi: 10.48550/ARXIV.2405.10667.

[29] Y. Choi and R. Joynt. “Interacting random-field dipole defect model for heating in semiconductor-based qubit devices”. In: *Physical Review Research* 6.1 (Feb. 2024). doi: 10.1103/physrevresearch.6.013168.

[30] J. D. Teske, F. Butt, P. Cerfontaine, G. Burkard, and H. Bluhm. “Flopping-mode electron dipole spin resonance in the strong-driving regime”. In: *Physical Review B* 107.3 (Jan. 2023). doi: 10.1103/physrevb.107.035302.

[31] R. W. Andrews, C. Jones, M. D. Reed, A. M. Jones, S. D. Ha, M. P. Jura, J. Kerckhoff, M. Levendorf, S. Meenehan, S. T. Merkel, A. Smith, B. Sun, A. J. Weinstein, M. T. Rakher, T. D. Ladd, and M. G. Borselli. “Quantifying error and leakage in an encoded Si/SiGe triple-dot qubit”. In: *Nature Nanotechnology* 14.8 (July 2019), pp. 747–750. doi: 10.1038/s41565-019-0500-4.

[32] M. Aldeghi, R. Allenspach, and G. Salis. “Modular nanomagnet design for spin qubits confined in a linear chain”. In: *Applied Physics Letters* 122.13 (Mar. 2023). doi: 10.1063/5.0139670.

[33] F. Forster, M. Mühlbacher, D. Schuh, W. Wegscheider, and S. Ludwig. “Electric-dipole-induced spin resonance in a lateral double quantum dot incorporating two single-domain nanomagnets”. In: *Phys. Rev. B* 91 (19 May 2015), p. 195417. doi: 10.1103/PhysRevB.91.195417.

[34] F. Bersano, M. Aldeghi, N. Martinolli, V. Boureau, T. Aboud, M. Ghini, P. Scarlino, G. Salis, and A. M. Ionescu. *Integration of Cobalt Ferromagnetic Control Gates for Electrical and Magnetic Manipulation of Semiconductor Quantum Dots*. 2024.

[35] W. Legrand, S. Lopes, Q. Schaeverbeke, F. Montaigne, and M. Desjardins. “Optimal design of nanomagnets for on-chip field gradients”. In: *Physical Review Applied* 20.4 (Oct. 2023). doi: 10.1103/physrevapplied.20.044062.

[36] M. J. Donahue and D. G. Porter. *OOMMF user’s guide, version 1.0*. National Institute of Standards and Technology, Gaithersburg, MD, 1999. doi: 10.6028/nist.ir.6376.

[37] F. Ginzel, A. R. Mills, J. R. Petta, and G. Burkard. “Spin shuttling in a silicon double quantum dot”. In: *Physical Review B* 102.19 (Nov. 2020). doi: 10.1103/physrevb.102.195418.

[38] X. Zhao and X. Hu. *Coherent electron transport in silicon quantum dots*. 2019.

[39] B. Buonacorsi, B. Shaw, and J. Baugh. “Simulated coherent electron shuttling in silicon quantum dots”. In: *Physical Review B* 102.12 (Sept. 2020). doi: 10.1103/physrevb.102.125406.

[40] M. Rimbach-Russ, S. G. J. Philips, X. Xue, and L. M. K. Vandersypen. “Simple framework for systematic high-fidelity gate operations”. In: *Quantum Science and Technology* 8.4 (Sept. 2023), p. 045025. doi: 10.1088/2058-9565/acf786.

[41] D. Degli Esposti, L. E. A. Stehouwer, Ö. Gül, N. Samkharadze, C. Déprez, M. Meyer, I. N. Meijer, L. Tryputen, S. Karwal, M. Botifoll, J. Arbiol, S. V. Amitonov, L. M. K. Vandersypen, A. Sammak, M. Veldhorst, and G. Scappucci. “Low disorder and high valley splitting in silicon”. In: *npj Quantum Information* 10.1 (Mar. 2024). doi: 10.1038/s41534-024-00826-9.

[42] Y.-Y. Liu, S. Philips, L. Orona, N. Samkharadze, T. McJunkin, E. MacQuarrie, M. Eriksson, L. Vandersypen, and A. Yacoby. “Radio-Frequency Reflectometry in Silicon-Based Quantum Dots”. In: *Physical Review Applied* 16.1 (July 2021). doi: 10.1103/physrevapplied.16.014057.

[43] X. Xue, T. F. Watson, J. Helsen, D. R. Ward, D. E. Savage, M. G. Lagally, S. N. Coppersmith, M. A. Eriksson, S. Wehner, and L. M. K. Vandersypen. “Benchmarking Gate Fidelities in a Si/SiGe Two-Qubit Device”. In: *Phys. Rev. X* 9 (2 Apr. 2019), p. 021011. doi: 10.1103/PhysRevX.9.021011.

[44] L. DiCarlo, H. J. Lynch, A. C. Johnson, L. I. Childress, K. Crockett, C. M. Marcus, M. P. Hanson, and A. C. Gossard. “Differential Charge Sensing and Charge Delocalization in a Tunable Double Quantum Dot”. In: *Physical Review Letters* 92.22 (June 2004). doi: 10.1103/physrevlett.92.226801.

[45] M. Pioro-Ladrière, T. Obata, Y. Tokura, Y.-S. Shin, T. Kubo, K. Yoshida, T. Taniyama, and S. Tarucha. “Electrically driven single-electron spin resonance in a slanting Zeeman field”. In: *Nature Physics* 4.10 (Aug. 2008), pp. 776–779. doi: 10.1038/nphys1053.

[46] J. Yoneda, K. Takeda, T. Otsuka, T. Nakajima, M. R. Delbecq, G. Allison, T. Honda, T. Kodera, S. Oda, Y. Hoshi, N. Usami, K. M. Itoh, and S. Tarucha. “A quantum-dot spin qubit with coherence limited by charge noise and fidelity higher than 99.9%”. In: *Nature Nanotechnology* 13.2 (Dec. 2017), pp. 102–106. doi: 10.1038/s41565-017-0014-x.

[47] T. Tanttu, B. Hensen, K. W. Chan, C. H. Yang, W. W. Huang, M. Fogarty, F. Hudson, K. Itoh, D. Culcer, A. Laucht, A. Morello, and A. Dzurak. “Controlling Spin-Orbit Interactions in Silicon Quantum Dots Using Magnetic Field Direction”. In: *Physical Review X* 9.2 (May 2019). doi: 10.1103/physrevx.9.021028.

[48] M. Ortner and L. G. C. Bandeira. “Magpylib: A free Python package for magnetic field computation”. In: *SoftwareX* 11 (2020), p. 100466. doi: https://doi.org/10.1016/j.softx.2020.100466.

[49] R. Hanson, L. P. Kouwenhoven, J. R. Petta, S. Tarucha, and L. M. K. Vandersypen. “Spins in few-electron quantum dots”. In: *Reviews of Modern Physics* 79.4 (Oct. 2007), pp. 1217–1265. doi: 10.1103/revmodphys.79.1217.

[50] M. A. Nielsen. “A simple formula for the average gate fidelity of a quantum dynamical operation”. In: *Physics Letters A* 303.4 (Oct. 2002), pp. 249–252. doi: 10.1016/s0375-9601(02)01272-0.

# 6

# OUTLOOK

*You don’t have to see the whole staircase,*
*just take the first step.*

Martin Luther King Jr.

Since the beginning of this PhD Degree the field of spin qubits in semiconductor quantum dots saw tremendous progress. Qubit arrays have scaled from two to twelve - albeit not fully connected - qubits while high-fidelity initialisation, single-qubit gates and two-qubit gates were extensively demonstrated [1–6]. Good progress was made in the realization of long-range coupling and spin shuttling as well [7–9]. Parallel to that, industrial efforts are picking up. Their approach to this field enabled studies that look at devices on a statistically relevant scale are giving insights that go beyond early academic prototypes [10].

But, challenges remain. Most Si/SiGe devices are still linear chains, with inherently limited connectivity. The detrimental impact of low valley splittings seems unavoidable in large arrays. On another level, doubts around the scalability of popular EDSR techniques have become more prominent. Proposals mitigating each aspect exist but often come with new caveats; this thesis, with its focus on 2D-arrays and baseband control is no exception.

## SCALING TWO DIMENSIONAL ARRAYS



Scaling in the second dimension can be considered crucial to implement a large scale system. The improved connectivity and higher density reduces constrains on quantum algorithms and error correcting codes. As Chapter 4 shows, most parameters and concepts relating charge properties can readily be transferred from a linear chain to a 2D array. Gate pitches and dimensions require none or only small adjustments. Tunnel coupling control using barrier gates can also be implemented, though more extensive crosstalk calibration is required. While the gate layout used in Chapter 4 would warrant a centre gate to suppress unintentional diagonal tunnel coupling, studies with adjusted gate designs have shown this to be unnecessary [11].

On the other hand, more significant changes to the fabrication processes will become necessary as the second dimension becomes larger. An increasing number of gate layers are required to form quantum dots in the centre of the array. In cases of gate metals like Ti/Pd, additional ALD grown oxide layers reduce lever arms of gates in higher layers. Including or modifying etching steps can alleviate this issue by removing unnecessary parts of oxide layers at the quantum dot region. Alternatively gate metals that form a native oxide and bypass ALD layers like Al can be used to avoid this issue entirely.

Scaling in a second dimension also exacerbates climbing issues. Gates fanning out from the centre have to climb over more and more metal layers. To preserve electrical continuity, higher metal layers are typically thickened, but this approach is constrained by the need to maintain certain aspect ratios (height-to-width) for structural integrity. Inherently, the gate width is limited by the quantum dot size and pitch, which

ultimately restricts the possible thickness.

In contrast, industrial 3D fabrication techniques circumvent these limitations entirely. As demonstrated in studies such as [1, 11–13], multi-layer interconnects can be fanned out using stacked vias and chemical-mechanical polishing (CMP) processes, enabling all gates to be fabricated within the first metallic layer. Shared control, where multiple barrier or plunger gates are connected, also eases fabrication constraints but it relies heavily on the uniformity of the heterostructure and gate stack [14].

While the fabrication of larger quantum dot arrays seems challenging but manageable, more difficulties arise when implementing qubits using EDSR control. Linear quantum dot arrays position the qubits in a sweet line reducing susceptibility to charge noise. Two dimensional arrays by definition will deviate from it and thus face an increased decoherence gradient. Changes to the micromagnet design can mitigate this at the cost of a reduction in driving gradient and addressability as highlighted in Fig. 5.9**a-d**.

However, experimental observations from Chapter 5.2 reveal a surprising resilience in 2D scalability. Coherence times, Rabi driving frequencies, and qubit addressability in the 2x2 array remained almost on par with comparable linear arrays [5]. While we cannot rule out a potential misalignment of the quantum dots and the sweet line of the micromagnet in [5], a more likely explanation is that field gradients and coupled effects are not yet the limiting factors. This hypothesis is further supported by the data in Fig. 5.3, where a reduction of the decoherence gradient does not affect $T_2^*$.



A second consideration regarding micromagnets is their vertical distance to the qubits. Additional gate layers or vertical fanouts increase the distance of the micromagnet to the quantum dot layer, thus, reducing the field strength and gradients. While this would improve the decoherence gradient, driving gradients and spectral separation suffer.

The utilization of microwave signals introduces additional complexities. Achieving effective spatial addressability - for instance, to enable frequency reuse - requires microwave signals to be localized. As demonstrated in Section 5.2, a single screening gate can coherently drive all spins within the entire $2\times2$ qubit array. The observed driving speeds (see Fig. 5.2) show no correlation with the qubits' proximity to the gate. This observation underscores the critical need for enhanced microwave hygiene measures as the fall off of the electric field appears to be more than compensated by other effects such as changes in the confinement potential and differences in the local magnetic field gradients.

Further complications are microwave-induced heating effects, particularly PIRS. The time-dependent nature and nonlinear characteristics of PIRS render straightforward calibration and compensation protocols

impractical. Moreover, PIRS effects seem to differ fundamentally from general temperature-induced frequency shifts (see Chapter 5), raising significant questions about their underlying physical origin.

Working at elevated temperatures seems promising for a multitude of reasons, including the mitigation of PIRS. As shown in [15, 16] and Fig. 5.3**b** at higher temperatures the microwave induced phase pick up diminishes. Increasing the temperature also enables the use of more efficient cooling processes. The increased cooling power reduces constraints on the power dissipation of integrated or adjacent electronic components [17–19].

But working at elevated temperatures also has downsides. Increased charge noise enhances decoherence as shown in Fig. 5.5. Thermal broadening of reservoirs increases error rates of readout methods based on Elzerman readout. While PSB offers an alternative that is less sensitive to temperature, we still struggle to consistently tune up high-fidelity initialisation and readout based on it (see Fig. 5.8). Furthermore, both techniques still rely on a charge sensor. The typical SETs are also affected by temperature, reducing their sensitivity.

But even at low temperatures the integration of charge sensors is problematic for large and especially for dense two-dimensional arrays. The required space for a SET and its ohmic contact(s) is massive compared to its sensitivity range. These challenges make gate-based dispersive readout an appealing alternative. While current implementations are still limited in their performance and require large resonators the ability to readout without requiring space inside the quantum dot array is yet unparalleled. Hybrid models where gate-based dispersive readout is used for the centre and SETs for edge areas might make a compelling combination. Shifting the definition of the centre and edge area allows for a flexible allocation of resources depending on advancements of each technique.



### BASEBAND QUBIT CONTROL

The issues of EDSR control can be circumvented by using different encodings such as ST qubits and EO qubits. Both encodings allow to operate the qubits exclusively with baseband pulses alleviating all microwave related issues. EO qubits or material changes are able to take this one step further dropping also the need of a micromagnet. These encodings, however, use multiple spins to realize a qubit. The Hilbert space spanned by the ensemble of spins is, however, larger than the Hilbert space required to encode a single qubit. The collective spin is able to access states that are not part of the qubit, also known as leakage states. Aside relaxation and dephasing ST and EO qubits need to address this additional error. Using multiple spins to encode a qubit also creates additional overhead during operation i.e. requiring more

pulses to implement gates.

As shown by Wang et al. in [20] and in Chapter 5 it is also possible to operate single-spin qubits with baseband pulses. By transferring or hopping the spin qubit between quantum dots with different quantisation axes an effective rotation can be implemented. Crucially, this transfer must be diabatic with respect to spin while remaining adiabatic for the charge to ensure coherent manipulation. A higher Larmor frequency reduces the gate time for a given quantisation axis tilt. However, it also increases the timing precision of the baseband pulses which needs to be significantly smaller than the period of the spin precession.

This implementation of single-qubit gates changes the requirements for magnetic structures compared to designs for EDSR control drastically. By eliminating the need for driving and addressability gradient, the trade-off between qubit selectivity and decoherence is avoided. A tilt in the magnetic field direction between dots is added as requirement, but it poses no restriction on the decoherence gradient, enabling a constraint-free minimization.

While Section 5.4 proposes one architecture, this type of single-qubit gate can also be adopted in other architectures such as the spiderweb array [21]. Having dedicated areas for single-qubit gates reduces the number and complexity of nano magnets, as well as gate fanout.



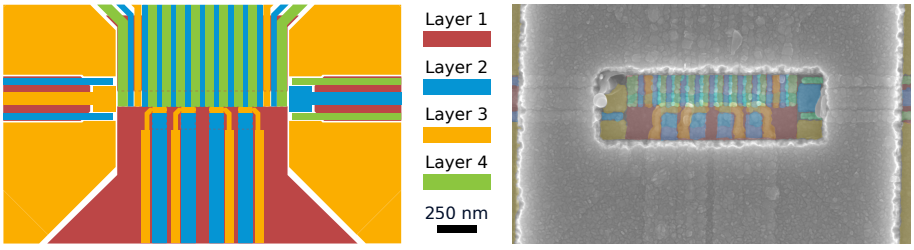


**Figure 6.1: Bilinear array.** Design schematic and SEM image of a bilinear array designed by B.W. Undseth and fabricated by L. Tryputen and D. Degli Esposti with ideas from [22]. The altering green (barriers) and blue (plungers) gates coming from the top aim to control a conveyor channel. The two yellow gates are the barriers between the two quantum dots used for PSB readout. The four blue gates from the bottom are intended to form the quantum dots hosting the spin qubits. The SEM image includes the micromagnet in grey. A potential defect can be seen on the inside top left corner.

Experiments testing the integration of hopping gates with conveyor-mode shuttling and two-qubit gates are currently in progress in our group. The design schematic alongside a false-coloured SEM image is shown in Fig. 6.1. The shuttling bus on the top part comprises 23

gates that can also be used to define 11 quantum dots. The lower half implements four static quantum dots which couple to the third, fifth, seventh and ninth quantum dot of the top row. In operation, the four static dots are considered the primary location of the qubits. The top row provides the secondary quantum dot to execute a hopping gate, a link to move a qubit to a readout zone close to the an SET (e.g. quantum dot 1 and 2 of the top row) and means to implement two-qubit gates [23]. The micromagnet on top of the four gate layers is further optimised for hopping control while maintaining a driving and addressability gradient for debugging purposes with EDSR.

While implementing hopping spins is certainly not free of challenges, it reopens old ways of thinking about operating spin qubits beyond robust micromagnet design [24].

## GENERAL OUTLOOK

While the vision of universal, fault-tolerant quantum computers remains distant, remarkable strides in hardware development have accelerated progress toward practical quantum advantage. Among the leading platforms, superconducting qubits currently dominate the landscape due to their initial scalability and controllability. Milestones such as processors with over 1000 qubits and and processors gate fidelities exceeding 99.9 % for single-qubit and two-qubit operations have been achieved [25–27]. But also other implementations such as trapped ions, neutral atoms or photonic qubits repeatedly make headlines with their successes.



This rapid advancement has been fuelled by an unprecedented influx of capital, with global investment in quantum technologies surpassing $2 billion in 2023 [28]. Governments, tech giants, and venture capitalists have poured resources into the field, driven by both strategic competition and speculative optimism. However, this growth model risks instability if practical applications fail to materialize. For long-term progress, the field must transition beyond hype and venture capital-driven cycles to establish sustainable, economically viable use cases. This transition hinges on maximizing the utility of noisy intermediate-scale quantum (NISQ) devices. While NISQ-era algorithms have shown promise, their real-world impact remains limited by noise, qubit connectivity, and the absence of provable speed-ups. Without such NISQ applications, parallels to fusion energy can be found. A possible impact so great the technology can’t be ignored, but lack of economical sustainability makes private investments scarce and institutional investments small.

Despite these challenges, the mood in the quantum community is far from pessimistic. Recent progress underscores that building a large-scale fault-tolerant quantum computer is increasingly framed as

an engineering challenge rather than a fundamental physics problem. Nonetheless, Feynman predicting it to be challenging was certainly correct.

# REFERENCES


[1] H. C. George, M. T. Mądzik, E. M. Henry, A. J. Wagner, M. M. Islam, F. Borjans, E. J. Connors, J. Corrigan, M. Curry, M. K. Harper, D. Keith, L. Lampert, F. Luthi, F. A. Mohiyaddin, S. Murcia, R. Nair, R. Nahm, A. Nethwewala, S. Neyens, B. Patra, R. D. Raharjo, C. Rogan, R. Savytskyy, T. F. Watson, J. Ziegler, O. K. Zietz, S. Pellerano, R. Pillarisetty, N. C. Bishop, S. A. Bojarski, J. Roberts, and J. S. Clarke. "12-Spin-Qubit Arrays Fabricated on a 300 mm Semiconductor Manufacturing Line". In: *Nano Letters* 25.2 (Dec. 2024), pp. 793–799. doi: 10.1021/acs.nanolett.4c05205.

[2] X. Xue, M. Russ, N. Samkharadze, B. Undseth, A. Sammak, G. Scappucci, and L. M. K. Vandersypen. "Quantum logic with spin qubits crossing the surface code threshold". In: *Nature* 601.7893 (Jan. 2022), pp. 343–347. doi: 10.1038/s41586-021-04273-w.

[3] A. Noiri, K. Takeda, T. Nakajima, T. Kobayashi, A. Sammak, G. Scappucci, and S. Tarucha. "Fast universal quantum gate above the fault-tolerance threshold in silicon". In: *Nature* 601.7893 (Jan. 2022), pp. 338–342. doi: 10.1038/s41586-021-04182-y.

[4] A. Mills, C. Guinn, M. Feldman, A. Sigillito, M. Gullans, M. Rakher, J. Kerckhoff, C. Jackson, and J. Petta. "High-Fidelity State Preparation, Quantum Control, and Readout of an Isotopically Enriched Silicon Spin Qubit". In: *Physical Review Applied* 18.6 (Dec. 2022). doi: 10.1103/physrevapplied.18.064028.

[5] S. G. J. Philips, M. T. Mądzik, S. V. Amitonov, S. L. de Snoo, M. Russ, N. Kalhor, C. Volk, W. I. L. Lawrie, D. Brousse, L. Tryputen, B. P. Wuetz, A. Sammak, M. Veldhorst, G. Scappucci, and L. M. K. Vandersypen. "Universal control of a six-qubit quantum processor in silicon". In: *Nature* 609.7929 (Sept. 2022), pp. 919–924. doi: 10.1038/s41586-022-05117-x.

[6] K. Takeda, A. Noiri, T. Nakajima, L. C. Camenzind, T. Kobayashi, A. Sammak, G. Scappucci, and S. Tarucha. "Rapid single-shot parity spin readout in a silicon double quantum dot with fidelity exceeding 99%". In: *npj Quantum Information* 10.1 (Feb. 2024). doi: 10.1038/s41534-024-00813-0.

[7] M. De Smet, Y. Matsumoto, A.-M. J. Zwerver, L. Tryputen, S. L. de Snoo, S. V. Amitonov, A. Sammak, N. Samkharadze, Ö. Gül, R. N. M. Wasserman, M. Rimbach-Russ, G. Scappucci, and L. M. K. Vandersypen. *High-fidelity single-spin shuttling in silicon*. 2024. doi: 10.48550/ARXIV.2406.07267.

[8] M. Volmer, T. Struck, A. Sala, B. Chen, M. Oberländer, T. Offermann, R. Xue, L. Visser, J.-S. Tu, S. Trellenkamp, Ł. Cywiński, H. Bluhm, and L. R. Schreiber. "Mapping of valley splitting by conveyor-mode spin-coherent electron shuttling". In: *npj Quantum Information* 10.1 (June 2024). doi: 10.1038/s41534-024-00852-7.

[9] J. Dijkema, X. Xue, P. Harvey-Collard, M. Rimbach-Russ, S. L. de Snoo, G. Zheng, A. Sammak, G. Scappucci, and L. M. K. Vandersypen. "Cavity-mediated iSWAP oscillations between distant spins". In: *Nature Physics* (Dec. 2024). doi: 10.1038/s41567-024-02694-8.

[10] S. Neyens, O. K. Zietz, T. F. Watson, F. Luthi, A. Nethwewala, H. C. George, E. Henry, M. Islam, A. J. Wagner, F. Borjans, E. J. Connors, J. Corrigan, M. J. Curry, D. Keith, R. Kotlyar, L. F. Lampert, M. T. Mądzik, K. Millard, F. A. Mohiyaddin, S. Pellerano, R. Pillarisetty, M. Ramsey, R. Savytskyy, S. Schaal, G. Zheng, J. Ziegler, N. C. Bishop, S. Bojarski, J. Roberts, and J. S. Clarke. "Probing single electrons across 300-mm spin qubit wafers". In: *Nature* 629.8010 (May 2024), pp. 80–85. doi: 10.1038/s41586-024-07275-6.

[11] K. Shyamsundar, E. Acuna, A. B. Mei, W. Ha, C. L. Jennings, D. S. Sanchez, A. Pan, M. D. Reed, and J. R. Petta. "High-connectivity SiGe quantum dot devices using the SLEDGE architecture". In: *2024 APS March Meeting, Session S46: Spin Qubit Arrays*. Abstract S46.00008. American Physical Society. Mar. 2024.

[12] E. Acuna, J. D. Broz, K. Shyamsundar, A. B. Mei, C. P. Feeney, V. Smetanka, T. Davis, K. Lee, M. D. Choi, B. Boyd, J. Suh, W. Ha, C. Jennings, A. S. Pan, D. S. Sanchez, M. D. Reed, and J. R. Petta. "Coherent control of a triangular exchange-only spin qubit". In: *Physical Review Applied* 22.4 (Oct. 2024). doi: 10.1103/physrevapplied.22.044057.

[13] A. J. Weinstein, M. D. Reed, A. M. Jones, R. W. Andrews, D. Barnes, J. Z. Blumoff, L. E. Euliss, K. Eng, B. H. Fong, S. D. Ha, D. R. Hulbert, C. A. C. Jackson, M. Jura, T. E. Keating, J. Kerckhoff, A. A. Kiselev, J. Matten, G. Sabbir, A. Smith, J. Wright, M. T. Rakher, T. D. Ladd, and M. G. Borselli. "Universal logic with encoded spin qubits in silicon". In: *Nature* 615.7954 (Feb. 2023), pp. 817–822. doi: 10.1038/s41586-023-05777-3.

[14] F. Borsoi, N. W. Hendrickx, V. John, S. Motz, F. van Riggelen, A. Sammak, S. L. de Snoo, G. Scappucci, and M. Veldhorst. “Shared control of a 16 semiconductor quantum dot crossbar array”. In: *arXiv* (2022). doi: 10.48550/ARXIV.2209.06609.

[15] K. Takeda, J. Yoneda, T. Otsuka, T. Nakajima, M. R. Delbecq, G. Allison, Y. Hoshi, N. Usami, K. M. Itoh, S. Oda, T. Kodera, and S. Tarucha. “Optimized electrical control of a Si/SiGe spin qubit in the presence of an induced frequency shift”. In: *npj Quantum Information* 4.1 (Oct. 2018). doi: 10.1038/s41534-018-0105-z.

[16] B. Undseth, O. Pietx-Casas, E. Raymenants, M. Mehmandoost, M. T. Madzik, S. G. J. Philips, S. L. de Snoo, D. J. Michalak, S. V. Amitonov, L. Tryputen, B. P. Wuetz, V. Fezzi, D. D. Esposti, A. Sammak, G. Scappucci, and L. M. Vandersypen. “Hotter is Easier: Unexpected Temperature Dependence of Spin Qubit Frequencies”. In: *Physical Review X* 13.4 (Oct. 2023). doi: 10.1103/physrevx.13.041015.

[17] Y. Xu, F. K. Unseld, A. Corna, A. M. J. Zwerver, A. Sammak, D. Brousse, N. Samkharadze, S. V. Amitonov, M. Veldhorst, G. Scappucci, R. Ishihara, and L. M. K. Vandersypen. “On-chip integration of Si/SiGe-based quantum dots and switched-capacitor circuits”. In: *Applied Physics Letters* 117.14 (Oct. 2020). doi: 10.1063/5.0012883.

[18] X. Xue, B. Patra, J. P. G. van Dijk, N. Samkharadze, S. Subramanian, A. Corna, B. Paquelet Wuetz, C. Jeon, F. Sheikh, E. Juarez-Hernandez, B. P. Esparza, H. Rampurawala, B. Carlton, S. Ravikumar, C. Nieva, S. Kim, H.-J. Lee, A. Sammak, G. Scappucci, M. Veldhorst, F. Sebastiano, M. Babaie, S. Pellerano, E. Charbon, and L. M. K. Vandersypen. “CMOS-based cryogenic control of silicon quantum circuits”. In: *Nature* 593.7858 (May 2021), pp. 205–210. doi: 10.1038/s41586-021-03469-4.

[19] S. J. Pauka, K. Das, R. Kalra, A. Moini, Y. Yang, M. Trainer, A. Bousquet, C. Cantaloube, N. Dick, G. C. Gardner, M. J. Manfra, and D. J. Reilly. “A cryogenic CMOS chip for generating control signals for multiple qubits”. In: *Nature Electronics* 4.1 (Jan. 2021), pp. 64–70. doi: 10.1038/s41928-020-00528-y.

[20] C.-A. Wang, V. John, H. Tidjani, C. X. Yu, A. S. Ivlev, C. Déprez, F. van Riggelen-Doelman, B. D. Woods, N. W. Hendrickx, W. I. L. Lawrie, L. E. A. Stehouwer, S. D. Oosterhout, A. Sammak, M. Friesen, G. Scappucci, S. L. de Snoo, M. Rimbach-Russ, F. Borsoi, and M. Veldhorst. “Operating semiconductor quantum processors with hopping spins”. In: *Science* 385.6707 (July 2024), pp. 447–452. doi: 10.1126/science.ado5915.

[21] J. M. Boter, J. P. Dehollain, J. P. van Dijk, Y. Xu, T. Hensgens, R. Versluis, H. W. Naus, J. S. Clarke, M. Veldhorst, F. Sebastiano, and L. M. Vandersypen. “Spiderweb Array: A Sparse Spin-Qubit Array”. In: *Physical Review Applied* 18.2 (Aug. 2022). doi: 10.1103/physrevapplied.18.024053.

[22] X. Xue. “Performance benchmarking of silicon quantum processors”. PhD thesis. May 2022. doi: 10.4233/UUID:20FCE6EF-6BB3-42A1-BDD3-53B2A282F0AE.

[23] Y. Matsumoto, M. De Smet, L. Tryputen, S. L. de Snoo, S. V. Amitonov, A. Sammak, M. Rimbach-Russ, G. Scappucci, and L. M. K. Vandersypen. *Two-qubit logic and teleportation with mobile spin qubits in silicon*. In preparation. 2025.

[24] D. Loss and D. P. DiVincenzo. “Quantum computation with quantum dots”. In: *Physical Review A* 57.1 (Jan. 1998), pp. 120–126. doi: 10.1103/physreva.57.120.

[25] D. Castelvecchi. “IBM releases first-ever 1, 000-qubit quantum chip”. In: *Nature* 624.7991 (Dec. 2023), pp. 238–238. doi: 10.1038/d41586-023-03854-1.

[26] D. A. Rower, L. Ding, H. Zhang, M. Hays, J. An, P. M. Harrington, I. T. Rosen, J. M. Gertler, T. M. Hazard, B. M. Niedzielski, M. E. Schwartz, S. Gustavsson, K. Serniak, J. A. Grover, and W. D. Oliver. “Suppressing Counter-Rotating Errors for Fast Single-Qubit Gates with Fluxonium”. In: *PRX Quantum* 5.4 (Dec. 2024). doi: 10.1103/prxquantum.5.040342.

[27] L. Ding, M. Hays, Y. Sung, B. Kannan, J. An, A. Di Paolo, A. H. Karamlou, T. M. Hazard, K. Azar, D. K. Kim, B. M. Niedzielski, A. Melville, M. E. Schwartz, J. L. Yoder, T. P. Orlando, S. Gustavsson, J. A. Grover, K. Serniak, and W. D. Oliver. “High-Fidelity, Frequency-Flexible Two-Qubit Fluxonium Gates with a Transmon Coupler”. In: *Physical Review X* 13.3 (Sept. 2023). doi: 10.1103/physrevx.13.031035.

[28] M. Dey. *Quantum Computing Statistics By Fundings, Investment Share, Revenue And Applications*. https://electroiq.com/stats/quantum-computing-statistics/. [Accessed 07-02-2025]. 2024.

# ACKNOWLEDGEMENTS

Around 15 years ago in highschool I expressed my desire to pursue research in quantum physics. After getting sidetracked on more than a few occasions I finally came back to the topic and decided to pursue a PhD degree in it. In those last five years many people supported me, and made this PhD not only possible but an absolutely amazing experience.

First and foremost, **Lieven**, you made my decision to stay after my master thesis easy. Your calm and collected way of leading created an environment where curiosity was encouraged and supported. I truly appreciate the freedom you gave in shaping my research, fostering independence. Yet you were always able to ask the right questions at the right time, challenging me and ensuring sufficient understanding. I admire how you balanced leading QuTech and our group while still making time for our monthly meetings. Thank you for providing such an inspiring and supportive research environment. But also beyond that, for all the trips, excursions, BBQs and parties that you made possible and hosted.

**Menno**, I had the pleasure of working with you during the early stages of the 2D project. The way you casually asked relevant, thought-provoking questions not only shows your great scientific mind but was an important source of feedback and inspiration.

**Giordano**, you and your group have enabled many of our scientific endeavours. The heterostructures you provide and tirelessly improve have been essential for my experiments and progress. I am also thankful for the sense of community you created through the wonderful parties you organized.

I also want to express my gratitude to my other committee members. Thank you, **Prof. dr. K. De Greve**, **Assoc. Prof. dr. A. Laucht**, **Prof. dr. L. DiCarlo**, and **Prof. dr. B. M. Terhal** for taking the time to read and evaluate my thesis.

---

*For a friend with an understanding heart is worth no less than a brother.*

Homer

---

With this quote I want to thank my two paranymphs. **Algirdas**, thinking about our friendship, I'm struck by how much you've shaped my life. Your enthusiasm for bouldering was infectious, and it wasn't long before

I joined you three times a week. The endless challenges and games we came up with always had me excited for our next session. Saturday mornings haven't been the same without you. Beyond bouldering, our regular watch parties and the countless hours spent explaining and occasionally playing board games brought so much joy into my life.

**Brennan**, I'm constantly in awe of your immense competence in both theory and experiment. Whether hunting for minus signs or coming up with new plans for the 2x2, you always approached challenges with creativity and determination. Beyond work, it's the adventures we've shared that I cherish most. From stepping out of our comfort zones to pick up salsa to the bouldering trips we've taken, you've made every experience unforgettable.

I want to extend this gratitude to everyone else who I had the pleasure to work with. **Marcel**, while our approaches to work were quite different when we teamed up, I truly appreciate the strengths you brought to our collaboration. Your meticulous attention to detail and structured way of thinking proved to be extremely valuable to our project. Though our collaboration had its challenges, your dedication and thoroughness left a lasting impression. I wish you all the best and continued success in your work in Innsbruck. **Mateusz**, working with you has been an absolute privilege. Your guidance and expertise at work have been invaluable, and your thoughtful feedback on my thesis made a world of difference. Beyond work, I'll always remember the fun we've had together. Thank you and Katarzyna for hosting me in Portland. Wishing you two all the best over there across the pond. **Oriol**, you unofficially joined my project when I was in a pinch for help and not only found PSB but also the first qubit on the 2x2. Between that, doing the lead climbing course with me, organizing climbing trips, and hosting pasta evenings, you've been an incredible source of support and adventure. I hope you'll find joy and fulfilment at your adventures. **Eline**, **Yuta** your ideas and insights proved invaluable and made our paper possible, and I'm deeply grateful for your contributions. Eline, I also wanted to congratulate you on becoming a mother. It must be an exciting new chapter! Wishing you both continued success in all your future endeavours. **Sergey**, **Anne-Marije** thank you for teaching me the ropes in the clean room and the lab. I wouldn't be where I am without your efforts and patience. **Alexander**, **Douwe**, thank you for choosing to do your master project with me, it was a joy to watch you grow and succeed. Teaching and guiding you has been a rewarding experience, and I've enjoyed seeing your progress throughout this journey.

I also want to thank everyone who I didn't work directly with but who shaped my experience in the spin qubits groups and at QuTech, whether through interesting discussions in the hallway, after group meetings, or in moments along the way. I wish all of you the utmost success and joy in all your endeavours, at work or outside of it. **Daniel**, our adven-

tures together have been nothing short of incredible. From our unforgettable trip to Japan to our climbing trips. Whether tackling new routes on the wall or indulging in fine dining, your company and unique humour made every moment more memorable. **Asser**, you have been an amazing office mate and friend, never too busy for a chat, a fabrication deep dive or some light hearted banter. Your hot takes, memes and wild stories always kept things interesting. Whether you joined us for bouldering, playing board games, or any other activity your company always made it more enjoyable. **Kenji**, **Cécile**, **Pablo**, thank you for the board game evenings. When Mars will be terraformed, we'll be ready! **Karina**, thank you for joining me on the wine course and for all the restaurant recommendation. I'm looking forward to trying each and every one of them. **Kian**, since the days of "Gin and Juice" you've been a constant presence in my QuTech experience, thanks for all the coffee and chats we had. **Christian**, **Corentin**, **Damian**, **Federico**, **Francesco**, **Jurgen**, **Valentin**, despite the busy conference schedules in the US and Italy, we still made time for rooftop bars, basketball games, and plenty limoncello - thank you for making it all so memorable! **Hanifa**, **Irene**, thank you for taking me on the rave, it was absolute joy. **Sander**, **Dennis**, **Daan**, your expertise in software engineering and the support you provide enabled my project.

A great many thanks also to **Liza**, **Maxim**, **Minh**, **Nicola**, **Tobias**, **Davide**, **Maximilian**, **Stefano**, **Alice**, **Jelmer**, **Patrick**, **Stephan**, **Sjaak**, **Tobias**, **Tzu-Kan**, and to all the other people (past and present) in the ever growing spin qubit environment in Delft.

I also want to express my gratitude towards both the technical and non-technical staff for all their contributions. **Amir**, **David**, **Delphine**, **Larysa**, **Rick**, **Saurabh**, and everyone else at TNO, thank you for your all the fab runs, optimisations and characterisations that improve our devices. **Jason**, **Matthew**, **Olaf**, **Tom**, your expertise and support in keeping our fridges cold is underrated. Your problem-solving skills have saved more than one experiment from disaster. **Berend**, **Erik**, **Haitham**, **Jelle**, **Nico**, **Raymond**, **Raymond**, **Roy**, **Roy**, **Siebe**, **Vinod** as well as the DEMO team foremost **Kees** and **Yannick** and the team of the Kavli Nanolab Delft, the same gratitude has to be extended to you for your expertise and support of our set-ups. During my PhD I also had the pleasure of doing a fair share of public outreach, I want to thank **Aldo**, **Erik** and **Maarten** for their work and support. **Csilla**, **Jenny**, **Marja**, **Monica**, **Rodica**, **Romina**, **Shannon**, thank you for running the show, the countless events you organised and helping me out with all my questions.

While colleagues became some of my dearest friends, I am just as thankful for my friends outside academia, whose laughter, encouragement, and companionship gave me much needed balance.

Everyone from the *Climbing Cult* and the *QuTech Adjacent*, **Çerağ**, **Elenor**, **Elise**, **Elodie**, **Eva**, **Melle**, **Satya**, **Pierre-Yves**, I will never for-

get the Saturday morning “podcasts” or our climbing trips. They not only got me in shape but also kept me sane when nothing else did. A special shout-out also **Knut** and **Yan**, it’s great to have you in my life!

**Alexander**, **Evelyn**, **Markus**, **Maximilian**, **Nadja**, während Covid die Welt auf den Kopf gestellt hat, habt ihr mit den Among-Us-Sessions für Ablenkung und viele Lacher gesorgt. Auch danach mit unseren ARAMs, GeoGuessr-runden und all den anderen Video- und Brettspielen habt ihr mir immer Freude bereitet und ein Gefühl von Zugehörigkeit vermittelt, das jede Distanz überbrückt. Meine Heimaturlaube, die Ausflüge in die Therme Erding, ins Mykonos und all die kleinen Momente dazwischen haben mir Kraft gegeben und Erinnerungen geschenkt, die weit über diese Arbeit hinaus Bestand haben. Auch wenn inzwischen die halbe Welt zwischen uns liegt, ein dickes Danke, dass sich zwischen uns so wenig ändert. **Lukas**, seit unseren gemeinsamen Tagen im Zeltlager begleitet mich unsere Freundschaft. Auch wenn unsere Kommunikation mittlerweile mehr als sporadisch ist, weiß ich, dass Freundschaft nicht von der Häufigkeit der Gespräche abhängt.

---

*The magic thing about home is that it feels good to leave,*
*and it feels even better to come back.*
*Das Magische am Zuhause ist, dass es sich gut anfühlt,*
*wegzugehen, und es fühlt sich noch besser an,*
*wiederzukommen.*

Wendy Wunder

---

Auch wenn die Heimaturlaube seltener wurden, bin ich immer froh, nach Hause zu euch zu kommen, **Mama**, **Papa**, **Schwesterherz** und **Kevin**. Ihr habt mich bedingungslos unterstützt, bei jeder Lebensentscheidung und jedem Umzug. Durch eure Unterstützung bin ich in die Position gekommen eine Promotion zu starten und nur durch eure Unterstützung habe ich die vergangenen fünf Jahre erfolgreich gemeistert. Danke dafür, für alles andere und für so viel mehr!

**Annika**, **Jakob**, es ist mir eine große Freude und Ehre, euch als Taufpate zu begleiten und euch beim Aufwachsen zuzusehen. Eure kleinen und großen Schritte zu erleben, erfüllt mich immer wieder mit Glück und Stolz.

---

*Thank you!*
*Danke.*

---

# CURRICULUM VITæ

## Florian Karl Unseld

08-Nov.-1993 Born in Ulm, Germany.

### EDUCATION

2004–2012 Schubart-Gymnasium Ulm

2012–2016 B.Eng. in Nachrichtentechnik
Technische Hochschule Ulm (2012-2015)
B.Eng in Electronic Engineering
Edinburgh Napier University (2015-2016)

2016–2020 M.Sc. in Electrical Engineering and Information Technology
Technische Universität München (2016-2020)
Technische Universiteit Delft (2017-2018, 2019-2020)

2020–2025 PhD in Applied Physics
Technische Universiteit Delft
*Thesis:* Spin Qubit Studies Using A 2x2 Quantum Dot Array In Si/SiGe
*Promotor:* Prof. dr. ir. L.M.K. Vandersypen

# LIST OF PUBLICATIONS


5. F. K. Unseld, B. Undseth, E. Raymenants, Y. Matsumoto, S. L. de Snoo, S. Karwal, O. Pietx-Casas, A. S. Ivlev, M. Meyer, A. Sammak, M. Veldhorst, G. Scappucci, and L. M. K. Vandersypen. *Baseband control of single-electron silicon spin qubits in two dimensions*. 2024. doi: 10.48550/ARXIV.2412.05171

4. B. W. Undseth, F. K. Unseld, E. Raymenants, and L. M. Vandersypen. "Spin-qubits device with nanomagnets for shuttling-based quantum gates and methods of operating the spin-qubits device". Patent. NL2039255. Dec. 2024

3. M. Meyer, C. Déprez, I. N. Meijer, F. K. Unseld, S. Karwal, A. Sammak, G. Scappucci, L. M. K. Vandersypen, and M. Veldhorst. "Single-Electron Occupation in Quantum Dot Arrays at Selectable Plunger Gate Voltage". In: *Nano Letters* 23.24 (Dec. 2023), pp. 11593–11600. doi: 10.1021/acs.nanolett.3c03349

2. F. K. Unseld, M. Meyer, M. T. Madzik, F. Borsoi, S. L. de Snoo, S. V. Amitonov, A. Sammak, G. Scappucci, M. Veldhorst, and L. M. K. Vandersypen. "A 2D quantum dot array in planar 28Si/SiGe". In: *Applied Physics Letters* 123.8 (Aug. 2023). doi: 10.1063/5.0160847

1. Y. Xu, F. K. Unseld, A. Corna, A. M. J. Zwerver, A. Sammak, D. Brousse, N. Samkharadze, S. V. Amitonov, M. Veldhorst, G. Scappucci, R. Ishihara, and L. M. K. Vandersypen. "On-chip integration of Si/SiGe-based quantum dots and switched-capacitor circuits". In: *Applied Physics Letters* 117.14 (Oct. 2020). doi: 10.1063/5.0012883

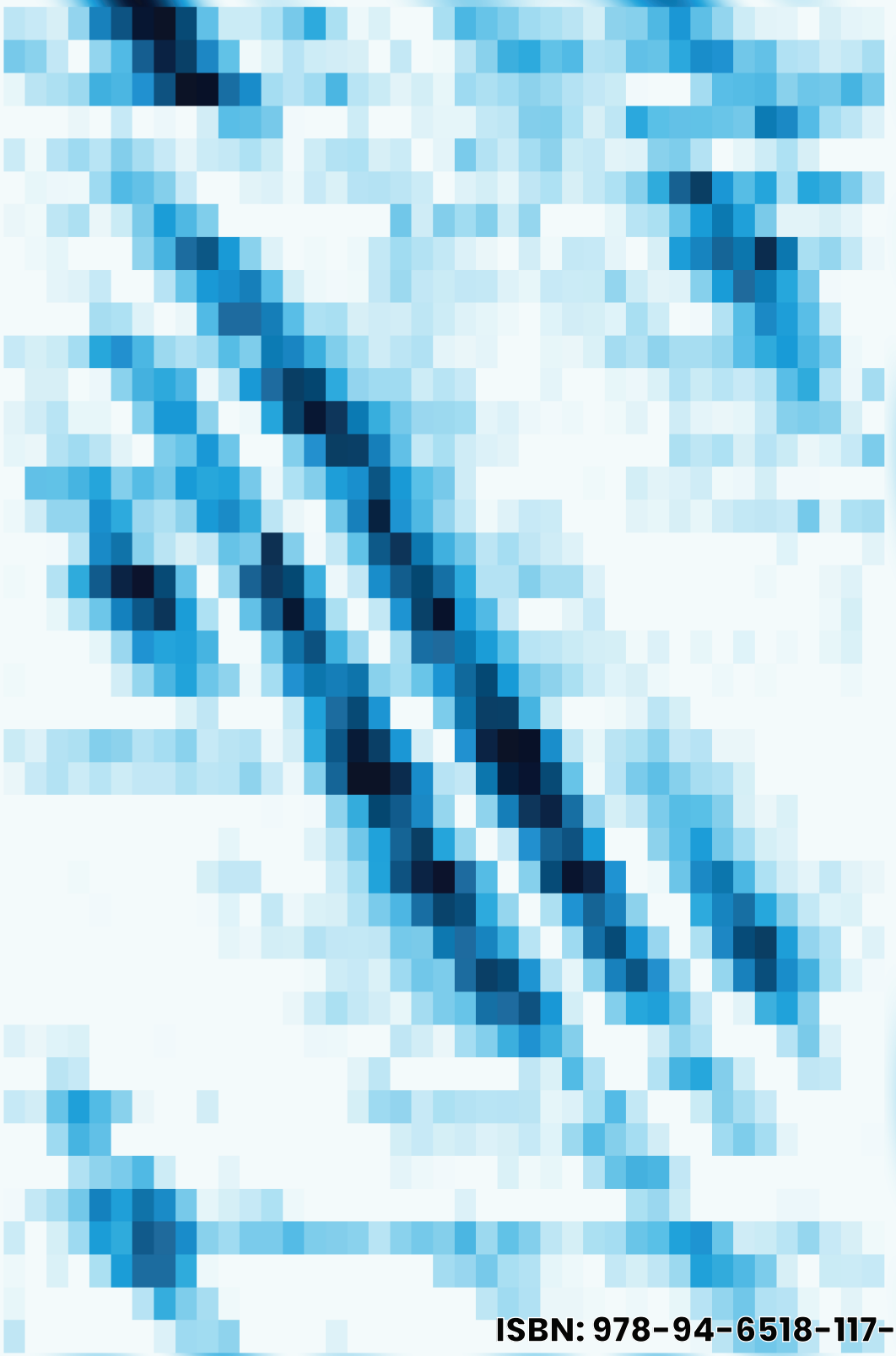

ISBN: 978-94-6518-117-2